Strategically Coupled Inertial Flow and Interfaced Evolution (SCI-FIE) Models for Dissolution Mining

by

Li Li

A thesis
presented to the University of Waterloo
in fulfillment of the
thesis requirement for the degree of
Doctor of Philosophy
in
Civil Engineering

Waterloo, Ontario, Canada, 2022

Examining Committee Membership

The following served on the Examining Committee for this thesis. The decision of the Examining Committee is by majority vote.

External Examiner: Dr. Jeffrey Priest
Professor,
Dept. of Civil Engineering,
University of Calgary

Supervisor(s):   Dr. Maurice B. Dusseault
Professor,
Dept. of Earth and Environmental Sciences,
University of Waterloo
Dr. Robert Gracie
Associate Professor,
Dept. of Civil and Environmental Engineering,
University of Waterloo

Internal-External Member: Dr. Fue-Sang Lien
Professor,
Dept. of Mechanical and Mechatronics Engineering,
University of Waterloo

Internal Member: Dr. Sriram Narasimhan
Professor,
Dept. of Civil and Environmental Engineering,
University of Waterloo

Internal Member: Dr. Shunde Yin
Associate Professor,
Dept. of Civil and Environmental Engineering,
University of Waterloo

Author's Declaration

This thesis consists of material all of which I authored or co-authored: see Statement of Contributions included in the thesis. This is a true copy of the thesis, including any required final revisions, as accepted by my examiners.

I understand that my thesis may be made electronically available to the public.

Statement of Contributions

Thesis consists in part of five manuscripts written for publication. Exception to the sole authorship of material are as follow:

Chapter 2 is based on the following peer-reviewed conference article:

L. Li, R. Gracie, M. B. Dusseault, Numerical Simulation of Salt Rock Dissolution, in: 54th U.S. Rock Mechanics/Geomechanics Symposium, U.S. Rock Mechanics/Geomechanics Symposium, American Rock Mechanics Association, Physical event cancelled, 2020.

I was the first author of this article and was responsible for writing the article. Dr. Maurice B. Dusseault and Dr. Robert Gracie reviewed and edited the paper. I developed the model and ran the simulation for the strongly coupled dissolution simulation, and did the analysis.

Chapter 3 is based on the following journal article:

L. Li, E. Rivas, R. Gracie, M. B. Dusseault, Methodology for the nonlinear coupled multiphysics simulation of mineral dissolution, International Journal for Numerical and Analytical Methods in Geomechanics 45 (15) (2021) 2193–2213.

In this article, Dr. Robert Gracie and Dr. Maurice B. Dusseault devised the project, conceptualized the main ideas, and outlined the proof. I designed the model and the computational framework in consultation with Dr. Robert Gracie and analyzed the data, and wrote the original draft. Dr. Endrina Rivas, Dr. Robert Gracie, and Dr. Maurice B. Dusseault revised, reviewed, and conceptualized the manuscript. All authors discussed the

results and contributed to the final manuscript. This chapter addresses objective one of the thesis.

Chapter 4 is based on the following journal article:

L. Li, R. Gracie, M. B. Dusseault, N. Xiao, W. Liang, Modeling and verification of nonlinear mineral dissolution processes with buoyancy effects, International Journal of Rock Mechanics and Mining Sciences (Under review).

In this article, Dr. Robert Gracie and Dr. Maurice B. Dusseault devised the main research ideas and engineering applications. I performed the numerical calculations and analyzed the data under the supervision of Dr. Robert Gracie and Dr. Maurice B. Dusseault. Dr. Robert Gracie and Dr. Maurice B. Dusseault reviewed and revised the manuscript draft written by me. Ning Xiao and I designed the lab experiments, and Ning Xiao performed experiments under the guidance of Dr. Weiguo Liang. All authors provided critical feedback and helped shape the research, analysis, and manuscript. This chapter addresses objective two of the thesis.

Chapter 5 is based on the following journal article:

L. Li, R. Gracie, M. B. Dusseault. Strategically Coupled Inertial Flow and Interface Evolution Model for Cavern Development by Dissolution, Energy (Under review)

Appendix A is based on the following conference article:

L. Li, R. Gracie, M. B. Dusseault. Salt Cavern Dissolution Mining: Lessons Learned from Simulations. In 56th US Rock Mechanics/Geomechanics Symposium. American Rock Mechanics Association, 2022.

In the articles, Dr. Robert Gracie and Dr. Maurice B. Dusseault developed the main research ideas and specified the engineering applications. I built the model, performed the numerical calculations, and analyzed the data under the guidance of Dr. Robert Gracie and Dr. Maurice B. Dusseault. I wrote the manuscript draft and the draft was reviewed and revised by Dr. Robert Gracie and Dr. Maurice B. Dusseault. This chapter addresses objective three of the thesis.

Abstract

Mineral dissolution or dissolution mining is a technology for underground mineral extraction. The space developed after the mining may be a desirable reservoir for the storage of natural gas and hydrocarbons or compressed air energy storage. The dissolution process involves a slowly moving boundary (solid-fluid interface between the mineral and brine), which must be considered in controlling the shape of the cavity in industrial practice for stable cavern construction. Mineral dissolution is a complex multi-field coupling process that includes dynamic brine flow, dissolved mineral transfer, and solid mineral dissolution. The unavailability of efficient and effective algorithms for the simulation of mineral dissolution, especially on a large scale, is currently one of the significant gaps in the literature.

Strategically Coupled Inertial Flow and Interface Evolution (SCI-FIE) models are proposed in the thesis to investigate the dissolution mechanism and provide a tool for more rigorous mineral dissolution and cavern shape control. The models are first built by developing a new loosely coupled algorithm for dissolution and boundary evolution, then improving it by adding gravity effects, and finally developing complex but physics-based model for industrial-scale dissolution simulation. These three objectives have been achieved: (1) developing a tractable numerical model simulation involving free brine flow and physically-driven boundary evolution; (2) developing a numerical model for non-linear mineral dissolution processes with buoyancy effects; and, (3) developing an integrated model for large-scale cavern evolution under turbulent flow.

The compressible Navier-Stokes equations are employed to govern the brine flow in SCI-FIE models to achieve objectives (1) and (2) to get more information about the inertial

flow. The Reynolds- Averaged Navier-Stokes equations are used to address objective (3) to analyze the turbulent brine flow in industrial-scale cavern development scenarios. The cavity boundary evolution is captured by a sharp interface model with a physically-derived dissolution rate equation. Smoothing algorithms are used to enhance the model robustness, contributing to low computational cost and stable simulation for the longer-term and larger-scale dissolution processes.

The models for objectives (1) and (2) are verified through convergence analysis, showing both spatial and temporal convergence. The second model is qualitatively validated using lab-scale experiments. The results of the cavern shape evolution simulation in the models for objective (3) show good agreement with the published experimental work.

The models can capture complex flow patterns, such as the generation of vortices (eddies) in the cavity, because the varying density of free brine flow within the cavity and the evolution of the cavity boundary are both considered. The simulation results indicate that the rising plume of less-dense brine results in the "morning glory" shape cavity under a vertical dissolution scenario and a significant difference between upper and lower fronts' dissolution for the horizontal dissolution case. The coupling effect of eddies development and the cavity shape evolution is also discussed. The results demonstrate that irregularities of the cavern wall previously assumed to be exclusively due to mineral heterogeneity, are also, at least in part, attributable to turbulent flow (eddy development). Two competing dissolution mechanisms are identified in the large-scale dissolution process, one enhancing dissolution unevenness and one that smooths out irregular dissolution features on the cavern walls. Different cavern construction methods used in industrial scale dissolution mining were investigated: reverse and direct dissolution methods, which tend towards a "morning

glory" and a "wide-bottom decanter" shaped cavern, respectively. Results suggest that, because of buoyancy effects, large roof spans seem to be unavoidable without using an oil/air blanket; however, blanket usage tends to lead to more jagged boundaries and can decrease the rate of cavern construction. The model also gives an excellent prediction of cavern evolution in the case of an insoluble interlayer present in the solution mining sequence.

This study opens a path to developing robust models of large-scale cavern development. It has implications for similar processes such as leach mining of metal ore deposits or ice melting.

Acknowledgements

All the work could not be possible without the support from many individuals.

First, I would like to express my appreciation to the committee members for reviewing my work and providing valuable suggestions and comments for improving the work.

I would express my sincere gratitude and appreciation to my supervisors, Prof. Maurice B. Dusseault and Prof. Robert Gracie, for their mentorship, patience, support and guidance throughout my Ph.D journey.

I would like to thank Prof. Haojie Lian and Prof. Weiguo Liang from the Taiyuan University of Technology for suggestions on the research and the support of the lab experiment. Furthermore, I would like to recognize the collaborative effect of Prof. Jianfeng Yang for providing me with friendship and support during the up and down of my life.

I must thank my family, my beloved parents, my sisters, and my partner who has always been there for me. Without you, none of this would have been possible.

Table of Contents

List of Tables

List of Figures

xix

Chapter 1

Introduction

1.1 Introduction to dissolution mining and cavern development

Dissolution mining or mineral dissolution is a commonly used technique in resource development and underground space utilization. Resources extracted by direct aqueous dissolution mining include salt (halite), potash (sylvite and carnallite), Glauber's salt (glauberite–a form of sodium sulfate), baking soda (nahcolite–a form of sodium bicarbonate), and several other less well-known minerals [1, 2, 3, 4]. Salt (halite) mining involves pumping water or partially saturated brine into a mineral formation to dissolve the solid soluble minerals and then pumping the mineral brine out and purifying it [5]. The caverns/cavities developed by the dissolution mining have future value for underground storage. Salt rock has low permeability and porosity, and large ductility, making a large storage capacity salt cavern an ideal reservoir for oil and natural gas storage, hydrogen storage, nuclear waste disposal, or Compressed Air Energy Storage (CAES) [6, 7, 8, 9, 10, 11, 12]. However, there are

various accidents that can happen in the creation and management of a salt cavern storage facility that may lead to integrity impairment. Most incidents are caused by human error, poor dissolution control and inadequate monitoring and management during and after the cavern construction [13]. Overhanging blocks may be developed unintentionally during the mining process because of inadequate dissolution control or thick insoluble layers. Irregular cavity shapes, as illustrated in Figure 1.1, are common results in large-scale dissolution mining or cavern development for storage facilities. A failure of the overhanging block can result in damage to tubing [14], which is used for fresh water injection and brine recovery, threatening continuous mineral extraction during the solution mining process [15]. Reliable shape control of the cavern during the dissolution mining process is needed to avoid overhanging block generation and excessively irregular shape cavern development [16].

JT86, China   Kraak-101, Germany
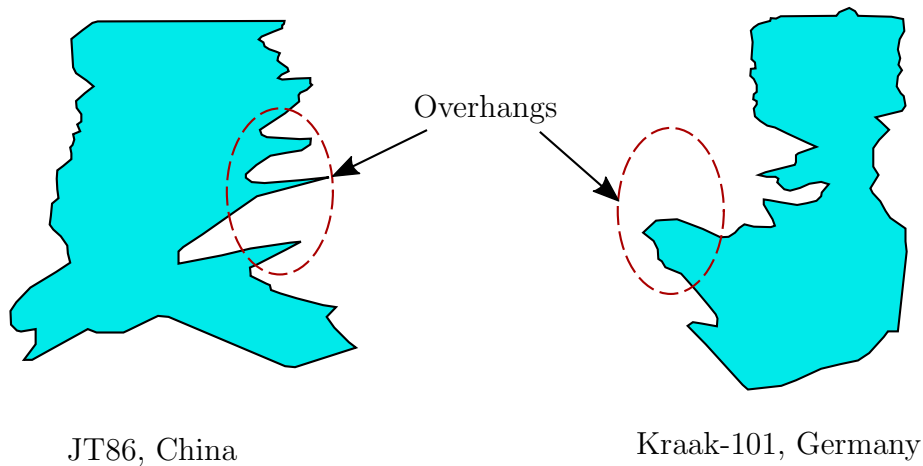
Figure 1.1: Sketch of Caverns with overhangs in China [17] and Germany [18].

Different methods are used in industry to exert control over the shape of the cavern during dissolution mining. The shape control methods include altering the location of the outlet/intake points, changing the brine flow circulation direction (direct or reverse disso-
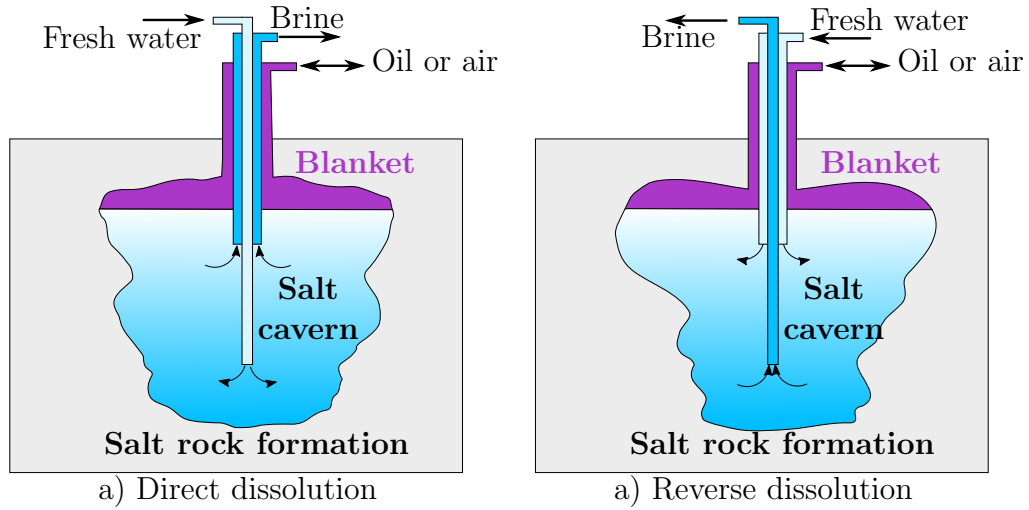
Figure 1.2: Sketch of direct (a) and reverse (b) dissolution methods with blanket (air or oil).

lution), and applying an air/oil blanket at the top of the cavity (Figure 1.2). A change of brine flow circulation direction during dissolution can alter the brine flow characteristics in the cavity and affect the dissolution pattern of the cavity boundary, but a "morning glory" type cavity with a wide top is still generally developed [19]. The "morning glory" type cavern with a large roof span is inherently unstable, and the desired shape of a stable cavern is one with a reasonably smooth domed roof [20, 21, 22]. To achieve this more optimal cavity shape, a fluid blanket is often used to control upward cavern growth due to upwards fresh water flow driven by buoyancy effects. In addition, sonar monitoring is used to provide feedback to operators. However, the cost of sonar tests is high, and the use of sonar will interrupt mining process, so continuous (or frequent) monitoring over the long-term solution mining process, typically for three to five years, is uncommon [23]. Figure 1.3 demonstrates the significant differences between the real and designed cavern shapes for a case in China [24].

The complexity of the boundary of a dissolved cavity has been widely studied and is
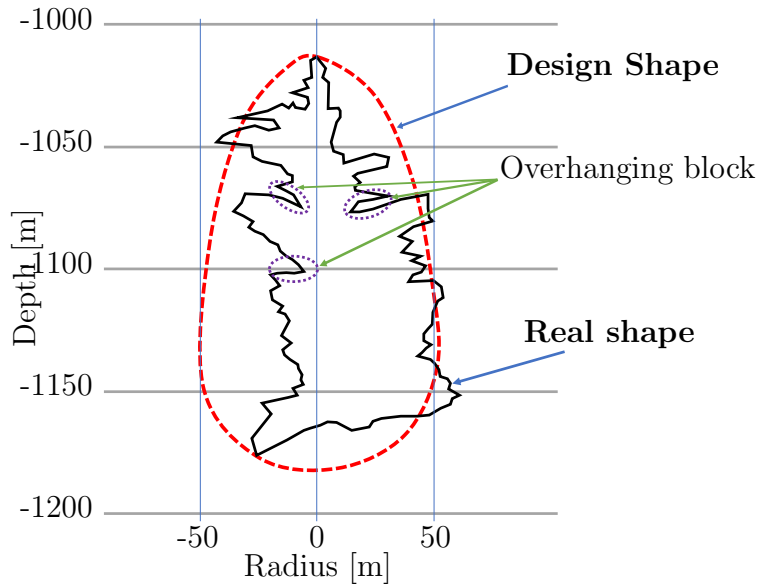
Figure 1.3: Difference between the real (black line) and designed (red dash line) salt cavern shape [24].

generally attributed to the heterogeneity of the salt formation [25, 26, 27]. A horizontal salt cavern may be proposed [28, 29] to avoid the influence of insoluble interlayers on developing stable underground caverns. Hydraulic fracturing is commonly used to connect two wellbores for the initial dissolution cavity creation, as shown in Figure 1.4. However, it is challenging to conduct dissolution rate control and cavity shape optimization during large horizontal cavern construction through air/oil blanket application [30], although it is feasible to alter the (horizontal) location of the outlet/inlet pipes and flow rate. Also, the traditional monitoring method (sonar survey) cannot be easily deployed in horizontal caverns [31], so it is difficult to monitor the cavern shape during the development process and to make real-time adjustments to control dissolution direction and shape. Recent laboratory and simulation research shows that turbulence and eddies in convective flow in the cavern also contribute significantly to the dissolution process and are more prevalent than previously understood [32, 33]. However, turbulence and eddy effects on dissolution

4

are rarely studied at the industrial cavern development scale, so further study is needed to investigate the complex dissolution process.
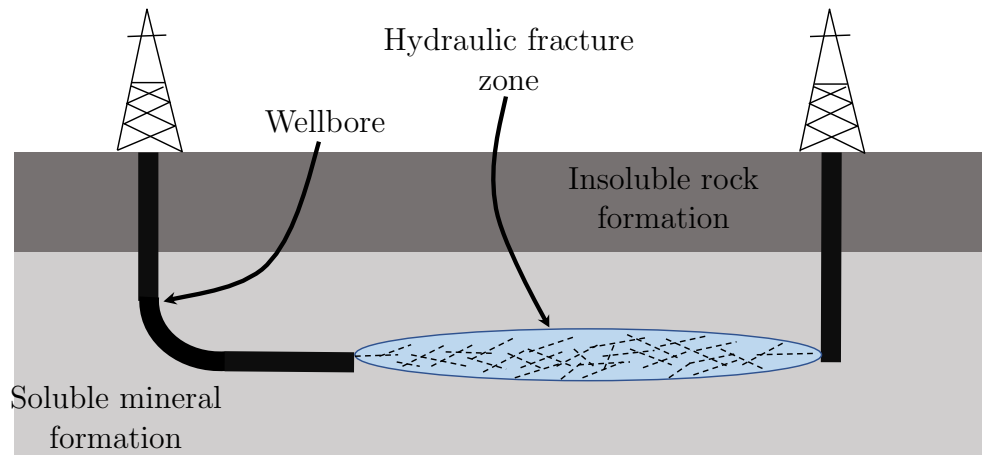
Figure 1.4: Sketch of connecting two wellbores with hydraulic fracturing for the initial dissolution cavity creation.

1.2 Mineral dissolution and cavern evolution modeling

Mathematical simulation of the dissolution process is a tool available to help understand the cavern shape evolution and evaluate factors that affect the dissolved geometry so that cavern shape predictions can be made. A dissolution simulation involves modeling brine flow and mineral mass transport within a fluid-filled cavity/cavern, dissolution/transfer of mineral mass from the cavity/cavern wall, and the evolution of the location of the cavity/cavern wall. The governing equations of the dissolution model should consider the

dissolution fronts (boundaries) evolution, mass conservation of mineral and brine, and conservation of momentum of the brine flow. The nonlinearity of the brine flow and dissolution front evolution are challenges that need to be overcome to develop an affordable dissolution simulation, especially for large-scale models. Different methods have been proposed in previous works to make the dissolution simulation more tractable.

1.2.1 Brine Flow Simulation Simplification

One of the methods to make the dissolution simulation more computationally affordable is to assume that the Reynolds number of the brine flow in the cavity is small, and hence the inertial effect can be ignored. Based on the low Reynolds number assumption, the fluid flow in the cavity is well approximated by Stokes' flow. Molins *et al.* [34] reviewed different simulation methods using Stokes' equations to study dissolution at pore scales (10^{-4} m) and showed reliable dissolution predictions, but the scales are more than two orders of magnitude smaller than industrial applications. Zidane *et al.* [35] employed Stokes' equations to describe groundwater flow to simulate large-scale salt rock dissolution underground, but the model only applies to the dissolution of salt rock near the fracture and is not feasible for large salt cavern evolution simulation. Another simplification based on the low brine flow velocity assumption is to employ a porous medium model for the fluid flow simulation. Gärttner *et al.* [36] solved the averaged velocity field by applying Darcy's law for micro-macro scale (10^{-2} m) dissolution and used level set analysis to study mineral dissolution as if the mineral were a porous medium. Nolen *et al.* [37] developed a computer program based on the finite difference method to simulate the development of salt caverns by single-well vertical leaching. In their model, Darcy's Law is used to calculate the fluid flow velocity. The permeability is an important parameter of Darcy flow

6

and needs to be specified, and the value changes during dissolution [38]. Based on the assumption of a porous medium, a fully coupled finite difference model of fluid flow, mass transfer, and dissolution was developed by Chen and Liu to study the reaction front of dissolution [39]. The Lattice-Boltzmann method (LBM) [40] and diffuse interface models (DIM) [41, 42] were used to simulate the salt rock dissolution process using fluid transport within the framework of porous media theory. The simplification of brine flow allows the model to deal with complex interfaces and can be extended to three-phase (solid, liquid, gas) dissolution simulation, and can even be upscaled to simulate the development of a cavity on the scale of meters [43, 44]. The porous medium flow transport equations used in the previous model, e.g., the Darcy-Brinkman equations, show good agreement with Naiver-Stokes equations when the Reynolds number is small [45], but in large cavity dissolution, the Reynolds number can reach a large value.

Under specific conditions, a Stokian and porous medium assumption-based model can provide dissolution evolution predictions. However, the solutions of "no-inertial-effect" models show deviation from the actual flow (Navier-Stokes equations-based flow) at large velocity, and the errors are sensitive to the geometry [46]. During the construction of the salt cavern, the free brine flow velocity can reach a high value, turbulent flow will appear, and the geometry of the cavern can be highly irregular [47]. An effective permeability and a characteristic length must be specified in the porous medium assumption-based model, and the influence of the value of these parameters on the dissolution is unclear. Oversimplification in the brine flow simulation can lead to inadequate results and will decrease the reliability and precision of the cavern evolution prediction.

7

1.2.2 Dissolution Boundary Movement Simulation Simplification

A strategy to reduce the nonlinearity of the governing equations for dissolution is to use simplified empirical equations of dissolution front motion. Durie *et al.* [48] conducted a series of lab experiments to investigate the dissolution of minerals and provided an empirical function of dissolution rate based on mineral concentration under different surface orientations. Then, the empirical function is employed to simulate dissolution front evolution. Li *et al.* [14] used Durie's function to study salt cavity leaching; they built several models to investigate large cavity leaching using different dissolution methods. In addition, salt cavern development in different types of salt rock formations [49, 50] and orientations [51] was studied. Their model considered the dissolution surface direction as an independent parameter contributing to dissolution and disregarded the relationship between the surface orientation and the brine flow. These articles paid much attention to the evolution of the dissolution front, but the mass conservation and the momentum conservation of brine flow during the leaching process were simplified so that the important role of the brine flow pattern in the cavern could not be addressed. Wan *et al.* [31] studied the dynamic dissolution process, which coupled the mass and momentum conservation of brine flow. However, the dissolution rate equation was empirically simplified using an equation similar to Durie's function. Sedaee *et al.* [52] employed a fourth-order polynomial to connect the dissolution rate with the brine density, but different coefficients used to determine the dissolution rate need to be specified by experiments before different applications.

In the models discussed above, the position and orientation of the dissolution surface are assumed to be the key factors that affect the dissolution rate calculation and must be determined before the simulation. Some of the coefficients need to be obtained by

corresponding lab experiments, and the coefficients are scale dependent. The relation between the value of the coefficients and boundary irregularity needs to be determined. The application of simplified dissolution rate equations will limit the feasibility and reliability of the dissolution model to predict the dissolution of irregular cavity walls.

1.3 Motivations

Shape control and cavern evolution prediction during the dissolution mining process are important to enhance the stability of the underground cavern for resource and energy storage. The mineral dissolution is impacted by natural and forced convection of the brine flow (laminar or turbulent), dissolved mineral concentration gradient near the dissolution front, and the characteristics of surrounding dissoluble mineral formations. This thesis aims to build a more rigorous model to simulate the mechanisms that lead to irregular shape development in dissolution mining and capture the key factors that can improve the cavern growth prediction.

Several gaps in the literature have been identified that need to be addressed in the realization of the main goal:

- The cavern evolution involves free brine flow and physically-driven boundary evolution; these are simultaneously active but have not yet been incorporated into a coupled numerical model on a large scale (industrial scale caverns).

- Oversimplification, either in brine flow simulation or in dissolution front evolution, contributes to limitations on the application and reliability of dissolution prediction model that purport to track the moving solid boundary.

- The coupling of the dissolution process with vortex flow and turbulent behavior in a large cavern has not been adequately addressed in the literature. The reliability and robustness of simplified mathematical models that are less computationally demanding for the case of high Reynolds number and Peclet number are questionable and require further study and improvement.

1.4   Research objectives and methodologies

Based on the background presented above, the overarching objectives of this thesis are presented in this section, and methodologies used to accomplish each of the objectives are also discussed.

1.4.1   Objective 1: Develop a tractable numerical simulation model involving free brine flow and physically-driven boundary evolution

A new coupled algorithm is proposed for simulating the dissolution process by taking advantage of the magnitude differences between the brine flow velocity and dissolution rate. The proposed model considers the varying density brine flow to be governed by the compressible Navier-Stokes equations, and the evolution of the cavity boundary is simulated with a physically derived dissolution rate equation. The sharp interface model in this work employs a new strategy to explicitly track the dissolution front, which results in a lower computational cost for long-term dissolution simulations.

The completed objective is described in Chapter 3 of the thesis, which is published in the following article:

L. Li, E. Rivas, R. Gracie, M. B. Dusseault, Methodology for the nonlinear coupled multiphysics simulation of mineral dissolution, International Journal for Numerical and Analytical Methods in Geomechanics 45 (15) (2021) 2193–2213.

1.4.2 Objective 2: Develop a numerical model for non-linear mineral dissolution processes with buoyancy effects

A new methodology for the simulation of salt cavity development by dissolution is presented. The buoyancy effect on the liquid flow due to brine density variations is investigated. The nonlinear model solves the dynamic brine flow governed by incompressible Navier-Stokes equations and employs a new explicit interface tracking strategy to address the dissolution front movements. An improved smoothing algorithm is proposed to enhance the robustness of the model. The improvements contribute to a low computational cost and stable simulation for the simulation of a long-term and meter-scale dissolution process. Spatial and temporal convergence studies are conducted, and qualitative validations of the model are carried out with lab-scale experiments. The impact of vortex generation and brine plume rise on the dissolution front evolution are captured and investigated.

The completed objective is described in Chapter 4 of the thesis, which is described in the following article:

L. Li, R. Gracie, M. B. Dusseault, N. Xiao, W. Liang, Modeling and verification of non-

linear mineral dissolution processes with buoyancy effects, International Journal of Rock Mechanics and Mining Sciences, 2022 (Under Review)

1.4.3 Objective 3: Develop an integrated numerical model for large-scale cavern evolution under turbulent flow

A methodology for simulating the dissolution mining of large caverns over a long period under turbulent flow is developed. The flow of brine is rigorously modeled using Computational Fluid Dynamics solutions of the Reynolds- Averaged Navier-Stokes equations coupled with the mass conservation equations governing the evolution of the cavern walls. Different cavern construction methods are investigated, including changing the brine circulation direction, altering the fresh water injection rate, and applying an oil/air blanket on the cavern top to address shape evolution. In addition, the influence of different fresh water injection velocities and the presence of an insoluble interlayer on dissolution is studied.

The completed objective is described in Chapter 5 of the thesis, which is discussed in the following article:

L. Li, R. Gracie, M. B. Dusseault, Strategically Coupled Inertial Flow and Interface Evolution Model for Cavern Development by Dissolution[J]. Energy, 2022. (Under Review)

The additional results for this objective is published in the following article, and is discussed in Appendix A:

L. Li, R. Gracie, M. B. Dusseault,, Salt Cavern Dissolution Mining: Lessons Learned from Simulations. In 56th US Rock Mechanics/Geomechanics Symposium. American Rock

Mechanics Association, 2022.

Chapter 2

Strongly coupled mineral dissolution modeling

2.1 Introduction

To investigate the dissolution process, the general fluid flow (with gravity effect) and mass transfer equations are numerically solved to provide the fluid flow pattern and concentration distribution in a small-scale cavity. During dissolution, fluid dynamics and mass transfer are modelled using the Finite Element Method (FEM). The Arbitrary Lagrangian-Eulerian (ALE) method is used to address factors affecting the dissolution process in a moving boundary situation and resolves features of the moving boundary in numerical simulation. The model simulates all the physics in the dissolution process simultaneously, and a strongly coupled algorithm is employed.

2.2 Mathematical model

The assumptions below are made to develop reasonable mathematical expressions of the dissolution process.

- Rock salt is considered homogeneous, a material with isotropic properties, there are no insoluble interlayers in the salt domain, and no other minerals are present.

- During dissolution, no insoluble residuals are created that might affect the dissolution process, and there are no common-ion effects because there is only one mineral - NaCl.

- The temperature of the fluid is constant.

- The fluid is an incompressible Newtonian fluid.

- The finite velocities of the dissolution interface resulting from the volume change of the salt rock are not accounted for explicitly because they are extremely small compared to the advective and density-driven fluid velocity.

The dissolution process of salt rock involves the fluid (brine) flow, mass transfer of salt, and movement of the dissolution interface.

Based on the mass conservation law, the continuity equation of the brine can be written as,

$$\frac{\partial \rho}{\partial t} + \frac{\partial}{\partial x_k}\left(\rho u_k\right) = 0 \tag{2.1}$$

in which Einstein notation is used and the repeated indices are summed; ρ is the density of the fluid, kg/m^3; x_k represents the Cartesian coordinate components; and u_k represents

the Cartesian velocity components in the direction of the corresponding coordinate, m/s.

The brine is taken as a Newtonian fluid; according to the Navier-Stokes equation, the conservation of momentum can be expressed as,

$$\rho\frac{\partial u_j}{\partial t} + \rho u_k \frac{u_j}{x_k} = -\frac{\partial p}{\partial x_j} + \frac{\partial}{\partial x_j}\left(-\frac{2}{3}\mu\frac{\partial u_k}{\partial x_k}\right) + \frac{\partial}{\partial x_i}\left[\mu\left(\frac{\partial u_i}{\partial x_j} + \frac{\partial u_j}{\partial x_i}\right)\right] + \rho f_j \qquad (2.2)$$

in which u_j is the fluid flow velocity in the j direction, m/s; p is the thermodynamic pressure, N/m^2; μ is dynamic viscosity, Ns/m^2; and, ρf_j denotes the body force, N.

Furthermore, the transport of the dissolved salt in the brine is calculated as,

$$\frac{\partial c}{\partial t} + \frac{\partial}{\partial x_k}\left(-D\frac{\partial}{\partial x_k}c\right) + \frac{\partial}{\partial x_k}(cu_k) = 0 \qquad (2.3)$$

in which c represents the molar concentration of NaCl, mol/m^3; D denotes the diffusion coefficient, m^2/s, and u_k is the velocity of the brine in the k direction, m/s.

Solving the movement of the dissolution front is essential for this study. Based on the mass conservation of NaCl near the dissolution front, the dissolution rate is related to the concentration gradient along the normal direction near the dissolution front [53]. The dissolution interface movement rate is calculated as,

$$\frac{ds}{dt} = -D\frac{M}{\rho_s}\frac{\partial c}{\partial n} \qquad (2.4)$$

in which s is the movement of the dissolution front, m; M represents the molar mass of salt rock, kg/mol; ρ_s denotes the density of solid NaCl, kg/m^3; and $\frac{\partial c}{\partial n}$ is the NaCl concentra-

16

tion gradient normal to the dissolution front, mol/m^4.

The dissolved mineral transport from solid salt rock to brine will increase the brine density. Assuming that the density change of the fluid only depends on the mineral concentration in the brine, the brine density can be expressed as [54],

$$\rho = \rho_w + cM \left(1 - \frac{\rho_w}{\rho_s} \right) \tag{2.5}$$

in which ρ_w is the density of water, m^3/kg.

2.3   Numerical modeling

The numerical simulation involves three main components: the Finite Element Method (FEM) model for simulating brine and dissolved salt rock transport in the cavern, the Moving Boundary model for solving the slowly moving dissolution interface, and the algorithm coupling the Moving Boundary and the FEM models. The numerical simulation is developed based on multiphysics coupling mathematical equations and solved by a commercial software called COMSOL Multiphysics^{TM}, which is based on the FEM. The multiphysics coupling of fluid flow and mass transfer will be investigated in the domain of dissolving salt caverns. The ALE approach, a commonly used front-tracking method, is used to track the location of the dissolution boundary of the salt cavern (salt/brine interface). In this method, the movement of the interface is solved explicitly, and the simulated domain grid moves with the moving boundary. The location information of points lying on the interface updates at each time step, and the mesh in the moving domain is continuously updated, as shown in Figure 2.1.

(a) t = 0   (b) t > 0
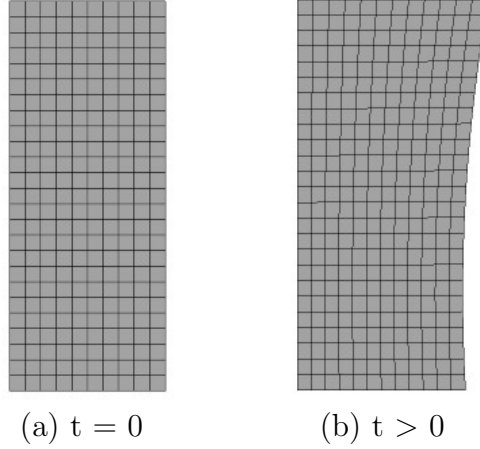
Figure 2.1:   Schematic depiction of a moving mesh solution (ALE approach).

For the simulations presented in this work, a 2D simulation model is developed. The initial geometry of the cavern is a rectangle, as shown in Figure 2.2, with the size of $H \times L$, which is set to be 5×10^{-4} m $\times$ 2×10^{-4} m. The cavity is assumed to be full of brine during the dissolution process.

The right boundary of the rectangle is set to be the dissolution front, which is assumed to be a no-slip boundary. The dissolution mineral concentration on the dissolution front is assumed to be the saturated value, which is 5400 mol/m³.

$$u|_{\Gamma_D} = 0 \ m/s \tag{2.6}$$

$$c|_{\Gamma_D} = c_S = 5400 \ mol/m^3 \tag{2.7}$$

Here, $u|_{\Gamma_D}$ is the brine flow velocity magnitude, m/s, and $c|_{\Gamma_D}$ denotes the concentration on the salt rock dissolution interface, mol/m³.
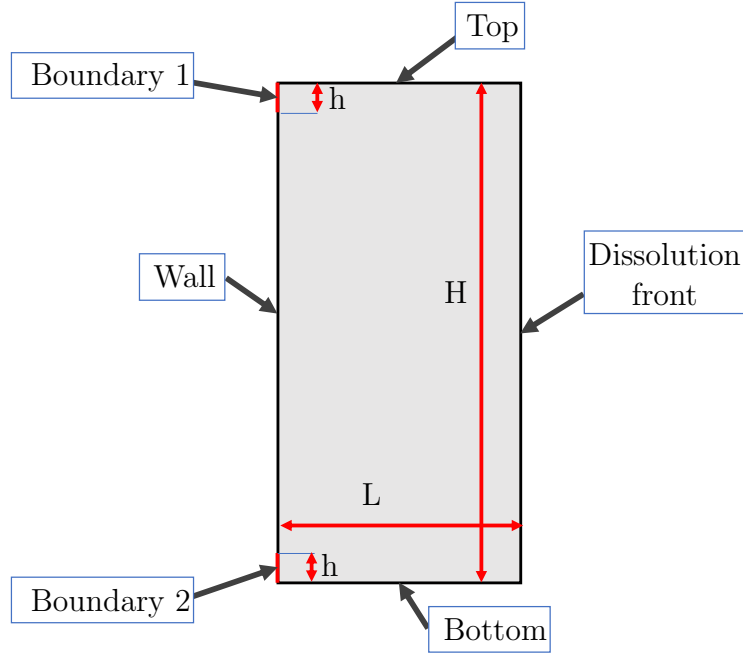
Figure 2.2: The geometry for the simulation examples.

On the left boundary, two small separate boundaries, Boundary 1 and Boundary 2, are defined, and will be used as the fresh water injecting location and brine discharging location. The length of the small boundaries is set to be h, which is 10^{-5} m. The normal velocity of the fresh water flow on the inlet surface boundary is fixed, and the concentration at the entrance is zero. On the outlet, the brine pressure is set to be equal to the atmospheric pressure.

$$u|_{in} = 0.001 \ m/s \tag{2.8}$$

$$c|_{in} = 0 \ mol/m^3 \tag{2.9}$$

$$p|_{out} = 0.1 \ MPa \tag{2.10}$$

in which $u|_{in}$ is the normal velocity of fresh water flow into the salt caverns, m/s; $p|_{out}$ is the pressure on the outlet, Pa; and $c|_{in}$ is the concentration at the inlet position, mol/m^3.

The conditions of the top, bottom, and the rest of the left wall are assumed to be no-slip boundaries without dissoluble minerals,

$$u_w = 0 \ m/s, \ and \tag{2.11}$$

$$\frac{\partial c}{\partial n}|_w = 0 \ mol/m^4 \tag{2.12}$$

in which u_w represents the magnitude of the fluid flow on the top, bottom, and wall, m/s; and $\frac{\partial c}{\partial n}|_w$ is the gradient of the NaCl concentration in the direction normal to the wall, mol/m^4.

To numerically solve the partial differential equations 2.1 to 2.5, initial and boundary conditions are needed. The initial conditions for the fluid are that the velocity is zero, the pressure equals 0.1 MPa, and the brine in the cavern is saturated. Thus,

$$u|_{t=0} = 0 \ m/s \tag{2.13}$$

$$p|_{t=0} = 0.1 \ MPa, and \tag{2.14}$$

$$c|_{t=0} = c_S = 5400 \ mol/m^3 \tag{2.15}$$

in which u is the magnitude of the fluid flow velocity, m/s, and c_S denotes the saturated molar concentration of the brine, mol/m^3.

The parameters used in this modeling are specified in Table 2.1.

Table 2.1: The parameters used for simulation.

Parameter	Variable	Value	Unit
Dynamic viscosity	μ	8.94×10^{-4}	Pa/s
Density of salt rock	ρ_{s}	2059	kg/m^3
Density of water	ρ_{w}	1000	kg/m^3
Diffusion coefficient	D	10^{-9}	m^2/s
Molar mass of salt	M	0.0585	kg/mol

2.4 Results and discussion

In this section, the comparison between laboratory experimental dissolution results and the simulation results is conducted to give a qualitative validation. In addition, the brine flow evolution and the cavity boundary location changes during dissolution are discussed.

2.4.1 Model qualitative validation

A comparison between experimental results and numerical simulation is conducted to validate the dissolution simulation model quantitatively. A dimensionally smaller simulation scale was conducted compared to the lab scale because of limitations of the numerical simulation models resulting from Peclet Number issues. The topological shape of the dissolution front for both laboratory experiments [55] and numerical simulation results are shown in Figure 2.3. The red arrows reflect the fresh water injection location, and the red dashed lines indicate the location of the initial dissolution front. H_0 represents the largest height, and L_0 denotes the largest dissolution front location for each scenario. The normalized dissolved cavity boundary outlines are plotted. For both lab work and simulation, the change of the dissolution front location is shape-similar. The large dissolution front location happens on the top regardless of the position of the injection location because

21

low-density fresh water is buoyant. When changing the fresh water injection location from the bottom to the top, the increase of the dissolution distance at the top becomes larger, and the numerical simulation models predict the phenomenon well. The trend and shape of the dissolution interface shape of the simulation results are consistent with published experimental results. This indicates that the numerical models developed in this study can provide a reference for actual dissolution processes.
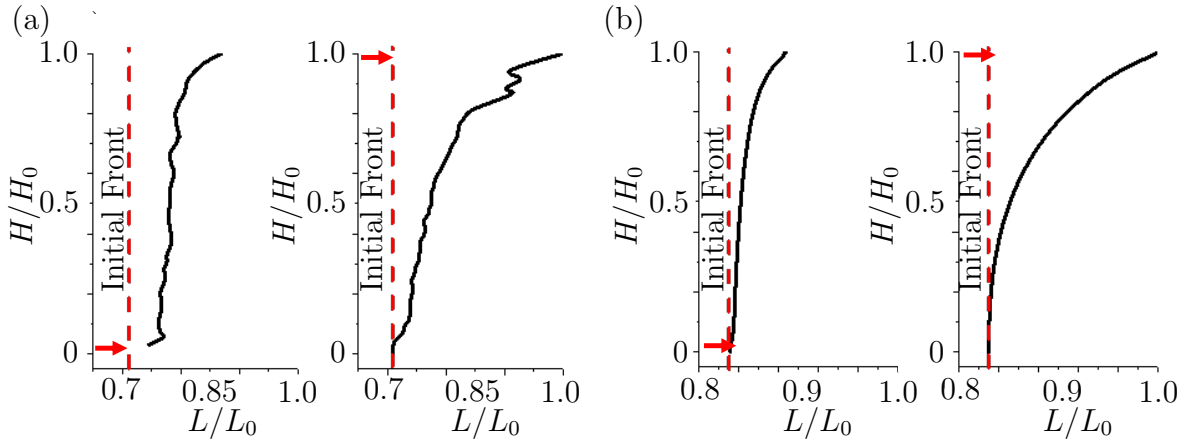
Figure 2.3: Comparison of dimensionless dissolution front location. (a) Dissolution front location of the referred lab results[55], (b) Numerical simulation results.

2.4.2 Dissolution Process

The brine flow and dissolved cavity evolution are investigated in this section. Boundary 2 is selected as the fresh water injection boundary, and the injection velocity is 0.001 m/s. Boundary 1 is set to be the brine outlet. The Reynolds number is 0.55, and the brine flow is thus laminar. The Peclet number is 20, which means that the advection plays an important role in dissolved mineral transport. The maximum mesh size is set to be 7×10^{-7} m, so the cell Peclet number is 0.08, and this ensures the stability of the simulation model.

During the dissolution process, the velocity distribution and direction in the brine domain
are shown in Figure 2.4. The distribution of brine velocity shows significant change during
the dissolution process. At the beginning of the dissolution process, a vortex is generated
in the bottom region because of the injection of fresh water. The brine flow velocity in the
upper region of the cavity is low, and no vortex appears. With the increase of time, the
geometry and velocity distribution change because of the dissolution of the salt rock. After
50 s dissolution, the original vortex grows and occupies the majority of the cavity. The
center of the vortex moves upward and increases the brine flow velocity in the upper zone of
the cavity. The velocity of the fluid near the dissolution front also increases because of the
convection effect caused by the vortex. During the dissolution between 50 s and 100 s, the
location of the vortex center does not undergo significant change, although the cavity keeps
expanding. This indicates that the brine flow reaches a quasi-steady state. In addition,
a relatively higher velocity region forms near the right boundaries in the later dissolution
process, which indicates that more fluid goes directly from the inlet to the outlet and is
not fully involved in the dissolution process.
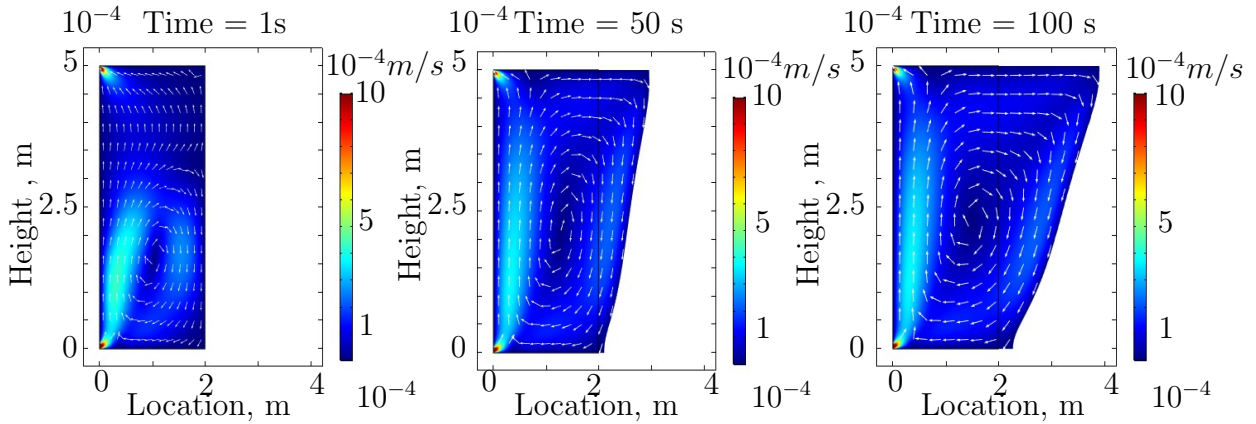
Figure 2.4:   Velocity distribution and direction during the dissolution process.

The change in the concentration distribution during the dissolution process is shown in
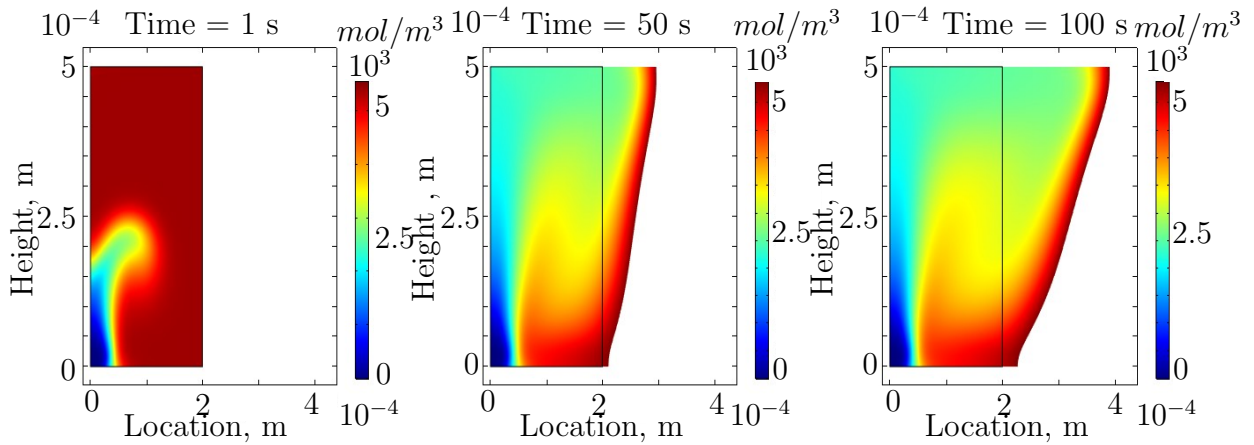
Figure 2.5: Concentration distribution during dissolution process.

Figure 2.5. The concentration distribution of the brine experiences a significant change in the early stages of the simulation (1-50 s). The injected fresh water results in a decrease in the concentration near the inlet, but the buoyancy effect is significant and leads to upward transport of the less dense brine. When the lighter brine gets mixed with the saturated brine in the cavity, the denser brine is transported downwards because of gravity. This explains why the vortex generates, as shown in Figure 2.4. The brine concentration distribution has obvious changes after 50 s dissolution: although the concentration of the brine near the inlet is still the lowest in the cavity, the brine with a lower concentration (around 2.5×10^3 mol/m^3) occupies the top of the cavity. The lower concentration brine is lighter than the saturated brine, and the buoyancy effect forces the less dense brine to be trapped near the top. The less concentrated brine on the top flows horizontally, gets in touch with the solid salt rock interface, dissolves the solid mineral, densifies, and flows downwards. The brine concentration keeps increasing when it flows past the dissolution front, and the concentration approaches the saturated value when the brine reaches the bottom of the cavern, explaining why there is far less significant dissolution at the bottom.

Another phenomenon shown in the dissolution process is that the overall distribution of the dissolved mineral concentration does not undergo significant change. It indicates that dissolved mineral transportation also reaches a quasi-steady state, although the dissolution boundary is continuing to move outward slowly.
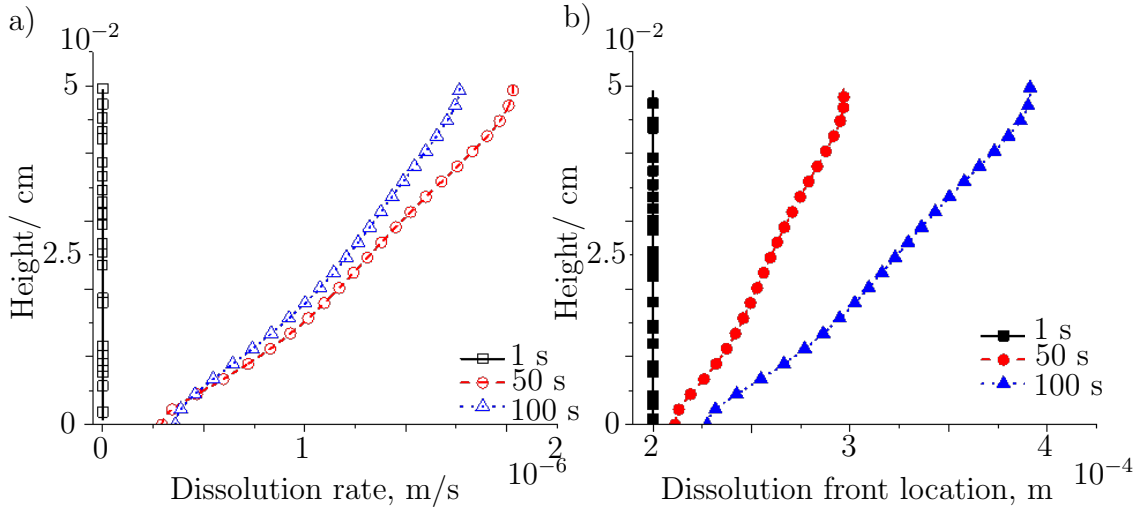
Figure 2.6: Dissolution rate (a) and distance (b) during the dissolution process.

The dissolution rate along the cavity boundary and the evolution of the dissolution front are shown in Figure 2.6. As described by Equation 2.4, the dissolution rate is related to the concentration gradient near the wall. The injected fresh water seriously disturbs the dissolved mineral distribution in the cavity in the early stage, but the advection does not affect the mineral transport near the dissolution front, which is also illustrated in Figure 2.5. So, there is no significant dissolution at the early stage. After 50 s of continuous injection of fresh water, the distribution of convection on the dissolved mineral expands to the whole cavity, and the concentration difference near the dissolution front becomes obvious. The dissolution rate increases with the cavity height because the buoyancy effect

promotes the rise of lower concentration brine to the top. The dissolution rate does not undergo a noticeable change during the later period of dissolution. The top dissolution rate only increases by about 12%, and the value slightly changes at the bottom boundary. In addition, there is a magnitude difference between the dissolution rate and the inlet fresh water injecting velocity, which is 10^{-4} to 10^{-3}.

2.5 Conclusions and limitations

The main conclusions and limitations of the study are:

- During the dissolution process, the flow pattern, concentration distribution, and dissolution rate at the solid-brine interface vary significantly in the early stages. The dissolution rate on the salt-brine interface experiences obvious changes. In later stages, the flow pattern and concentration distribution only undergo minimal change, and the change in dissolution rate is negligible. There is a large magnitude difference between the fresh water injection velocity and dissolution rate, even in a small dissolution cavity. The quasi-steady-state of the brine transport and cavity boundary evolution can last for a relatively long time.

- Gravity (buoyancy) significantly impacts the dissolution process and must be considered explicitly in mathematical formulations leading to engineering tools.

- The fully coupled dissolution model can predict the cavity evolution, and the results can be qualitatively validated by ignoring the spatial scale differences. The simulation can only be stable when the Pectlet number is low, requiring the cell mesh and time step to be small. The restriction on the mesh and timestep size limits the application of a fully coupled dissolution model to large cavern evolution simulation.

Chapter 3

Methodology for the nonlinear coupled multi-physics simulation of mineral dissolution

3.1   Introduction

The strong coupled model, which is discussed in Chapter 2, is expensive for large-scale and long-term dissolution simulation, so a more tractable numerical simulation model is desired. A new numerical methodology for simulating the coupled dissolution process is presented in this chapter. As a first step, we will focus on the simulation of the dissolution of narrow channels (fractures) in a two-dimensional context. This involves the coupling of brine flow, transfer of mineral mass in the cavity, and geometry evolution. The nonlinear equations governing brine flow, described in Section 3.2, are solved with varying brine density to more accurately capture the flow patterns. A nonlinear dissolution rate is derived from

local mass conservation at the dissolution front. New algorithms are presented in Section 3.3 for dissolution front evolution and the coupling strategy between brine flow and the moving interface. The gravitational force is assumed to be negligible in the model, making it applicable for small-scale dissolution simulation. The proposed model is used to simulate mineral dissolution along a horizontal cavity in Section 3.4. The model is verified using a convergence analysis, the brine flow and dissolution patterns are discussed, and the effect of Peclet number on the results is investigated. This work advances our understanding of the interaction between fluid transport and dissolution patterns that affect the early stages of solution mining.

3.2   Governing equations

The governing equations for the dissolution process are described in this section. The proposed model assumes that the flow of the aqueous solution and mass transfer of the mineral happens inside the dissolved cavity and some of the boundaries (the dissolution fronts) of the domain move during the dissolution process. The mineral dissolution model solves (1) the equations that govern the mass conservation and the motion of an aqueous solution, (2) the advection-diffusion equation for the transport of the dissolved component in the aqueous solution, and (3) the dissolution front evolution equation governed by the conservation of mass.

3.2.1   Fluid flow and mass transfer

The governing equations of free brine flow and dissolved mineral transport are discussed in this section. These are derived without assuming that the fluid is incompressible. The

general form of the equations captures the change in brine density with a change in mineral concentration, which affects the brine flow pattern. The variable brine density also introduces nonlinear terms to the governing equations.

Mass conservation of the brine in the cavity is described by the continuity equation,

$$\frac{\partial \rho}{\partial t} + \nabla \cdot (\rho \mathbf{U}) = 0 \tag{3.1}$$

in which $\rho(\mathbf{x}, t)$ is the density of the brine [kg/m³], $\mathbf{U}(\mathbf{x}, t)$ is the brine flow velocity [m/s], $\mathbf{x}$ is the spatial coordinate system within the cavity [m], and t is the time [s].

The brine is assumed to be a Newtonian fluid. The principle of conservation of momentum of the brine with changing density leads to the Navier–Stokes equation,

$$\frac{\partial}{\partial t}(\rho \mathbf{U}) + \rho (\mathbf{U} \cdot \nabla) \mathbf{U} = -\nabla p + \nabla \cdot \left[\mu \left(\nabla \mathbf{U} + (\nabla \mathbf{U})^{\mathrm{T}} - \frac{2}{3} (\nabla \cdot \mathbf{U}) \mathbf{I} \right) \right] + \nabla \cdot [K (\nabla \cdot \mathbf{U}) \mathbf{I}] + \rho \mathbf{g} \tag{3.2}$$

in which $p(\mathbf{x}, t)$ is the fluid pressure [Pa], μ is the dynamic viscosity [Pa · s], K is the bulk viscosity [Pa · s], $\mathbf{g}$ denotes the body force [m/s²], and $\mathbf{I}$ is the identity tensor.

The transport of the dissolved mineral is a combination of advection and diffusion [56]. Mass conservation of dissolved mineral in the brine is governed by,

$$\frac{\partial}{\partial t}(\rho \Phi) + \nabla \cdot (\mathbf{U} \rho \Phi) = -\nabla \cdot (-\rho D_{\mathrm{s}} \nabla \Phi) \tag{3.3}$$

in which $\Phi(\mathbf{x}, t)$ is the mass fraction of the soluble mineral and D_s is the mass diffusion coefficient of the mineral in brine [m^2/s].

The density of brine is a function of the concentration of the dissolved mineral. Yang et al. [54] provided a formula relating brine density to the molar concentration of the dissolved mineral. By modifying their formula based on the mineral mass fraction, the brine density can be expressed as,

$$\rho = \rho_w + \frac{\rho_w \left(1 - \frac{\rho_w}{\rho_s}\right)}{\frac{1}{\Phi} + \frac{\rho_w}{\rho_s} - 1} \tag{3.4}$$

in which ρ_w represents the density of water [kg/m^3] and ρ_s denotes the density of pure solid mineral rock [kg/m^3]. This equation defines the brine density in terms of the water density, the basic mineral property (the solid mineral density), and the mass fraction of the dissolved mineral, which makes the equation more readily applied to the dissolution of different minerals. While other works have used (3.4) as an auxiliary equation for the momentum conservation equation [54, 57], the brine density equation is a part of the coupled system of all fluid flow and mass transfer equations in this work.

3.2.2 Mass conservation at the dissolution front

The mineral dissolution process occurs at the mineral and water interface, a solid-liquid interface. The difference in mineral concentration between the brine and the solid mineral rock is the driving force for the dissolution. Two competing processes occur at the solid-liquid interface: dissolution and crystallization. When the mineral concentration in the aqueous phase is low, dissolution dominates, and the bulk mineral dissolves. With

prolonged dissolution, the amount of the dissolved mineral in the solution increases and the concentration rises; the crystallization rate increases while the dissolution rate drops. Over time, the solution becomes saturated and the large-scale crystallization and dissolution rates equalize. While the temperature has effects on the dissolution [58], it is not considered in the current model. In this model, freshwater is continuously injected into the cavity, causing the mass fraction of the mineral in the solution to remain smaller than the saturated value, so only the dissolution process is considered.

Dissolution is assumed to occur along a zero-thickness solid-liquid interface called the dissolution front. Minerals are dissolved at the dissolution front and transferred to the brine. The dissolution process is illustrated in Figure 3.1. Consider the cubic cell at the interface shown in Figure 3.1; the mass of mineral transported out of the cell is equal to the mass dissolved from the solid mineral surface. The mass balance is described by

$$\Delta s_\mathrm{d} \Delta t \mathbf{N} \cdot \mathbf{n} = \frac{\rho_\mathrm{s}}{M} \Delta L \Delta s_\mathrm{d} \tag{3.5}$$

in which $\mathbf{N}$ is the flux of dissolved mineral [mol/m^{2}s], $\mathbf{n}$ is the normal vector of the dissolution front, Δs_d is the surface area of the dissolution front [m^2], Δt is the dissolution time [s], M is the molar mass of salt rock [kg/mol], and ΔL is the dissolution distance during the dissolution process [m].

The total flux of mineral from the dissolution front includes the Fickian diffusion and the advective transport of the dissolved mineral [59]. Based on the principle of superposition, the total flux is,

$$\mathbf{N} = -D_\mathrm{f} \nabla c + c\mathbf{U} \tag{3.6}$$
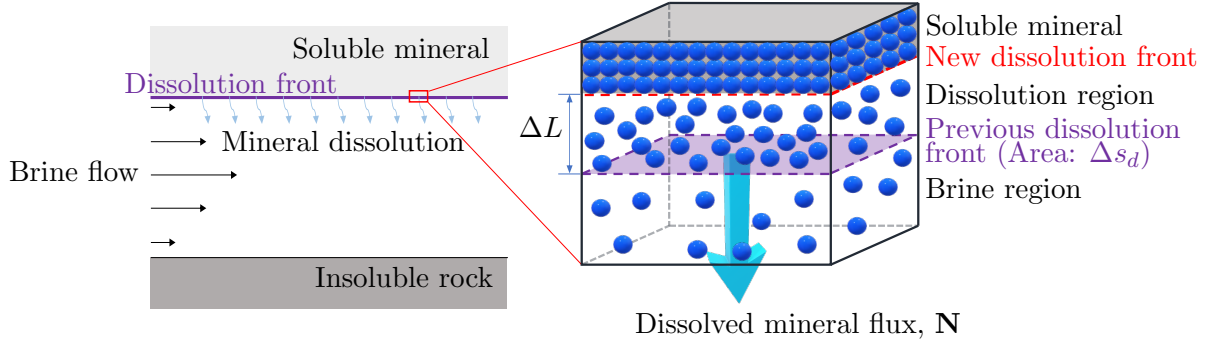
Figure 3.1: Schematic of macro-scale (left) and micro-scale (right) dynamic dissolution process. The dissolved mineral is transferred from the dissolution front with flux $\mathbf{N}$. After Δt, a new dissolution front is located at a distance of ΔL from the previous front. The flow of brine in the cavity transports away the dissolved minerals.

in which c is the molar concentration of dissolved mineral [mol/m^3] and D_f is the diffusion coefficient near the dissolution front [m^2/s].

Combining (3.5) and (3.6), and taking the limit as ΔL and Δt go to zero, the dissolution rate, v_d [m/s], is given by

$$v_\mathrm{d} = \frac{dL}{dt} = \frac{M}{\rho_s} \left(-D_\mathrm{f} \nabla c + c\mathbf{U} \right) \cdot \mathbf{n} \tag{3.7}$$

The relation between molar concentration and mass fraction of dissolved mineral in the brine is,

$$c = \frac{\rho_\mathrm{w}}{M \left(\frac{1}{\Phi} + \frac{\rho_\mathrm{w}}{\rho_\mathrm{s}} - 1 \right)} \tag{3.8}$$

Substituting (3.8) into (3.7) gives an expression for the dissolution rate in terms of the mass fraction of the soluble mineral,

$$v_\mathrm{d} = \frac{\rho_\mathrm{w}}{\rho_\mathrm{s} \left(\frac{1}{\Phi} + \frac{\rho_\mathrm{w}}{\rho_\mathrm{s}} - 1 \right)^2 \Phi^2} \left(-D_\mathrm{f} \nabla \Phi + \left(\frac{1}{\Phi} + \frac{\rho_w}{\rho_s} - 1 \right) \Phi^2 \mathbf{U} \right) \cdot \mathbf{n}. \tag{3.9}$$

3.2.3 Model simplification

Previous laboratory and field studies [60, 61, 62] have shown that the dissolution rate is low compared to brine flow rates, and the flow of the brine will reach and the dissolved mineral concentration will achieve a quasi-steady state in a short amount of time (e.g., it takes less than 2 s to reach the quasi-steady state for mineral dissolution in a 0.1 m length channel with 0.1 m/s inlet freshwater velocity) [63]. The distribution of dissolved minerals near the dissolution front will not undergo significant change after the quasi-steady state is established, and the dissolution rate on the front does not change significantly, as shown in Chapter 2. Hence, the assumption is made that the brine flow in the dissolved cavity is steady-state during the dissolution process, and the dissolution rate is steady over a relatively long period. This is a major departure from many previous models, which solve the transient problem and incur higher computational costs (e.g., COMSOL [64], DIM [43] , and LBM [40]). The mechanical pressure and the thermodynamic pressure of the brine is considered to be the same, so the bulk viscosity is zero. The lab experiments show that gravity has effects on the brine flow [65]. However, the Froude number (F_r) increases with the characteristic length of the model, indicating that the influence of the gravity term (in Navier-Stokes equations) can be less critical for the brine flow in a smaller cavity. So, as a first step, the gravity force is ignored in the proposed model. Nonetheless, we will endeavor to eliminate this assumption in future iterations of the model for large-scale problems.

Based on the above assumptions, (3.1), (3.2), and (3.3) are simplified to the following set of nonlinear equations,

$$\nabla \cdot (\rho \mathbf{U}) = 0 \tag{3.10}$$

$$\rho \left(\mathbf{U} \cdot \nabla \right) \mathbf{U} = -\nabla p + \nabla \cdot \left[\mu \left(\nabla \mathbf{U} + (\nabla \mathbf{U})^{\mathrm{T}} - \frac{2}{3} \left(\nabla \cdot \mathbf{U} \right) \mathbf{I} \right) \right] \tag{3.11}$$

$$\nabla \cdot (\rho \mathbf{U} \Phi) = -\nabla \cdot (-\rho D_{\mathrm{s}} \nabla \Phi) \tag{3.12}$$

The simplified equations still capture the change in brine density with a change in the mass fraction of the dissolved mineral in the nonlinear terms.

The dissolution front is a no-slip boundary. Since the evolution of the dissolution is slow, the relative brine flow velocity on the dissolution front is considered to be zero. Thus, the advection term ($\mathbf{U}$) on the right-hand side of (3.9) can be eliminated and the dissolution rate (3.9) is further simplified as,

$$v_{\mathrm{d}} = \frac{\rho_{\mathrm{w}}}{\rho_{\mathrm{s}} \left(\frac{1}{\Phi} + \frac{\rho_{\mathrm{w}}}{\rho_{\mathrm{s}}} - 1 \right)^2 \Phi^2} \left(-D_{\mathrm{f}} \nabla \Phi \right) \cdot \mathbf{n} \tag{3.13}$$

The dissolution distance ΔH of a point on the dissolution front over the time step τ is

approximated as,

$$\Delta H = \int_{T_0}^{T_0+\tau} v_{\mathrm{d}} dt \approx v_{\mathrm{d}}\tau$$

$$= \frac{\rho_{\mathrm{w}}}{\rho_{\mathrm{s}} \left(\frac{1}{\Phi} + \frac{\rho_{\mathrm{w}}}{\rho_{\mathrm{s}}} - 1\right)^2 \Phi^2} \left(-D_{\mathrm{f}}\nabla\Phi\right) \cdot \mathbf{n}\tau \tag{3.14}$$

in which the second equality assumes that the process is quasi-steady, so v_{d} can be assumed to be constant over τ.

3.2.4 Global mass conservation during dissolution

The complete dissolution process involves freshwater injection, mineral dissolution, and brine discharge. Consider brine flow through a cavity embedded in a soluble mineral, as illustrated in Figure 3.2. Conservation of mass of the mineral over the whole domain and over the time period τ requires that the amount of mineral dissolved from the brine-mineral interface, m_{D}, be equal to the difference of the mass exiting and entering the cavity, m_{E}, plus any additional mineral mass stored in the solution, m_{S}. The global mass balance is given as

$$\int_{T_0}^{T_0+\tau} \left(\int_{\Gamma_{\mathrm{out}}} \Phi_{\mathrm{out}}\rho_{\mathrm{out}}\mathbf{U}_{\mathrm{out}} \cdot \mathbf{n}d\Gamma - \int_{\Gamma_{\mathrm{in}}} \Phi_{\mathrm{in}}\rho_{\mathrm{in}}\mathbf{U}_{\mathrm{in}} \cdot \mathbf{n}d\Gamma\right) dt + \left(\int_{\Omega'} \rho'\Phi'd\Omega' - \int_{\Omega} \rho\Phi d\Omega\right)$$

$$= \int_{T_0}^{T_0+\tau} \int_{\Gamma_{\mathrm{d}}} v_{\mathrm{d}}\rho_{\mathrm{s}}d\Gamma dt \tag{3.15}$$

in which T_0 is the initial time [s]; τ is the dissolution period length [s]; Γ_{in}, Γ_{out}, and Γ_{d} are

35

the inlet, outlet, and the dissolution front surfaces [m^2], respectively; Φ_{in} and Φ_{out} are the mass fraction of dissolved mineral at the inlet and outlet boundaries; ρ_{in} and ρ_{out} are the inlet and outlet brine densities [m^3/s]; $\mathbf{U}_{\text{in}}$ and $\mathbf{U}_{\text{out}}$ are the inlet and oulet brine velocities [m/s]; Ω and Ω' are the cavity domains at the start of dissolution $(t = T_0)$ and end of dissolution $(t = T_0 + \tau)$, respectively; ρ and ρ' are the brine densities at the start and end of the dissolution time step [kg/m^3]; and Φ and Φ' are the corresponding mass fraction of dissolved mineral at the start and end of the dissolution time step.
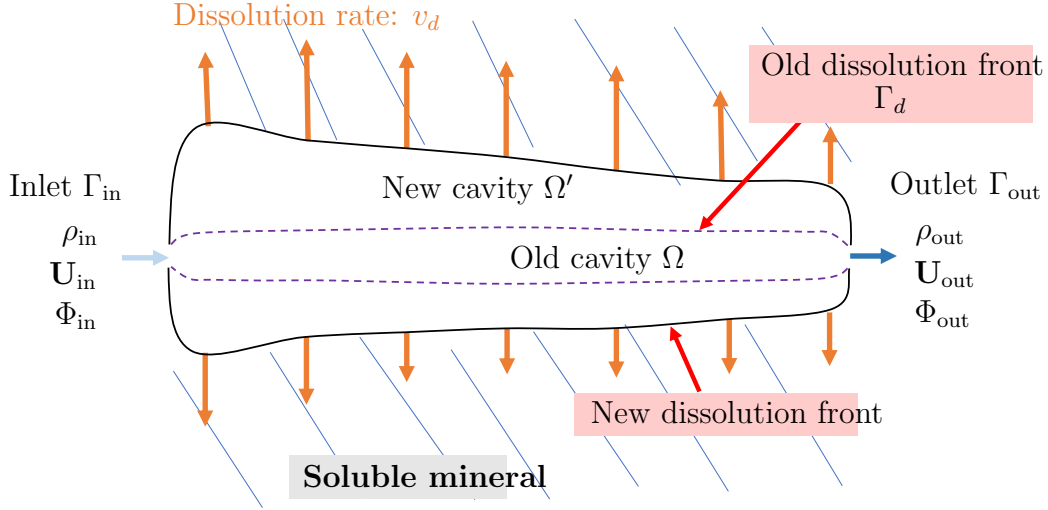
Figure 3.2: Mass conservation during the enlargement of a dissolved cavity embedded in a soluble mineral.

From the global mass conservation (3.15), three quantities of interest are derived: the mass of mineral dissolved along the mineral-brine interface (m_D), the dissolved mineral mass extracted from the cavity (m_E), and the dissolved mineral mass stored in the solution (m_S).

The mass of mineral dissolved from the mineral-brine interface, m_{D}, over the dissolution

time τ is approximated as,

$$
\begin{aligned}
m_{\mathrm{D}} &= \int_{\Gamma_{\mathrm{d}}} \Delta H \rho_{\mathrm{s}} d\Gamma \\
&= \left[\int_{\Gamma_{\mathrm{d}}} \frac{\rho_{\mathrm{w}}}{\left(\frac{1}{\Phi} + \frac{\rho_{\mathrm{w}}}{\rho_{\mathrm{s}}} - 1 \right)^2 \Phi^2} (-D_{\mathrm{f}} \nabla \Phi) \cdot \mathbf{n} d\Gamma \right] \tau
\end{aligned}
\tag{3.16}
$$

The dissolved mineral mass extracted from the dissolution system m_{E} is of high interest in the design of dissolution mining systems. Assuming that the inlet and outlet flux remain constant and steady over τ, m_{E} can be approximated as,

$$
m_{\mathrm{E}} = \left(\int_{\Gamma_{\mathrm{out}}} \Phi_{\mathrm{out}} \rho_{\mathrm{out}} \mathbf{U}_{\mathrm{out}} \cdot \mathbf{n} d\Gamma - \int_{\Gamma_{\mathrm{in}}} \Phi_{\mathrm{in}} \rho_{\mathrm{in}} \mathbf{U}_{\mathrm{in}} \cdot \mathbf{n} d\Gamma \right) \tau
\tag{3.17}
$$

It follows that the mass of mineral stored in the brine is,

$$
m_{\mathrm{S}} = m_{\mathrm{D}} - m_{\mathrm{E}}
\tag{3.18}
$$

3.2.5 Boundary conditions

The boundary conditions required to solve the mineral dissolution problem are described in this section. At the inlet, Γ_{in}, freshwater is injected. Well-developed velocity distribution of the steady laminar fluid flow at the inlet is assumed. Compared to a plug flow (constant) velocity profile, a parabolic profile reduces the sharp change of velocity near the dissolution

37

front close to the inlet and enhances the stability of the model. It is expected that the influence of the choice of the inlet velocity profile on the dissolution process will decrease with distance from the inlet. The boundary conditions along the inlet boundary, with an aperture of $2w$, are,

$$\mathbf{U}(\mathbf{x}) \cdot \mathbf{n} = U_{\max} \left(1 - \frac{y^2}{w^2} \right) \qquad \forall \, \mathbf{x} \in \Gamma_{in}$$
$$\Phi(\mathbf{x}) = 0 \qquad \forall \, \mathbf{x} \in \Gamma_{in}$$

(3.19)

in which $U_{\max}$ is the maximum velocity magnitude of the well-developed flow [m/s] and y denotes the vertical coordinate along the inlet boundary [m].

The pressure of brine is set to be equal to the atmospheric pressure, $P_0 = 101$ kPa, at the outlet (Γ_{out}). The gradient of the dissolved mineral mass fraction at the outlet is equal to zero, so the condition of zero diffusion flux is applied,

$$p(\mathbf{x}) = P_0 \qquad \forall \, \mathbf{x} \in \Gamma_{out}$$
$$[D_{\mathrm{f}} \nabla (\rho \Phi)] \cdot \mathbf{n} = 0 \qquad \forall \, \mathbf{x} \in \Gamma_{out}$$

(3.20)

It is noteworthy that while the diffusive mass flux of the mineral is prescribed to be zero at the boundary, the advective flux is still non-zero. Dissolution occurs along the solid-brine interface, Γ_{d}. The dissolution front is assumed to be a no-slip boundary when computing the brine flow, and the relative brine flow velocity on the dissolution front is assumed to be

zero. So, the brine velocity on the boundary is defined as $\mathbf{U}(\mathbf{x}) = \mathbf{0}$. Thus, $\mathbf{U} \cdot \mathbf{n} \neq v_d$ on the dissolution front; however, since the dissolution rate (v_d) is extremely small compared to the average brine velocity in the cavity/cavern (discussed in Chapter 2), this inconstancy is deemed acceptable. The mineral behind the dissolution front is assumed to be pure and soluble, and there are no insoluble obstacles. Also, the dissolved mineral is assumed to be saturated on the dissolution front with a mass fraction of 0.264 [54],

$$
\begin{aligned}
\mathbf{U}(\mathbf{x}) &= \mathbf{0} && \forall \, \mathbf{x} \in \Gamma_d \\
\Phi(\mathbf{x}) &= 0.264 && \forall \, \mathbf{x} \in \Gamma_d
\end{aligned}
\tag{3.21}
$$

3.3   Numerical algorithms

This section describes the algorithms used to couple the solution of brine flow, dissolved mass transfer, and dissolution boundary movement. It also describes the novel algorithm for updating the dissolution front and an algorithm for smoothing the dissolution rate to increase the robustness of the model.

3.3.1   Main coupling algorithm

The main algorithm, illustrated in Figure 3.3, is an iterative scheme comprised of three main modules to: 1) generate the geometry and mesh, 2) solve the fluid flow and mass transfer equations, and 3) calculate the evolution of the dissolution front. A new python program is developed to transfer information between each module and iterate over each timestep. A description of the three modules is given below.
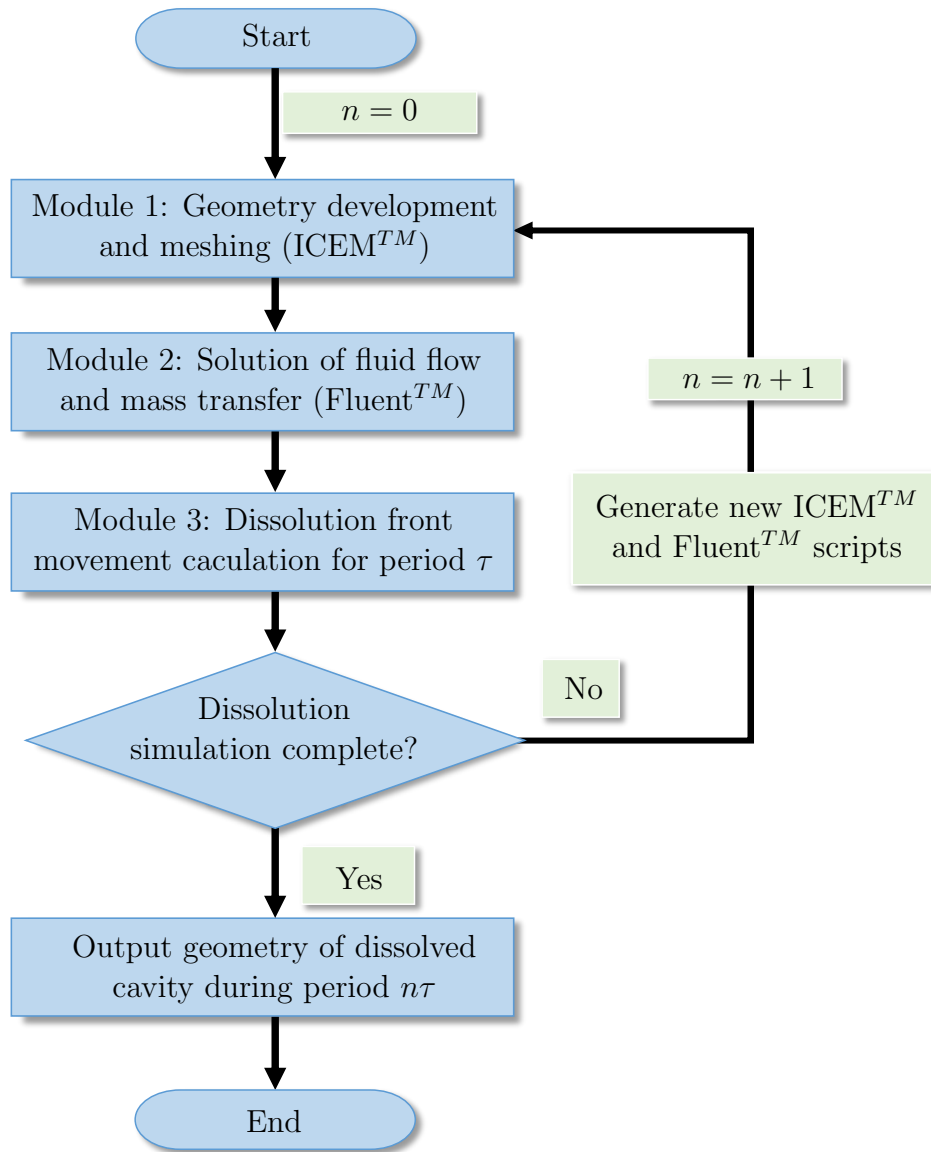
Figure 3.3: Sketch of main algorithm.

1) The geometry of the cavity and corresponding mesh is first generated with the ANSYS ICEM^{TM} software. The mesh used to discretize the domain conforms to the geometry of the cavity and is updated with each timestep. An approximately constant element size is maintained in the mesh with each update of the geometry.

2) The mesh data is transferred to the second module to solve the brine flow and mass transfer equations within the dissolution cavity. The governing equations (3.10-3.12) with changing brine density (3.4) are solved using Fluent^{TM}, a commercial software based on the finite volume method (FVM). The nonlinear discrete equations are iteratively solved using the Semi-Implicit Method for Pressure Linked Equations (SIMPLE) algorithm. The SIMPLE algorithm solves the continuity and Navier–Stokes equations (3.10-3.11) to provide the fluid velocity and pressure. Subsequently, the mass transfer equation (3.12) is solved to obtain the mass fraction of dissolved mineral; the brine density is updated with (3.4), and the solution algorithm is iterated until a converged solution is obtained.

3) Once the fluid velocity and mass concentration in the cavity are obtained, the files from the Fluent^{TM} simulation are transferred to the next module to carry out dissolution front movement calculations. The movement of the dissolution front is calculated by a new developed program, which outputs a data file with the updated geometry information. The algorithm for the dissolution front movement is described in Section 3.3.2. Once the dissolution front movement has been computed, the updated boundary information is written into the ICEM^{TM} script by the developed program. The updated ICEM^{TM} script is then ready to be called to generate the new geometry and mesh for the next timestep in the brine flow simulation. The Fluent^{TM} script is also updated to reflect the geometry change.

The geometry development, the brine flow and mass transfer simulation, and the dissolution front update are repeated for each timestep.

The current approach may be compared to the common front-tracking method – ALE, as discussed in Chapter 2. In the ALE approach, the evolution of the mesh (including mesh boundaries), which describes dissolution fronts, is explicitly coupled to the governing equations of the fluid inside the cavity. In other words, at each time step, the velocity of the dissolution front is determined at the same time as the velocity, density, and pressure of the brine. As a result, the ALE model rigorously describes the evolution of the dissolution front; however, this is achieved at a significant computational cost due to the need to solve a more highly coupled system of equations. Furthermore, as the cavity grows, remeshing is periodically needed to refine the mesh to avoid highly distorted elements.

In the proposed work, it is recognized that the dissolution front evolves very slowly, so the solution of the velocity, the density, and the pressure of the brine can be determined independently (decoupled) from the evolution of the dissolution front. The advantage of this approach over ALE is that the decoupled equations are much easier to solve and significantly larger domains and time step sizes are possible. For example, in previous efforts to model similar problems with ALE, the simulations were limited to extremely small domains (10^{-7}) m^2 and small time steps (1 s). This may be compared to the systems simulated here (as discussed in Section 3.4) of 10^{-4} m^2 using a time step size of 10^2 s.

3.3.2 Dissolution front evolution algorithm

The third module of the program uses the output of the fluid simulation to compute the dissolution front evolution, as shown in Figure 3.4. First, the dissolution rate, v_d, is calculated for each boundary element using (3.13). The gradient of the mineral mass fraction is calculated using the Green-Gauss cell-based method. The dissolution rate can be set to zero if the dissolution front reaches an insoluble obstacle; however, the presence of insoluble obstacles would necessitate more complex algorithms to update the topology of the front. Such complexities have not been considered in the current work. The dissolution rate is then smoothed to reduce the oscillations that appear in the gradient. This smoothing process increases the robustness of the algorithm and allows for the use of coarser meshes. The calculation of the smoothed dissolution rate ($\overline{v_d}$) is discussed in Section 3.3.3. Given the dissolution timestep, τ, the smoothed dissolution front movement distance is then calculated as,

$$\Delta \overline{H} = \overline{v_\mathrm{d}} \tau \tag{3.22}$$

Finally, the geometry of the dissolution boundary is updated based on the dissolution front distance. A sketch of the dissolution front updating approach is shown in Figure 3.5. The smoothed normal dissolution distance is applied to the center point of the boundary element, and the normal direction is calculated based on the location of the previous dissolution front boundary nodes. The moving distance of each boundary element center in the x- and y-directions is calculated as,

$$
\begin{aligned}
\Delta x^\mathrm{I} &= \frac{y_n^\mathrm{i} - y_n^\mathrm{i+1}}{\sqrt{\left(x_n^\mathrm{i+1} - x_n^\mathrm{i}\right)^2 + \left(y_n^\mathrm{i+1} - y_n^\mathrm{i}\right)^2}} \Delta \overline{H} \\
\Delta y^\mathrm{I} &= \frac{x_n^\mathrm{i+1} - x_n^\mathrm{i}}{\sqrt{\left(x_n^\mathrm{i+1} - x_n^\mathrm{i}\right)^2 + \left(y_n^\mathrm{i+1} - y_\mathrm{n}^\mathrm{i}\right)^2}} \Delta \overline{H}
\end{aligned}
\tag{3.23}
$$
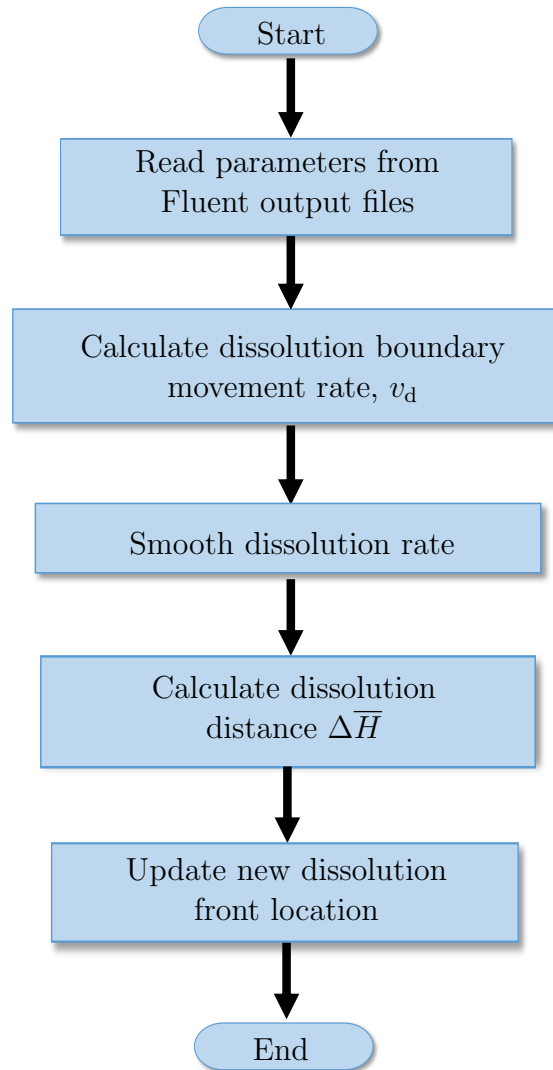
Figure 3.4: Dissolution front movement algorithm.

in which Δx^{I} and Δy^{I} are the displacement in the x- and y-directions of the midpoint of boundary element I [m], y_n^{i} and $y_n^{\mathrm{i+1}}$ denote the y-coordinates of boundary nodes i and $\mathrm{i}+1$, and x_n^{i} and $x_n^{\mathrm{i+1}}$ represent the x-coordinates of boundary nodes i and i $+1$.

The new dissolution front is obtained by connecting the updated boundary center points with a spline function. The new geometry and mesh are generated using ICEM^{TM}.
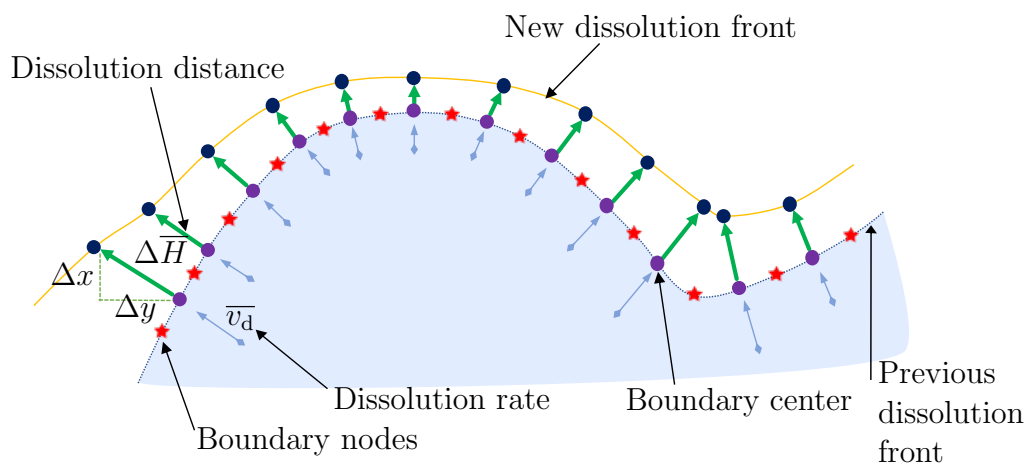
Figure 3.5: Schematic illustration of the dissolution front movement.

The approaches used in the proposed model to characterize the moving interface can be classified as a front tracking method because the movement of the dissolution front is tracked explicitly. It is different from some other methods which use implicit strategies to capturing the moving interface, such as level sets and the phase field method, which have been widely applied to multi-phase flow, and solidification problems [66, 67].

45

3.3.3 Dissolution Rate Smoothing

The dissolution rate is proportional to the gradient of the dissolved mineral mass fraction near the dissolution front, and the mass fraction gradient is approximated using the Green-Gauss cell-based method. As a result, the velocity of the front is subject to small numerical perturbations, which can grow into large spurious oscillations along the dissolution front. These numerical disturbances may be reduced with mesh refinement and/or with a smoothing algorithm as described below. A comparison of the dissolution rate before and after using the smoothing algorithm is shown in Figure 3.6, demonstrating the successful elimination of perturbations.
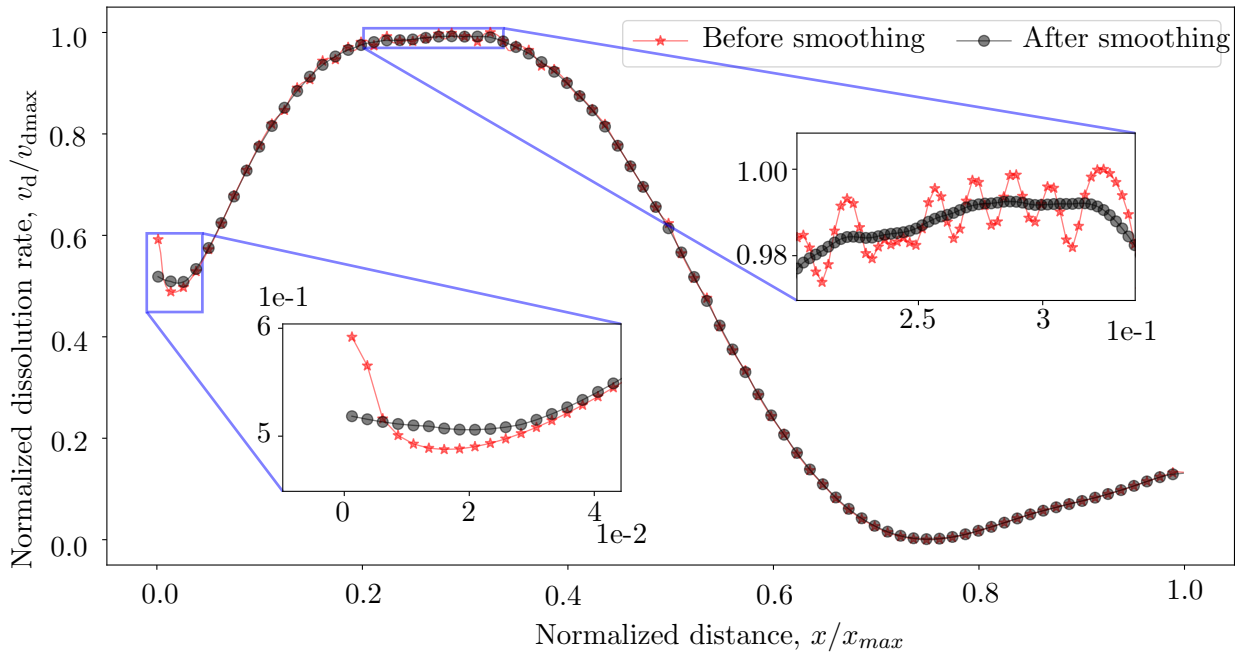
Figure 3.6: Boundary dissolution rate distribution before and after smoothing.

Before starting the smoothing calculation, a smoothing radius, r, and the number of

smoothing iterations, s_n, are predefined based on user experience. For each cell on the dissolution front, the distances between neighboring boundary cells' center points and the center of the boundary cell in question are calculated. All cells within a distance r of the center of the boundary cell are included in the smoothing calculation. A sketch of how the smoothing area is defined is shown in Figure 3.7.
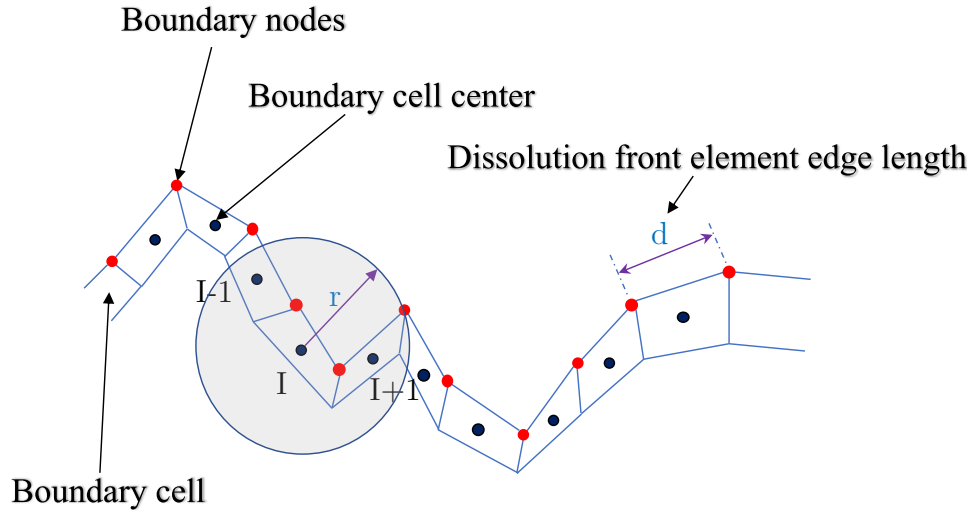
Figure 3.7: Sketch of dissolution rate smoothing area identification.

The main part of the smoothing algorithm is the calculation of the weighted average of the dissolution rate. The length of the boundary edge of the dissolution front element is selected as the weight. The averaged (smoothed) dissolution rate of boundary element I [m/s] is given as,

$$\overline{v_{\mathrm{d}}^{\mathrm{I}}} = \frac{\sum_{\mathrm{J}=1}^{\mathrm{N}} v_{\mathrm{d}}^{\mathrm{J}} d^{\mathrm{J}}}{\sum_{\mathrm{J}=1}^{\mathrm{N}} d^{\mathrm{J}}} \tag{3.24}$$

in which N represents the number of boundary elements involved in the smoothing calculation, $v_{\mathrm{d}}^{\mathrm{J}}$ is the dissolution rate of each boundary element, J, in the averaging radius

47

Table 3.1: Material Properties

Parameter	Variable	Value	Unit
Dynamic viscosity	μ	10^{-3}	Pa/s
Density of salt rock	ρ_s	2170	kg/m^3
Density of water	ρ_w	1000	kg/m^3
Diffusion coefficient in brine	D_s	10^{-9}	m^2/s
Diffusion coefficient near dissolution front	D_f	10^{-9}	m^2/s

[m/s], and d^J is the length of the boundary edge of the dissolution element involved in the smoothing calculation [m].

The smoothing calculation is performed for all the dissolution front elements. Then, the dissolution rate of each element is updated ($v_\mathrm{d}^\mathrm{I} = \overline{v_\mathrm{d}^\mathrm{I}}$ for all I) and the smoothing calculation process for all the elements is repeated until the iteration number s_n is reached. The flow chart of the dissolution rate smoothing algorithm is demonstrated in Figure 3.8.

3.4 Numerical Simulation

In this section, a numerical case study of mineral dissolution is conducted. Convergence of the model is first verified (Section 3.4.1), followed by a discussion of fluid flow and dissolution patterns (Section 3.4.2) and the influence of Peclet number on the results (Section 3.4.3). The material parameters used for the simulation are listed in Table 3.1.

The initial geometry is a rectangle with width $2w$ and length l. The inner zone of the geometry is the brine-filled cavity and mineral dissolution occurs along the dissolution front, Γ_d. Freshwater is injected along Γ_in and Γ_out is the brine outlet. Since gravity is

Start

$s_{\mathrm{i}} = 0$

$I = 1$

Locate all cells within
radius r of cell I
(computed with cell centers)

$\overline{v_{\mathrm{d}}^{\mathrm{I}}} = \dfrac{\sum_{\mathrm{J}=1}^{\mathrm{N}} v_{\mathrm{d}}^{\mathrm{J}} d^{\mathrm{J}}}{\sum_{\mathrm{J}=1}^{\mathrm{N}} d^{\mathrm{J}}}$

I = I+1

no

All boundary
cells computed?

yes

$s_{\mathrm{i}} = s_{\mathrm{i}} + 1$

Update dissolution rate
$v_{\mathrm{d}}^{I} = \overline{v_{\mathrm{d}}^{I}} \, \forall \, I$

yes

$s_{\mathrm{i}} < s_{\mathrm{n}}$?

no

End
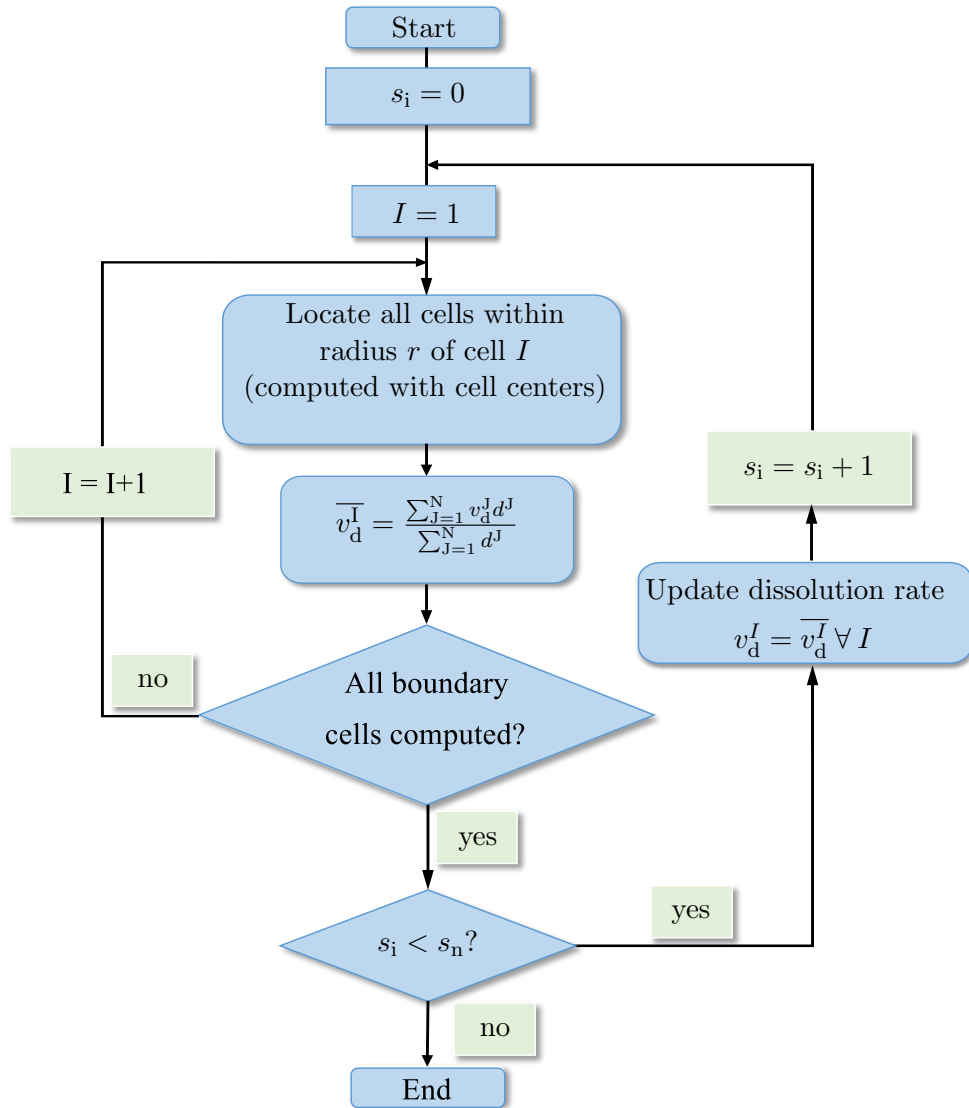
Figure 3.8: Boundary dissolution rate smoothing algorithm.

ignored (discussed in Section 3.2), the model is symmetric and the top half of the domain is modeled as shown in Figure 3.9. The bottom edge, Γ_b, is the symmetric axis along which the shear stress vanishes. In addition to the boundary conditions stipulated in Section 3.2.5, the bottom boundary, Γ_b, is subject to zero normal brine velocity, zero shear stress, and zero diffusion flux of mineral,

$$\mathbf{U}(\mathbf{x}) \cdot \mathbf{n} = 0 \qquad \forall\, \mathbf{x} \in \Gamma_b$$
$$\mu \left[\nabla\mathbf{U} + (\nabla\mathbf{U})^{\mathrm{T}} \right] \cdot \mathbf{n} = \mathbf{0} \qquad \forall\, \mathbf{x} \in \Gamma_b \qquad (3.25)$$
$$-\mathbf{n} \cdot \left[-D_{\mathrm{f}}\nabla(\rho\Phi) \right] = 0 \qquad \forall\, \mathbf{x} \in \Gamma_b$$
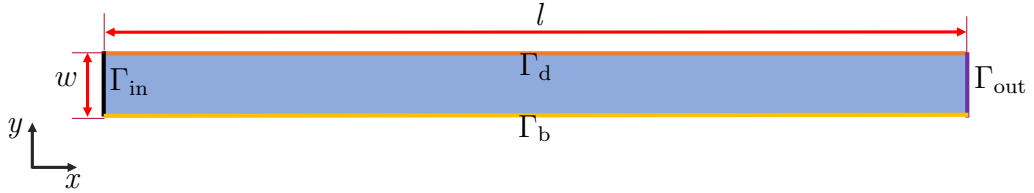
Figure 3.9: Initial cavern geometry for numerical simulation.

3.4.1 Model Verification

The model is verified using a convergence analysis. Verification against an analytical solution, while desirable, was not possible since the analytical solution for this nonlinear problem does not exist. Validation of the model against laboratory or field experiments still remains to be accomplished, but is beyond the scope of this manuscript. The geometry is shown in Figure 3.9, with $w = 0.001$ m and $l = 0.1$ m. The magnitude of the maximum velocity, U_{max}, is 0.01 m/s. The simulation employs a structured mesh of quadrilateral cells.

It is recognized that the total domain size is orders of magnitude smaller than a typical salt cavern. However, the domain used here is much larger than the models that can be simulated using existing algorithms, which try to solve the coupling problem of brine and dissolved mineral mass conservation, full Navier-Stokes equations, and nonlinear moving boundary evolution equations, unless one resorts to the introduction of a very large amount of unphysical artificial damping or using small-scale domain with a fine mesh (see COMSOL simulations in Chapter 2), or resorts to models with low Reynolds Number in order to neglect the inertia force in the momentum conservation equations (such as diffuse interface models [45]). From this point of view, the model here is the first step. Further, accurate simulation of large caverns will require the introduction of gravity-driven flow which is neglected in the current model and significantly complicates modelling efforts. The convergence of the model with mesh and times step size reduction is shown in Figure 3.10. For mesh convergence, a reference model with element size $s_0 = 6 \times 10^{-10}$ m^2 is used. A reference model with timestep size $T_{s0} = 100$ s is used to check the time convergence. A normalized L$_2$ difference norm is calculated to verify the convergence trend,

$$
R_{\Delta\overline{H}l2} = \left(\frac{\int\limits_{\Gamma_d} \left(\Delta\overline{H}_{\mathrm{rs}} - \Delta\overline{H} \right)^2 d\Gamma}{\int\limits_{\Gamma_d} \Delta\overline{H}_{\mathrm{rs}}^2 d\Gamma} \right)^{1/2} \tag{3.26}
$$

in which $R_{\Delta\overline{H}l2}$ is the L$_2$ difference norm between model results and reference results, $\Delta\overline{H}_{\mathrm{rs}}$ denotes the moving distance of solid-brine interface in the reference model [m], and $\Delta\overline{H}$ denotes the dissolution distance of the solid-brine interface [m].

The results of the convergence analysis in Figure 3.10 show that the error in the dissolution

51
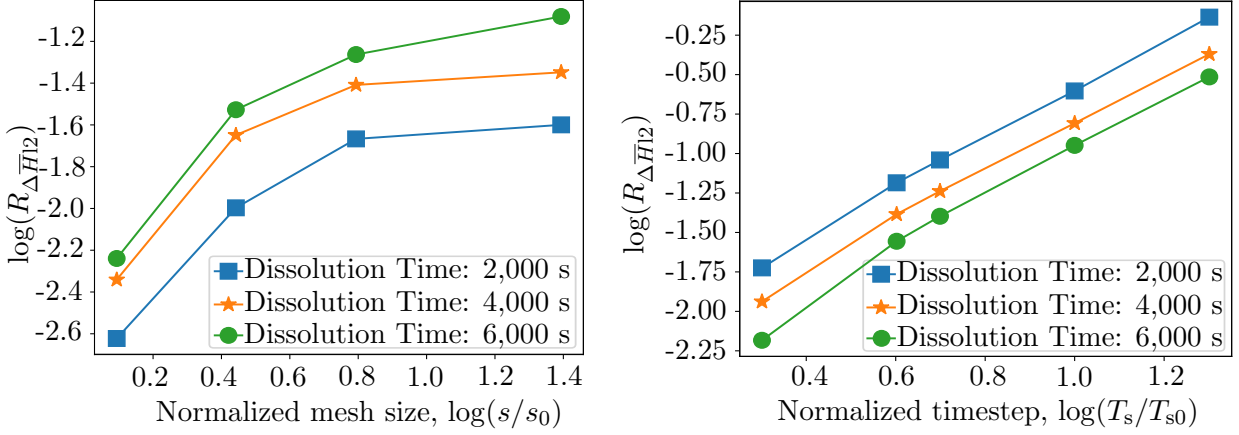
Figure 3.10: The L2 difference norm for mesh refinement (left) and temporal refinement (right).

distance decreases when the mesh size of the model gets close to the reference model for each dissolution time. The results of the time convergence analysis have a similar trend. It can be concluded that the proposed dissolution model is self-consistent.

3.4.2 Fluid Flow and Dissolution Pattern

The fluid flow, mass transfer, and dissolution cavity geometry evolution during dissolution are presented and discussed in this section. The geometry parameters for the simulation are set to $l = 0.1$ m and $w = 0.001$ m. At each time step, a new structured mesh of cells is generated, conforming to the new dissolution interface. The average size of the quadrilateral cells in the mesh is 6×10^{-10} m^2. The number of cells in the initial geometry mesh is 1.3×10^5 and increases with the expansion of the cavity. In the last step of the simulation, there are 5.8×10^5 cells. The magnitude of the maximum inlet velocity ($U_{\max}$) is 0.01 m/s, resulting in a Reynolds number, R_e, of 10, and Peclet number, P_e of 10^6. The timestep

for the dissolution front movement used in the simulation is 100 s. The total number of time steps is 1000 and the total simulated time is 100,000 s ($\approx$ 28 hrs). It is noted that the simulated time herein is significantly larger than can be achieved with existing models without resorting to modeling the process as a diffusion dominated process instead of as an advection dominated process.

The flow pattern undergoes a significant change with the cavity enlargement, as shown in Figure 3.11. At the start of freshwater injection, the changes in the cavity shape due to dissolution affect the flow pattern near the inlet. This in turn affects the mineral dissolution along the new flow path, creating a coupled phenomenon that results in a vortex. The vortex then grows over time with the enlargement of the cavity caused by dissolution. The proposed model can capture this phenomenon because it solves the nonlinear physical equations of brine flow coupled with the moving dissolution front.

At the outlet, the brine flow is directed towards the centerline of the cavity. The magnitude of the brine velocity near the inlet and outlet does not undergo an obvious change over time because of the constant brine injection velocity at the inlet and the constant pressure condition at the outlet. However, the flow velocity in the middle of the cavity decreases as the cavity aspect ratio and the dissolved mineral mass in the cavity increase.

As shown in the right part of Figure 3.11, the high concentration brine is mainly located near the dissolution front (shown in red). A relatively high mass fraction zone is also generated near the inlet and expands with the dissolution process. The high mass fraction zone evolution is consistent with the evolution of the vortex. It indicates that the mass fraction distribution is mainly controlled by the brine flow velocity in the cavity (advec-
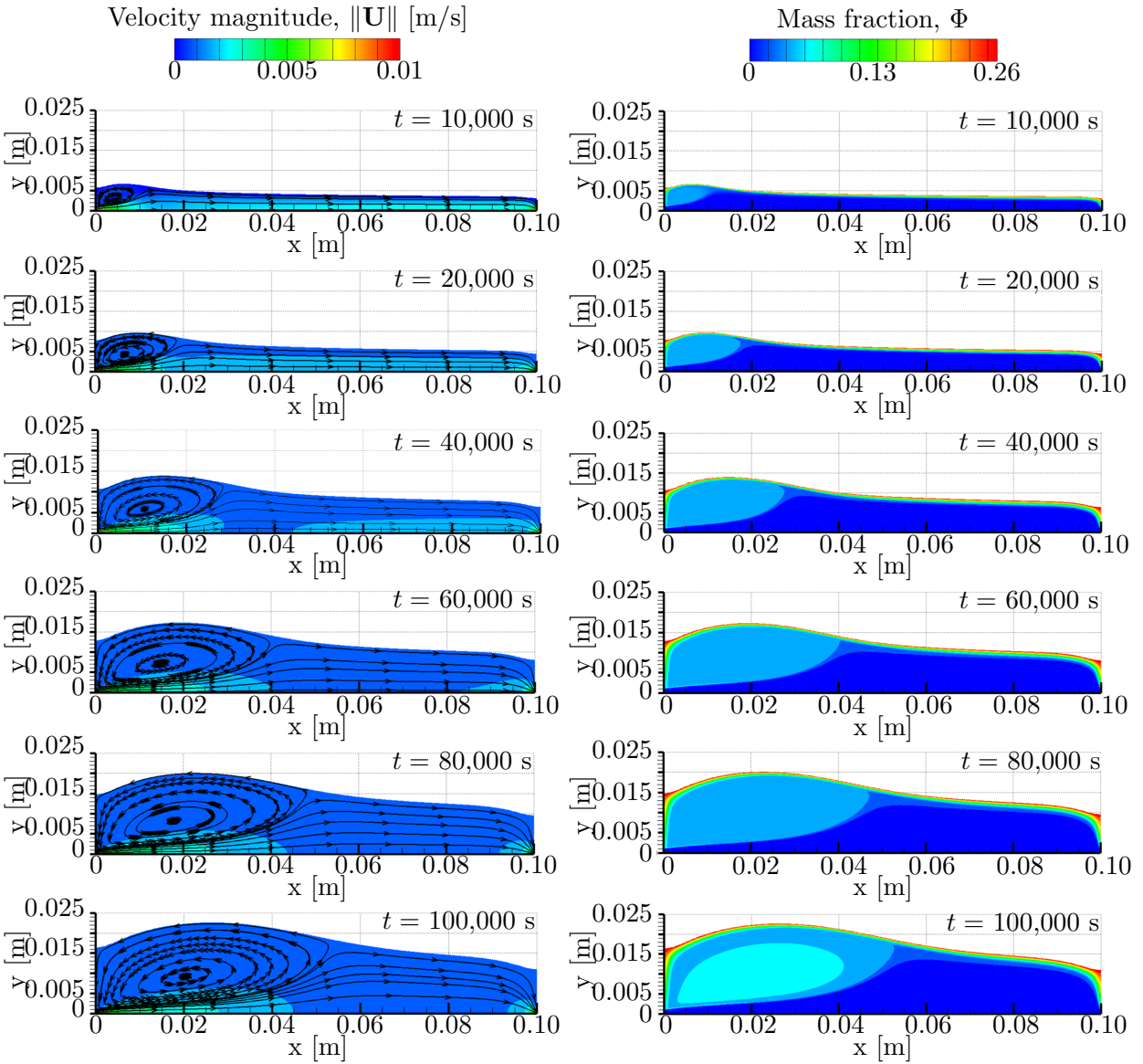
Figure 3.11: Velocity (left) and mass fraction (right) distributions after dissolution time of 10,000 s, 20,000 s, 40,000 s, 60,000 s, 80,000 s, and 100,000 s.

tion dominated). The generation of vortices increases the dissolved mineral mass trapped in the cavity. From the vortex tip to the outlet, the mass fraction near the dissolution front increases because the brine flow transports the dissolved mineral from upstream to downstream. At the outlet area, the dissolved mineral is trapped in the corners due to the lack of advection since the flow direction moves towards the centerline of the cavity.

Figure 3.12 shows the change in dissolved mineral mass at the dissolution front, m_D, the mass of dissolved mineral extracted from the cavity, m_E, and the mass of mineral stored in the brine, m_S. As the mineral is dissolved, it is transferred into the brine and transported out of the dissolution system by the continuous flow. The values of the dissolved mineral mass and the mass of transported mineral out of the cavity increase with time, and the difference (the stored mineral) also increases with time. This indicates, as expected, that a small but increasing amount of dissolved mineral is trapped and stored in the cavity. The generation of a high mass fraction zone shown in Figure 3.11 provides evidence of this phenomenon. The right part of Figure 3.12 indicates the change of dissolved mineral stored in the cavity. The mineral trapped in the cavity increases rapidly at the early stage of dissolution but tends to increase linearly after 20,000 s.

The dissolution pattern and dissolution rate at different times are explored in Figure 3.13. The cavity widens as freshwater flows into it. Due to the vortex effect, the location of the widest section of the cavity is not fixed; it moves towards the outlet during the dissolution period. The dissolution rate shows the same trend. The widening effect decreases along the flow path from the vortex tip to the outlet because the increase in brine concentration slows the rate of dissolution. The overall cavity width increases with time while the dissolution rate decreases with time. The change in the average dissolution rate over the

55

(a) Dissolved mineral mass (m_D)
and extracted dissolved mineral mass (m_E)

(b) Mineral mass stored in cavity (m_S)
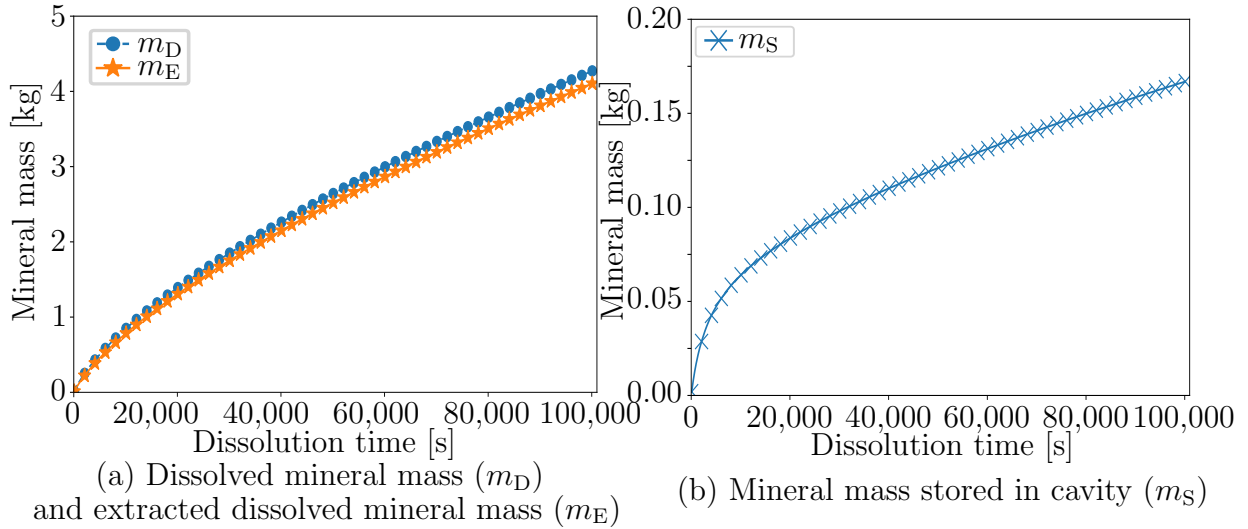
Figure 3.12: The change of mineral mass dissolved from the dissolution front and extracted from the dissolution system (a), and the evolution of mineral mass stored in the brine in the cavity (b).

dissolution period is shown in Figure 3.14. It demonstrates that the dissolution rate keeps decreasing, but the gradient decreases with time. The dissolution rate tends to a small but stable value after a long dissolution period (over 10^5 s).

To further investigate why the maximum dissolution distance and dissolution rate migrate, a snapshot of the flow pattern, mass fraction distribution, and dissolution rate distribution at $t = 50,000$ s is shown in Figure 3.15. The star marker shows the location of the maximum dissolution rate along the dissolution front. The corresponding location in the fluid flow and mass fraction distribution chart is highlighted by the red dashed line. At the tip of the vortex, the brine flows in two different directions. The diversion of flow along two directions leads to a decrease in mineral mass at the vortex tip near the dissolution front because the dissolved mineral transport is dominated by advection. It causes an increase in the mass fraction gradient at the vortex tip, not distinguishable along the front in Figure

56
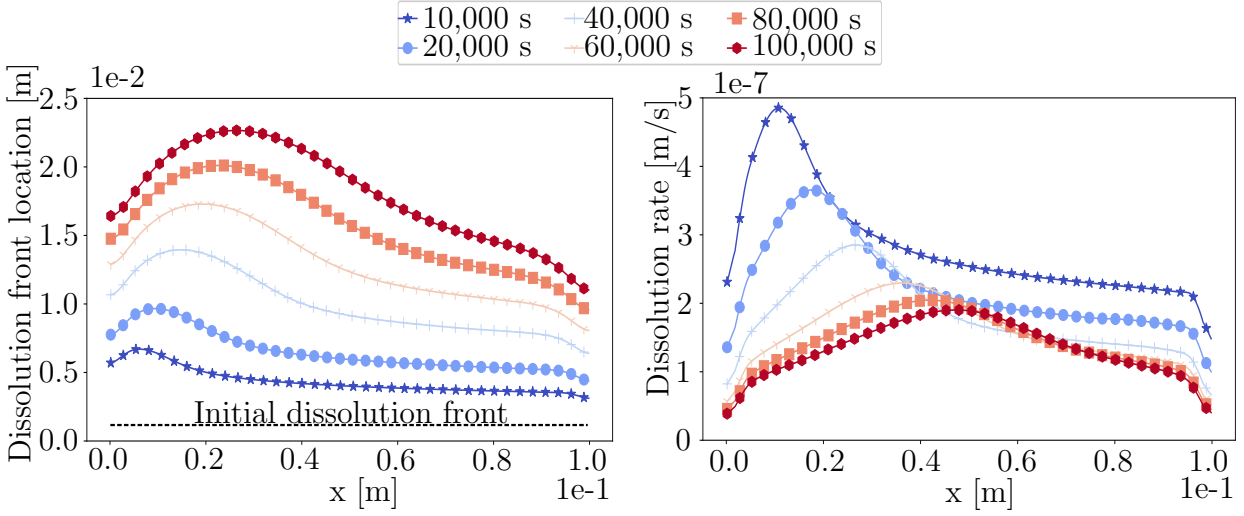
Figure 3.13: Dissolution front location (a) and dissolution rate distribution (b) during dissolution.
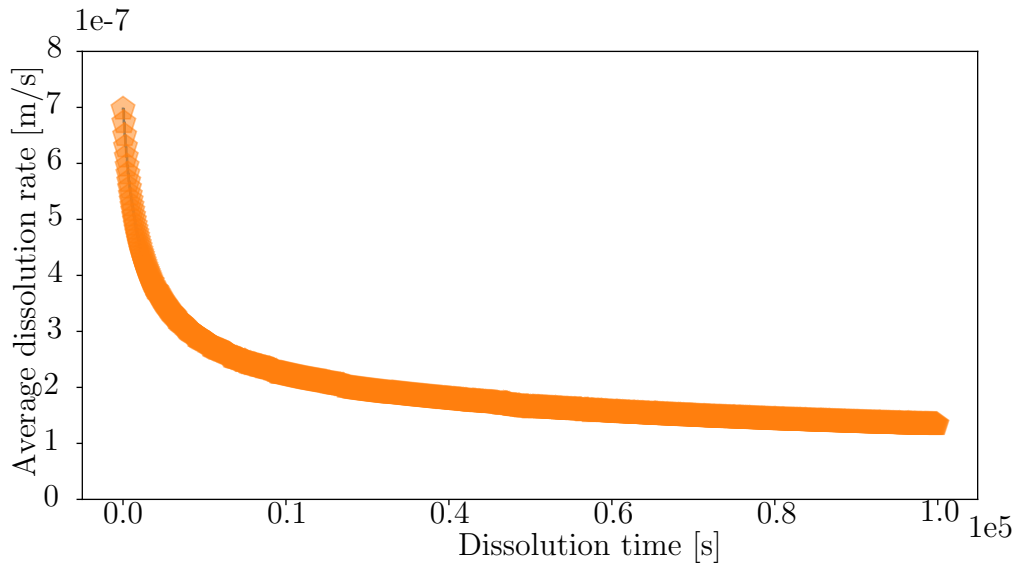
Figure 3.14: Average dissolution rate during dissolution.

3.15; but can be reflected from the general mass fraction trend along the vortex tip. As the dissolution rate is proportional to the mass fraction gradient, the maximum dissolution rate is expected to occur at the tip of the vortex. The dissolution rate distribution figure at the bottom of Figure 3.15 shows that the value and location maximum dissolution rate are accurately captured. The results show that the brine flow patterns have a non-negligible influence on the dissolution rate and the cavity topology change. The proposed model can capture this complex coupling phenomenon.
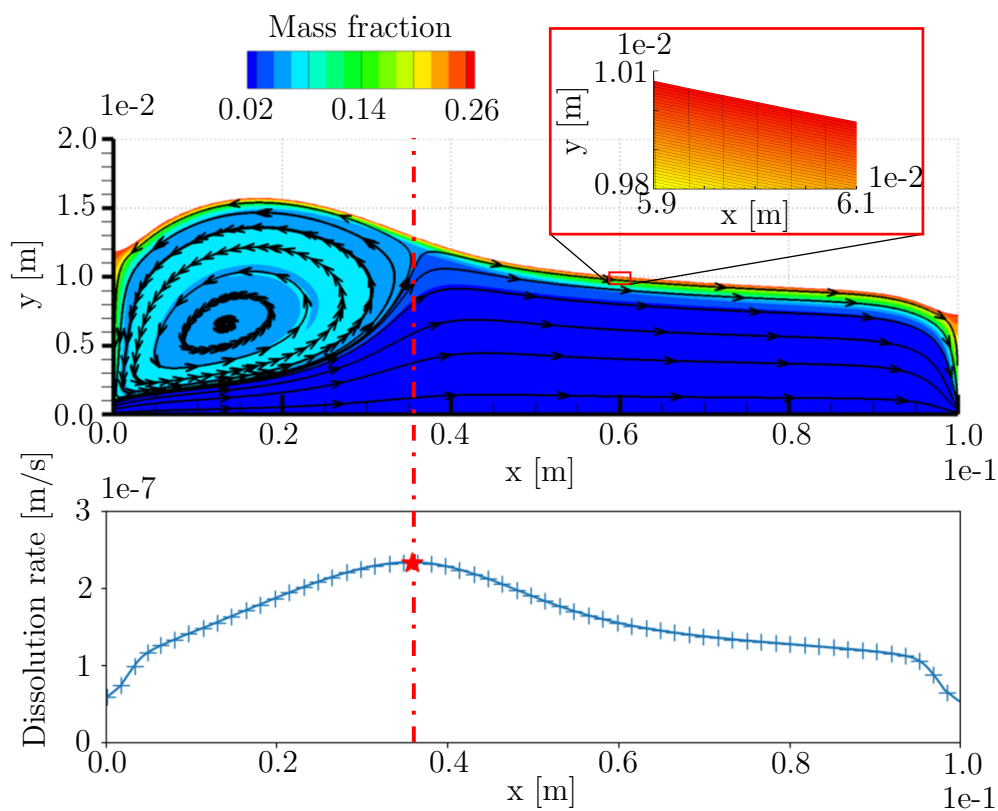
Figure 3.15: Brine flow pattern, mass fraction distribution and maximum dissolution rate location after 50,000 s of dissolution.

3.4.3 Influence of Peclet Number

In this section, the influence of the Peclet Number (P_e) on the dissolution process is discussed. The change in Peclet Number is explored by changing the inlet velocity. The geometry is selected as $w = 0.001$ m and $l = 0.1$ m. The inlet velocity is set to 0.01 m/s, 0.05 m/s, and 0.1 m/s, corresponding to Peclet Number (P_e) of 10^6, 5×10^6, and 10^7, respectively.

Figure 3.16 demonstrates the brine flow pattern and mass fraction distribution after $5,000$ s of dissolution under different P_e. The increase in P_e promotes the generation of a larger vortex in the dissolved cavity. Convection has a more obvious effect on mineral transport when P_e is high. The zone of high mineral mass fraction increases as the inlet velocity increases.

The dissolution rate and the shape of the dissolution front are also affected by an increase in Peclet number, as shown in Figure 3.17. The increase in the inlet velocity promotes higher rates of mineral dissolution, especially the dissolution near the outlet. The location of maximum dissolution along the boundary moves more rapidly in the downstream direction as the inlet velocity gets larger. However, the evolution of the dissolution rate along the dissolution boundary is more complicated. The maximum dissolution rate decreases with time when P_e is low. However, when P_e gets larger, the maximum dissolution rate moves towards the outlet region more quickly, and the maximum dissolution rate increases at the later stages of the process.
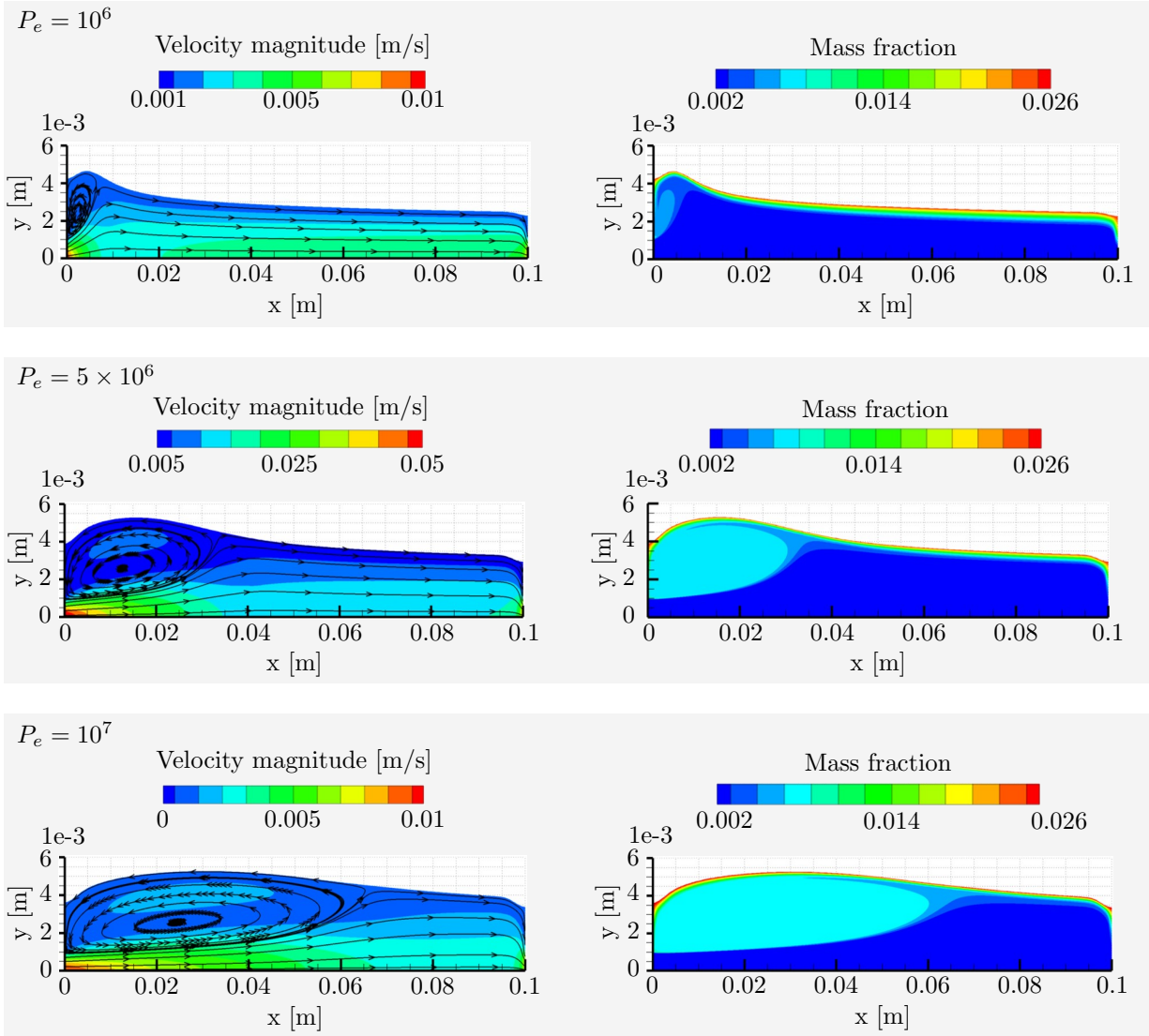
Figure 3.16: Velocity (left) and mass fraction (right) distributions at 5,000 s of different P_e.
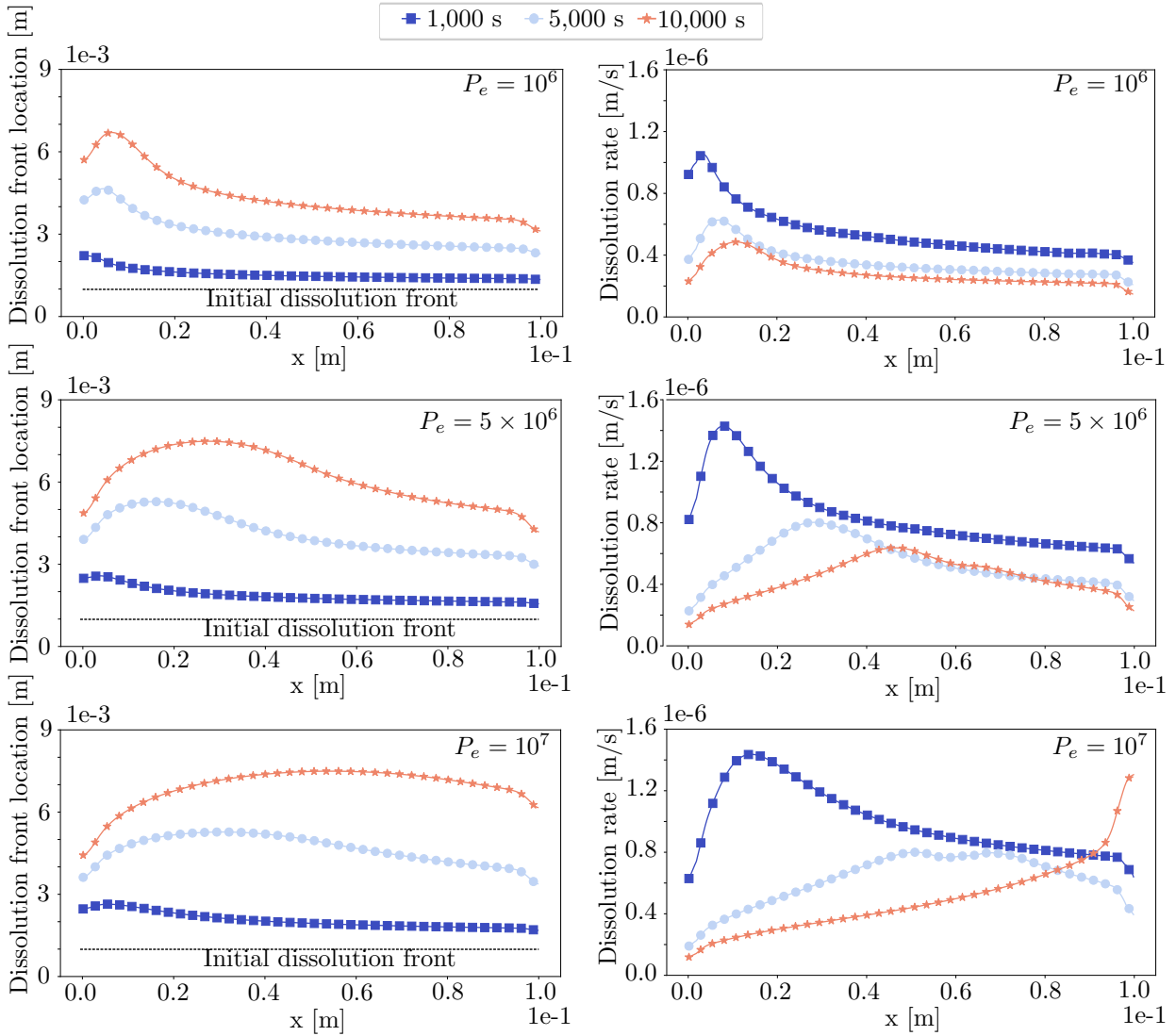
Figure 3.17: Dissolution front location (right) and dissolution rate distribution (left) under different Pe.

61

Chapter 4

Modeling and verification of non-linear mineral dissolution processes with buoyancy effects

4.1   Introduction

In the previous chapter, a model in which the dissolution front evolution is determined using a loosely coupled algorithm is presented, and it takes advantage of the scale difference between brine flow rate and dissolution rate. It makes the algorithm suitable for simulating larger domains and longer dissolution processes, but the gravitational force is ignored. In this chapter, we extend our previous model to incorporate buoyancy effects that lead to a number of algorithmic modifications and provide an initial validation of the model against preliminary laboratory experiments. We focus on the two-dimensional mineral dissolution simulation and laboratory experiments of vertical and horizontal dissolution in

this chapter. The nonlinear equations which govern the brine flow under gravity effects due to varying brine density are described in Section 4.2. In Section 4.3, new algorithms are introduced to simulate the brine flow patterns, dissolution front evolution, and coupling effects. In Section 4.4, the model is verified using a convergence analysis, and the model is validated through comparison with lab-scale experiments results of horizontal and vertical dissolution.

4.2 Governing equations

This section describes the equations that govern the process of dissolution. The proposed model involves brine flow and dissolved mineral transfer in the cavity and slowly moving cavity boundaries (dissolution fronts). The governing equations involve mass and momentum conservation of brine flow, mass conservation of dissolved minerals within the cavity, and mass conservation along the dissolving cavity boundaries during dissolution. One particular innovation in this model is that the evolution of the dissolution front is updated using the time-averaged behavior of the brine, leading to a more computationally efficient yet realistic simulation.

4.2.1 Brine flow and dissolved mineral transfer

During dissolution, the brine and blanket fluid (air or oil) fill the dissolved cavity. In this proposed model the blanket fluid is not considered, so brine is the only fluid explicitly modelled. An example of brine flow in a horizontal cavity is illustrated in Figure 4.1. Fresh water flows into the cavity from the inlet, dissolving the minerals from the dissolution fronts, and the brine containing the dissolved minerals is discharged from the outlet.
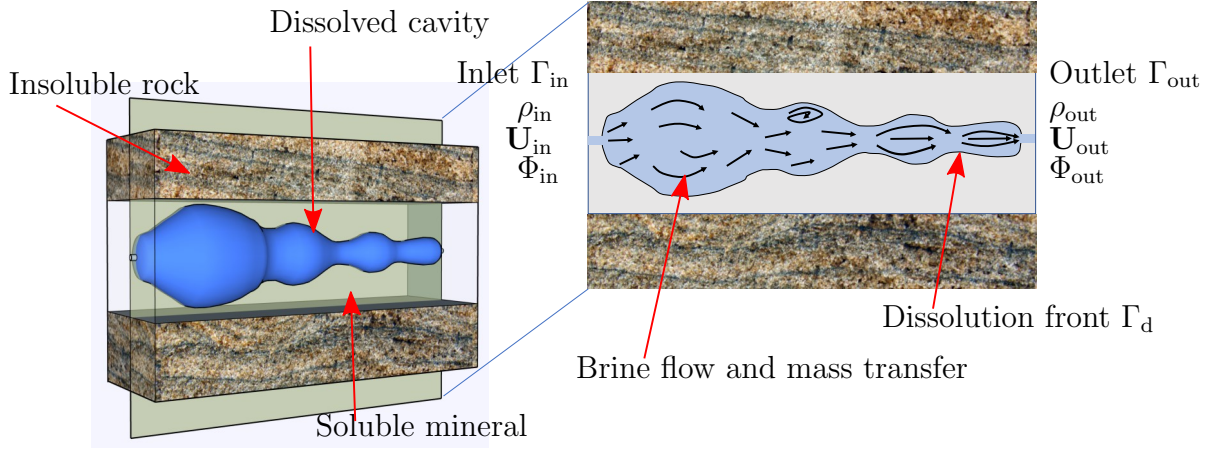
Figure 4.1: Sketch of the brine flow in the dissolved cavity.

Consider a two-dimensional fluid domain; the brine flow is governed by the conservation of mass and momentum. The brine is assumed to be a Newtonian fluid. Letting ρ denote the brine density [kg/m³], $\mathbf{V}$ the brine flow velocity, [m/s], p the brine pressure [Pa], μ the brine dynamic viscosity [Pa · s], $\mathbf{I}$ the identity tensor, and $\mathbf{g}$ the gravity acceleration [m/s²], the governing equations are,

$$\frac{\partial \rho}{\partial t} + \nabla \cdot (\rho \mathbf{V}) = 0 \tag{4.1}$$

$$\frac{D}{Dt}(\rho \mathbf{V}) = -\nabla p + \nabla \cdot \left[\mu \left(\nabla \mathbf{V} + (\nabla \mathbf{V})^{\mathrm{T}} - \frac{2}{3} (\nabla \cdot \mathbf{V}) \mathbf{I} \right) \right] + \rho \mathbf{g}. \tag{4.2}$$

The mechanical pressure is assumed to be equal to the thermodynamic pressure of the brine; thus, the bulk viscosity is zero, and the bulk viscosity term in the Navier–Stokes equations is ignored.

Transporting dissolved minerals within the cavity involves both advection and diffusion

[56]. Conservation of mass of the dissolved minerals is governed by

$$\frac{\partial}{\partial t}\left(\rho\Phi\right) + \nabla \cdot \left(\mathbf{V}\rho\Phi\right) = -\nabla \cdot \left(-\rho D_{\mathrm{s}}\nabla\Phi\right) \tag{4.3}$$

where Φ is the mineral mass fraction in the fluid, and D_{s} denotes the mineral mass diffusion coefficient $[\mathrm{m^2/s}]$.

Density change introduces nonlinearity into the governing equations (4.1-4.3), and density differences result in buoyancy forces. The brine density can be defined in terms of mineral mass fraction in the brine Φ, the mineral density ρ_{s} $[\mathrm{kg/m^3}]$, and the density of water ρ_{w} $[\mathrm{kg/m^3}]$, and can be expressed as,

$$\rho = \rho_{\mathrm{w}}(1 + b) \tag{4.4}$$

where $b = \frac{\left(1 - \frac{\rho_{\mathrm{w}}}{\rho_{\mathrm{s}}}\right)}{\frac{1}{\Phi} + \frac{\rho_{\mathrm{w}}}{\rho_{\mathrm{s}}} - 1}$. Equation 4.4 enables the proposed model to be broadly applicable to different minerals, as discussed in Chapter 3.

4.2.2   Dissolution front evolution

The mineral dissolving process takes place at the solid-liquid interface between the solid mineral and the brine. The driving force behind the dissolution is the difference between the mineral concentrations in the brine and the solid mineral rock. The dissolution process is assumed to occur on an interface that is zero-thickness, called the dissolution front. The dissolution process on vertical dissolution fronts is illustrated in Figure 4.2.
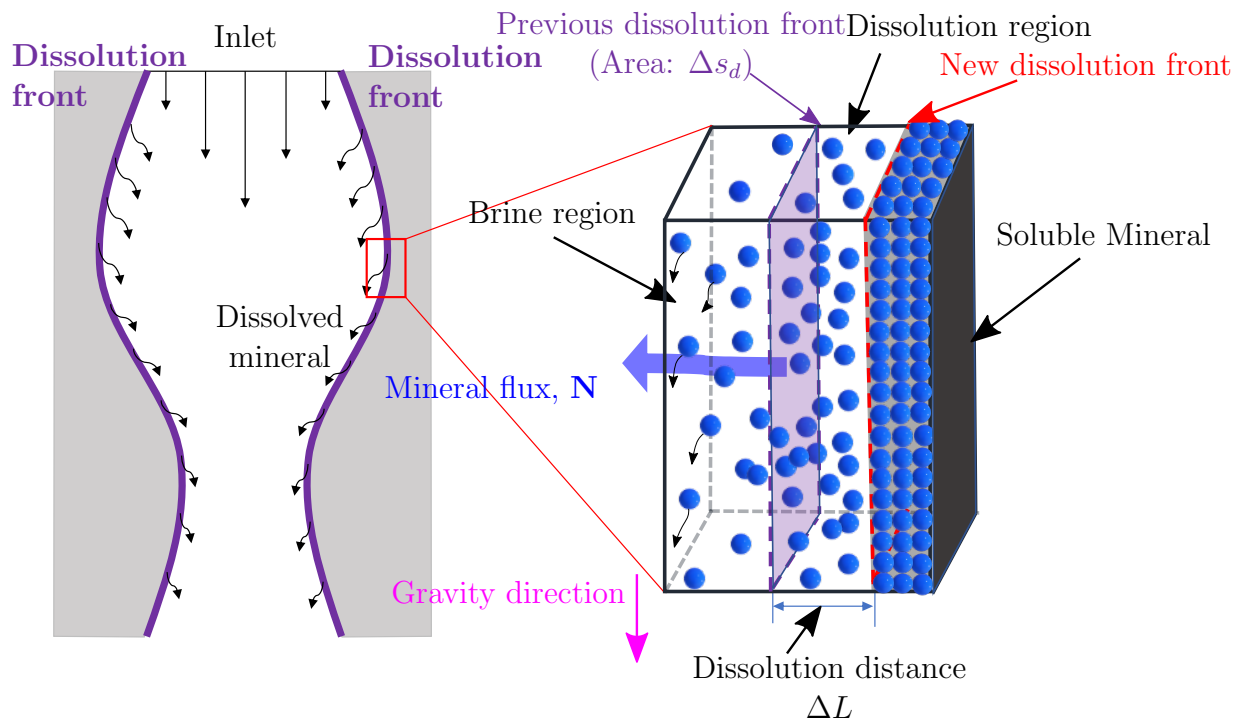
Figure 4.2: Schematic of the dissolution process in macro (left) and micro (right) scale. The brine enters the cavity from the inlet, dissolves and transports away the dissolved mineral. The dissolved mineral is transferred to brine with flux **N** from the dissolution front. A new dissolution front is generated at a distance of ΔL from the previous one after continuous dissolution for period Δt.

$\mathbf{N}$ represents the flux of dissolved mineral [mol/m^{2}s], Δs_d denotes the surface area of the dissolution front [m^2], and ΔL is the dissolution front moving distance [m] after the dissolution time Δt [s]. The mass of the mineral dissolved from the dissolution front is equal to the mass transferred into the brine in the cavity; the local mass conservation can be expressed as,

$$\Delta s_\mathrm{d} \Delta t \mathbf{N} \cdot \mathbf{n} = \frac{\rho_\mathrm{s}}{M} \Delta L \Delta s_\mathrm{d} \tag{4.5}$$

where $\mathbf{n}$ denotes the outwards normal of the dissolution front, and M represents the mineral molar mass [kg/mol].

The dissolved mineral flux $\mathbf{N} = -D_\mathrm{f} \nabla c + c \mathbf{U}'$, and c represents the molar concentration of dissolved mineral in brine [mol/m^3] and $c = \frac{\rho_\mathrm{w}}{M\left(\frac{1}{\phi} + \frac{\rho_\mathrm{w}}{\rho_\mathrm{s}} - 1\right)}$, D_f is the diffusion coefficient of the dissolved mineral close to the dissolution front [m^2/s], the value of D_f is related to the property of the solid mineral, and $\mathbf{U}'$ is the brine flow velocity relative to the dissolution front [m/s].

Following the derivation in Chapter 3, the dissolution rate is,

$$v_\mathrm{d} = \frac{\rho_\mathrm{w}}{\rho_\mathrm{s} \Phi^2 \left(\frac{1}{\Phi} + \frac{\rho_\mathrm{w}}{\rho_\mathrm{s}} - 1\right)^2} \left(-D_\mathrm{f} \nabla \Phi\right) \cdot \mathbf{n}. \tag{4.6}$$

A particular innovation of this model for mineral dissolution is the recognition that the time scales of dissolution and brine flow are significantly different, as observed in both laboratory and field studies [68, 69], and the brine flow velocity is much faster than the dissolution rate [70]. A quasi-steady condition will be achieved during the dissolution in

a short time, t^{ss}[63]. It is possible to assume that the dissolving mineral front velocity is constant over a long period, τ, which is longer than the period to reach quasi-steady-state dissolution conditions, i.e. $\tau \gg t^{ss}$. Thus it is possible to revise the mineral dissolution rate equation (6) in terms of the time-averaged mass fraction distribution near the front. The equation for the dissolution rate can then be rewritten as,

$$v_{\mathrm{d}}' = \frac{\rho_{\mathrm{w}}}{\rho_{\mathrm{s}} \overline{\Phi}^2 \left(\frac{1}{\overline{\Phi}} + \frac{\rho_{\mathrm{w}}}{\rho_{\mathrm{s}}} - 1 \right)^2} \left(-D_{\mathrm{f}} \nabla \overline{\Phi} \right) \cdot \mathbf{n} \tag{4.7}$$

in which $\overline{\Phi}$ is the time-averaged dissolved mass fraction.

The distribution of averaged brine fluid properties is calculated as

$$\overline{\beta(\mathbf{x})} = \frac{\int_{T_0}^{T_0 + t^{ss}} \beta(\mathbf{x}, t) dt}{t^{ss}} \tag{4.8}$$

in which $\overline{\beta(\mathbf{x})}$ is the averaged brine flow property (e.g. brine flow velocity $\mathbf{V}$, fluid pressure p, and mineral mass fraction Φ), and $\beta(\mathbf{x}, t)$ is the dynamic brine flow property.

The dissolution front is updated using a time step size of τ. The distance travelled by a point on the dissolution front, ΔH, is approximated as,

$$\Delta H = \int_{T_0}^{T_0 + \tau} v_{\mathrm{d}} dt \approx v_{\mathrm{d}}' \tau \tag{4.9}$$

in which the second equality is based on the assumption that the time-averaged brine velocity is constant.

68

Based on the above assumptions, the proposed model reduces the computational costs for the dissolved cavity evolution calculation, making it different from previous models (COMSOL^{TM}[12] and DIM[**?**]).

4.3 Algorithm

In this section, the main algorithm that couples all the aspects of the dissolution process model is introduced. The sub-algorithms used to simulate the brine flow and dissolved mineral transfer in the cavity, and the algorithm applied to develop initial condition User Defined Function (UDF) for fluid dynamic simulation are presented. In addition, the novel algorithms employed to calculate dissolution front evolution and dissolution rate smoothing on the cavity boundary are discussed.

4.3.1 Main coupling algorithm

The main algorithm consists of four primary modules coupled in an iterative scheme, as shown in Figure 4.3. The four modules are: I) Geometry and mesh generation; II) Brine flow and dissolved mineral transportation simulation; III) Dissolution front evolution calculation; IV) Initial condition UDF generation. The information is exchanged between each module by using a developed program, and the iteration involving the four modules is conducted for each dissolution timestep, τ. The details of the four modules are given below.

I) The cavity geometry and corresponding mesh are generated using ANSYS ICEM^{TM} based on the current dissolution front location. An unstructured mesh of quadrilateral cells is developed to conform to the dissolution front shape. A relatively constant mesh element size is maintained with each update of the geometry.

II) The geometry and mesh information is then transferred to Module II, which simulates brine flow and the transport of dissolved minerals in a fixed cavity. The Finite Volume Method (FVM) software FLUENT^{TM} is used to solve the governing equations (4.1-4.4) which include the brine mass conservation equations, Navier–Stokes equations, and the mass transfer equation, to generate the time-histories distribution of brine flow velocity, pressure, and dissolved mineral throughout t^{ss}. Additional details are described in Section 4.3.2.

III) A newly developed code is used to calculate the dissolution front evolution. The dynamic brine flow simulation results (the brine flow properties and dissolved mineral mass fraction distribution output from Module II) are averaged over the period, t^{ss}, and the dissolution rate v'_d is computed at points along the dissolution front. The dissolution rate smoothing and the front movement algorithm are described in sections 4.3.3 and 4.3.4. The updated boundaries location is then obtained. The updated boundaries location information is written into a new ICEM^{TM} script for generating the new geometry and mesh for the next dissolution simulation time step until the dissolution simulation is completed. The FLUENT^{TM} script is also updated with the change in geometry.

IV) The brine flow and the dissolved minerals transport simulation in the updated geometry requires specification of the initial condition. The details about how the initial condition

is defined and how the UDF is generated are explained in Section 4.3.5.

4.3.2   Brine flow simulation algorithm

Simulations of brine flow and dissolved mineral transport are carried out in Module II. The flow chart of the algorithm is shown in Figure 4.4.

The geometry and mesh information is transferred from Module I and read by the brine flow simulation preprocessor. The initial condition for the first dissolution time step and the fluid dynamic simulation time step (Δt) are predefined. For the first dissolution time step, the initial condition in the cavity is defined as: (1) the brine flow is stationary, (2) the fluid pressure is equal to the atmospheric pressure (0.1 MPa), (3) the brine is saturated, and the dissolved mineral (rock salt) mass fraction is 0.264; for the subsequential dissolution time step, the UDF generated by Module IV is used to define the initial condition. The implicit transient SIMPLE algorithm is used to get the solution of the dynamic brine flow simulation. The dynamic brine flow simulation results are saved at every ten fluid dynamic simulation time steps. When the brine flow dynamic simulation time reaches the averaging period t^{ss}, the brine flow simulation in this cavity finishes.

As mentioned in Section 4.2.2, the dissolution process will reach a quasi-steady state after a certain period. The period is assumed to be equal to the averaging period t^{ss} in the proposed model. Kim *et al.* [63] found out that the time required to reach a quasi-steady-state condition depends on the Peclet number (Pe), dissolution channel length (L), and inlet velocity magnitude (v_0) as,

71
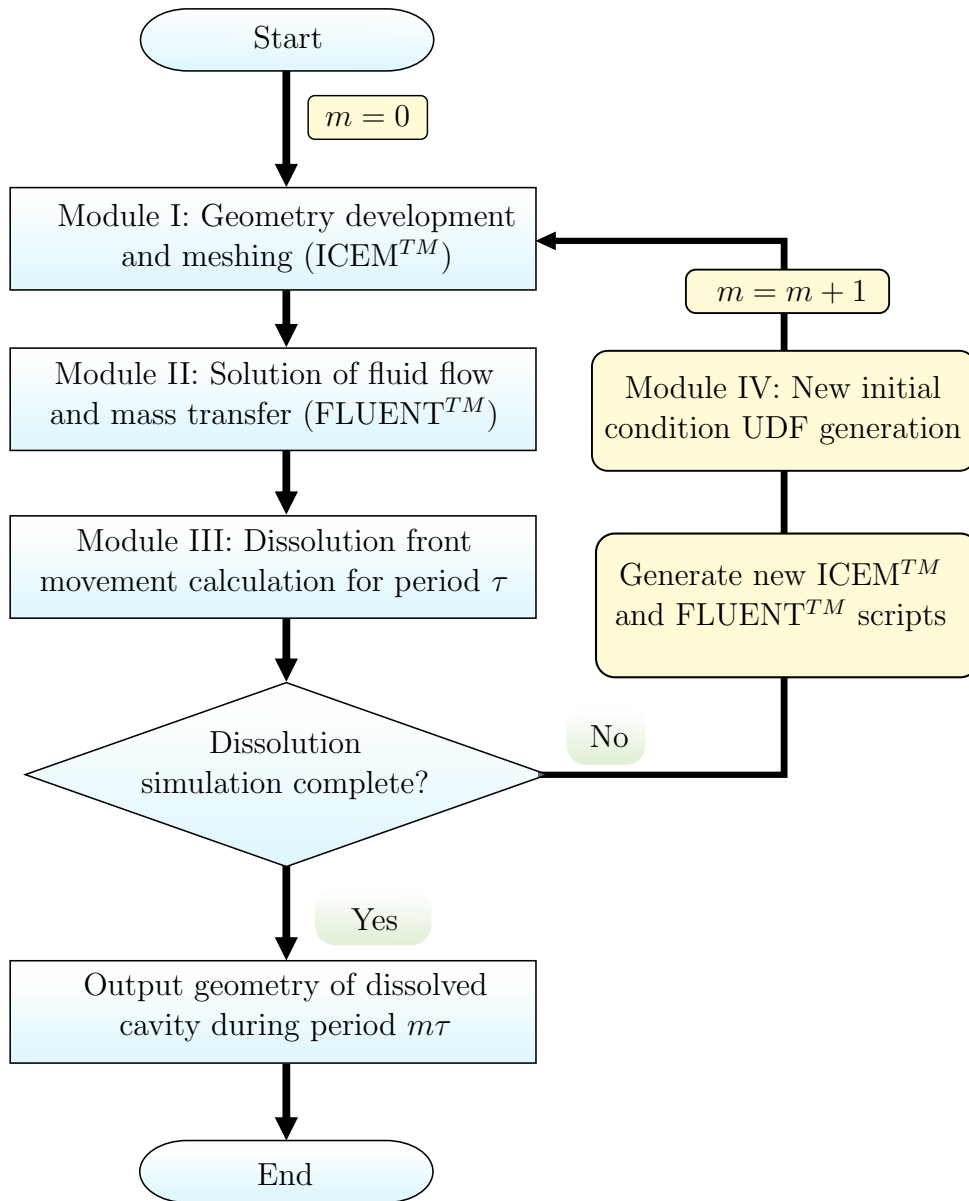
Figure 4.3: Sketch of main algorithm.
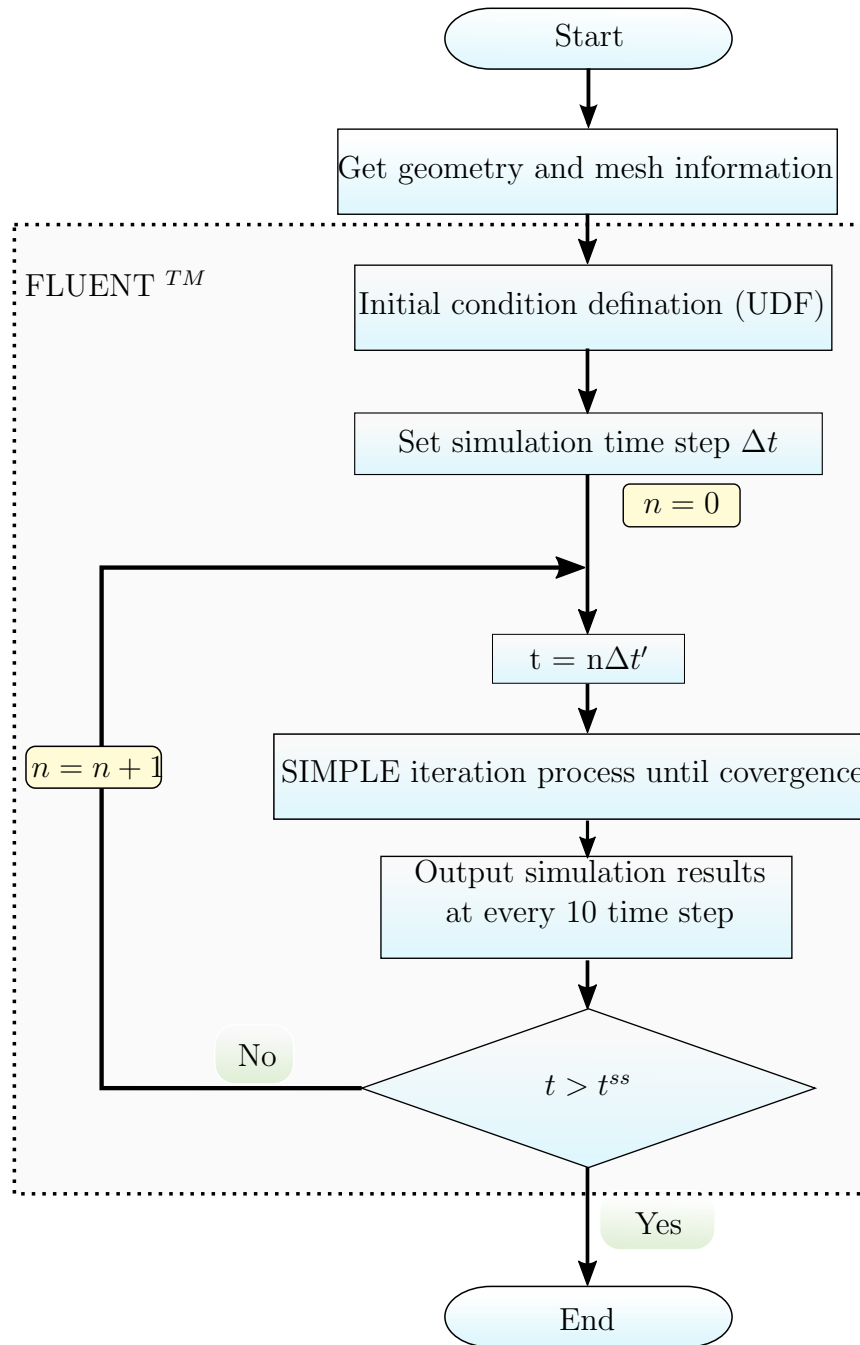
Figure 4.4: Brine flow simulation algorithm.

$$\begin{cases} t^{\text{ss}} \to 0 & Pe \ll 1, \\ t^{\text{ss}} \approx 2\frac{L}{v_0} & Pe \approx 1, \\ t^{\text{ss}} = \frac{L}{v_0} & Pe \gg 1. \end{cases} \qquad (4.10)$$

The averaging period is calculated using (4.10) for different inlet velocities. The distributions of the properties are written in history files during the period of t^{ss}, as shown in Figure 4.4.

4.3.3 Dissolution front evolution algorithm

The evolution of the dissolution front is calculated in the third module, and the flow chart is shown in Figure 4.5.

The time-averaged dissolved mineral mass fraction in the cavity is calculated using (4.8). The Green-Gauss cell-based method is used to obtain the mineral mass fraction gradient close to the dissolution front. Then, the dissolution rate (v'_d) is calculated using (4.7). The small eddies near the dissolution front cause the oscillations in the dissolved mineral mass fraction gradient, resulting in the dissolution rate fluctuation. However, the fluctuation is suppressed with a smoothing algorithm. The process of doing dissolution rate smoothing and the calculation of smoothed rate $\overline{v_d}$ are discussed in Section 4.3.4. The smoothing algorithm increases the algorithm's robustness and allows stable simulations on coarser meshes, which helps reduce the computational cost.

The front displacement in the normal direction is applied to the central point of the disso-
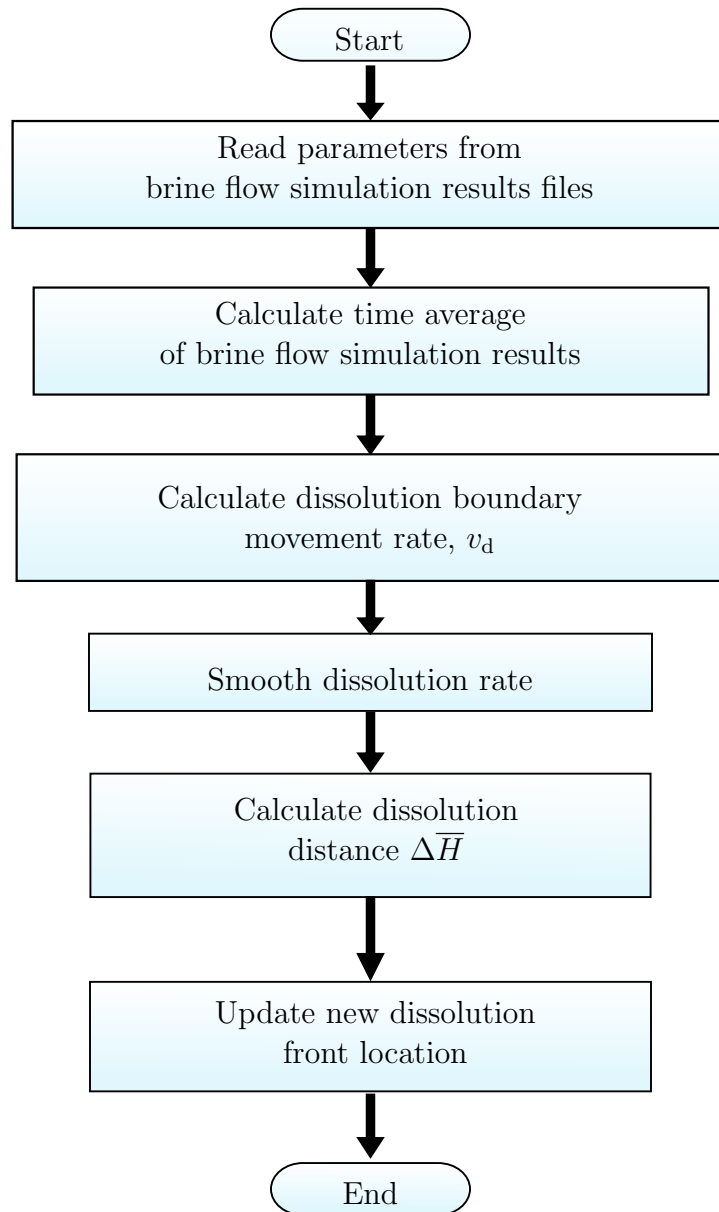
Figure 4.5: Dissolution front movement algorithm.

lution front boundary element. A spline function is used to connect the updated boundary element central points. The new dissolution front location information is then generated and written into the new ICEM^{TM} script, ready to be called to conduct the new geometry generation for next dissolution simulation.

4.3.4   Dissolution rate smoothing algorithm

The dissolved mineral mass fraction gradient can be highly irregular, especially near the dissolution front, because of the complex brine flow pattern and the irregular cavity shape. This leads to spurious oscillation of the dissolution rate along the front since the dissolution rate is related to the mineral mass fraction gradient. As shown in Figure 4.6, an algorithm is used for smoothing the dissolution rate and enhancing the robustness of the model.

The dissolution rate smoothing on a dissolution front cell is conducted using data from the neighboring boundary cells within the radius, r. The smoothing calculation goes through all the dissolution front cells and will iterate for s_n times. The parameters of r and s_n are predefined based on user experience. A sketch of the smoothing area identification and the weight distribution over the smoothing area is shown in Figure 4.7.

Let N be the number of boundary elements located in the averaging radius, and each element has the boundary edge length of d^{J}, $V_{\mathrm{d}}^{\mathrm{J}}$ the dissolution rate of each boundary element, w^{J} the weight applied on the element J, the averaged (smoothed) dissolution rate of the central dissolution front boundary element I, $\overline{v_{\mathrm{d}}^{\mathrm{I}}}$, is,

Start

$s_i = 0$

$I = 1$

Locate all cells within radius r of cell I (computed with cell centers)

$I = I+1$

$$\overline{v_d^I} = \frac{\sum_{J=1}^{N} w^J v_d^J d^J}{\sum_{J=1}^{N} w^J d^J}$$

$s_i = s_i + 1$

no

All boundary cells computed?

Update dissolution rate $v_d^I = \overline{v_d^I} \; \forall \, I$

yes

$s_i < s_n$?

yes

no

End
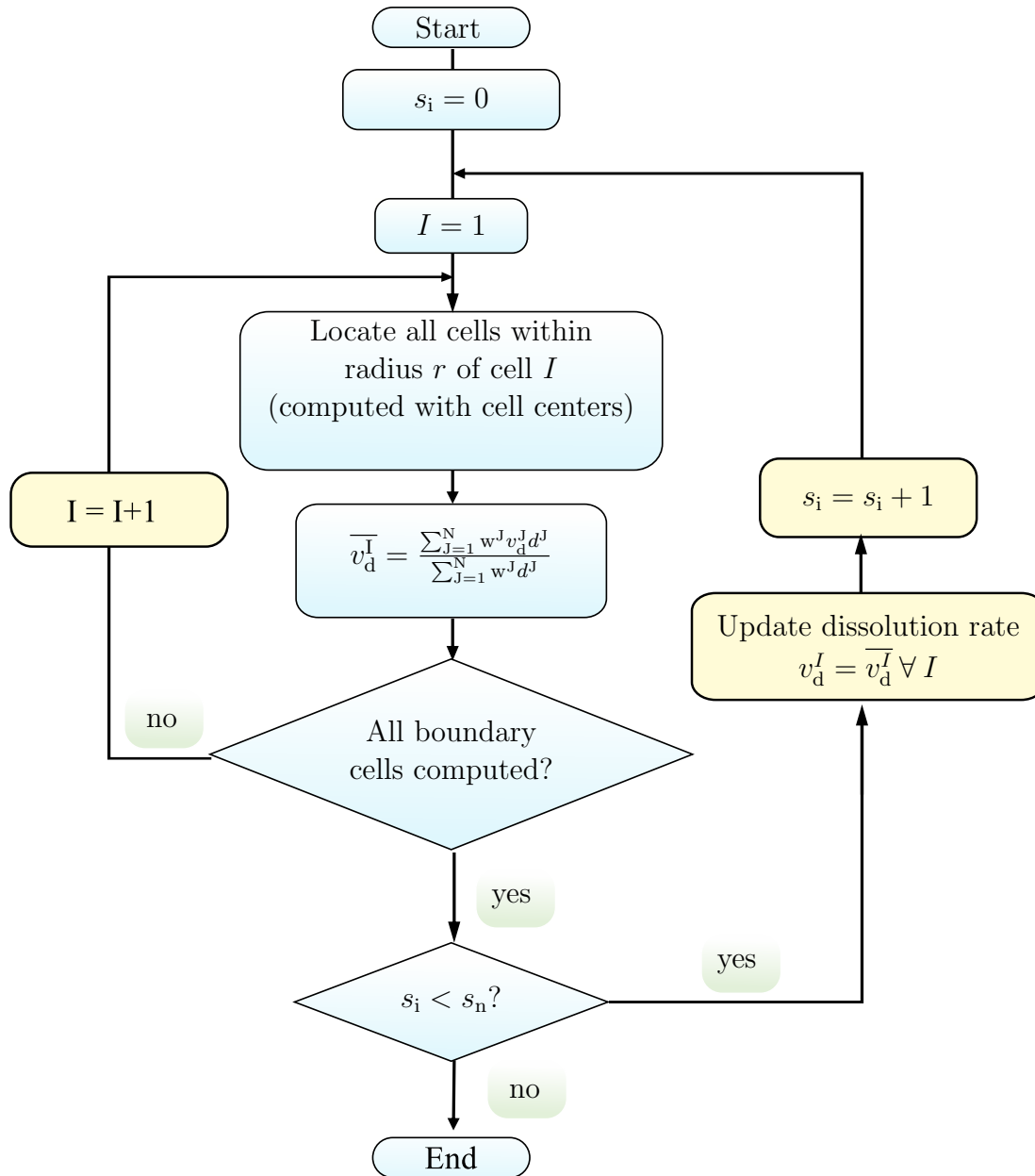
Figure 4.6: Boundary dissolution rate smoothing algorithm.
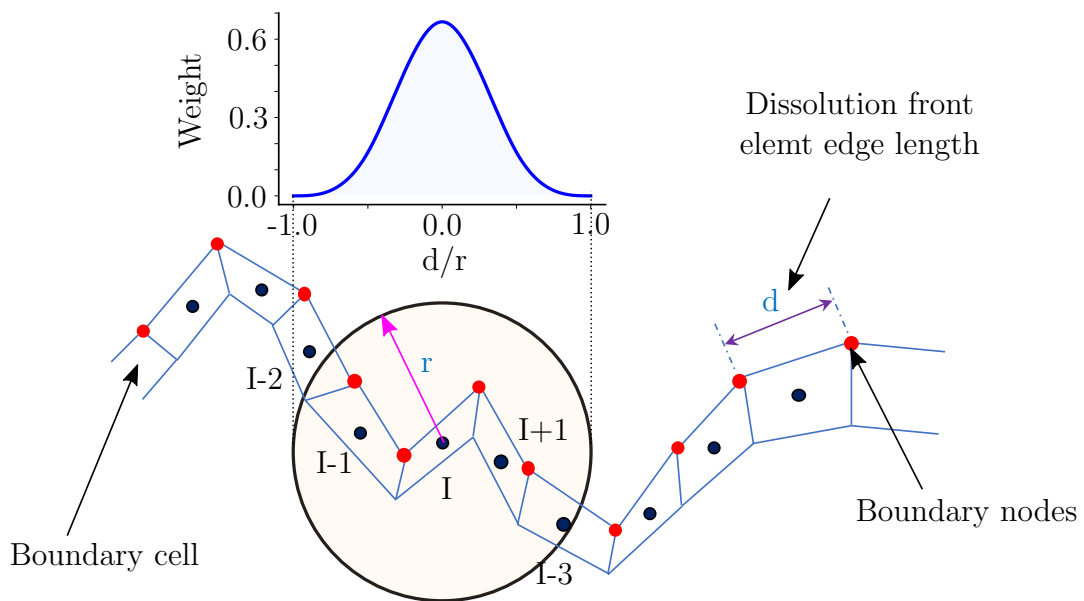
Figure 4.7: Illustration of dissolution rate smoothing area description and weight distribution.

$$\overline{v_{\mathrm{d}}^{\mathrm{I}}} = \frac{\sum_{\mathrm{J}=1}^{\mathrm{N}} \mathrm{w}^{\mathrm{J}} v_{\mathrm{d}}^{\mathrm{J}} d^{\mathrm{J}}}{\sum_{\mathrm{J}=1}^{\mathrm{N}} \mathrm{w}^{\mathrm{J}} d^{\mathrm{J}}} \tag{4.11}$$

The weight can be determined as,

$$w^{\mathrm{J}} = \begin{cases} \frac{2}{3} - 4(\frac{d}{r})^2 + 4(\frac{d}{r})^3 & \frac{d}{r} \leq \frac{1}{2}, \\ \frac{4}{3} - 4(\frac{d}{r}) + 4(\frac{d}{r})^2 - \frac{4}{3}(\frac{d}{r})^3 & \frac{1}{2} \leq \frac{d}{r} \leq 1, \\ 0 & \frac{d}{r} \geq 1. \end{cases} \tag{4.12}$$

The dissolution rate of each element is updated (smoothed) by replacing each v_d^{I} with $\overline{v_{\mathrm{d}}^{\mathrm{I}}}$, and the whole smoothing calculation process repeats until the iteration number s_n is achieved.

A comparison of the dissolution rate profile before and after using the smoothing algorithms is shown in Figure 4.8. It demonstrates that the original dissolution rate on the dissolution front is highly irregular, as expected. The smoothing algorithm can effectively eliminate spurious oscillations while ensuring the overall dissolution rate distribution trend. The smoothing calculation with a weight function (4.12) is superior in representing the dissolution rate distribution in the area with significant dissolution rate changes.

4.3.5 Initial UDF generation

In order to get the precise initial condition for brine flow simulation in a new cavity, the least-squares method is employed to get the best fit of the properties distribution obtained from (4.8) based on the dissolution simulation results, and the 2nd-degree polynomial equations of the properties spatial distribution are obtained and written into the
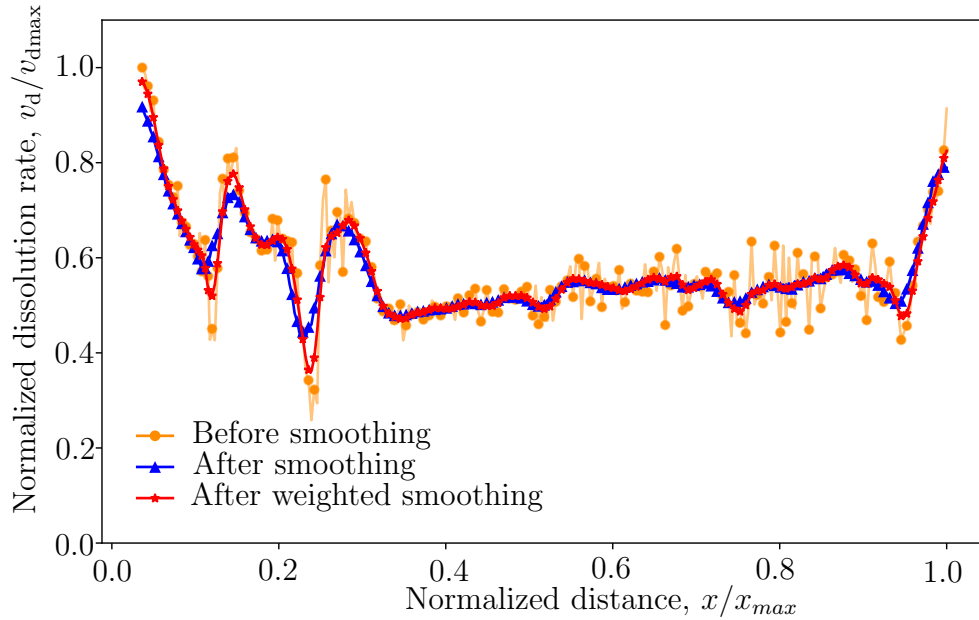
Figure 4.8: Dissolution rate distribution profile with and without smoothing treatment.

UDF file. The UDF file is then read into the brine flow simulator and helps define the initial conditions. An example of the averaged brine mass fraction distribution and the fitted surface is demonstrated in Figure 4.9. The fitting equation of $\overline{\Phi}$ will be used to define the initial mass fraction distribution for the brine flow simulation in the new geometry.

4.4 Discussion

4.4.1 Model verification

The convergence of the proposed model is verified in this section. Simulations are conducted to test the self-consistency of the algorithm. The geometry and boundary conditions are

a)

$$\overline{\Phi} = 0.204 + 0.370X - 13.45Y + 0.759X^2 + 32.30XY + 607.8Y^2$$

b)
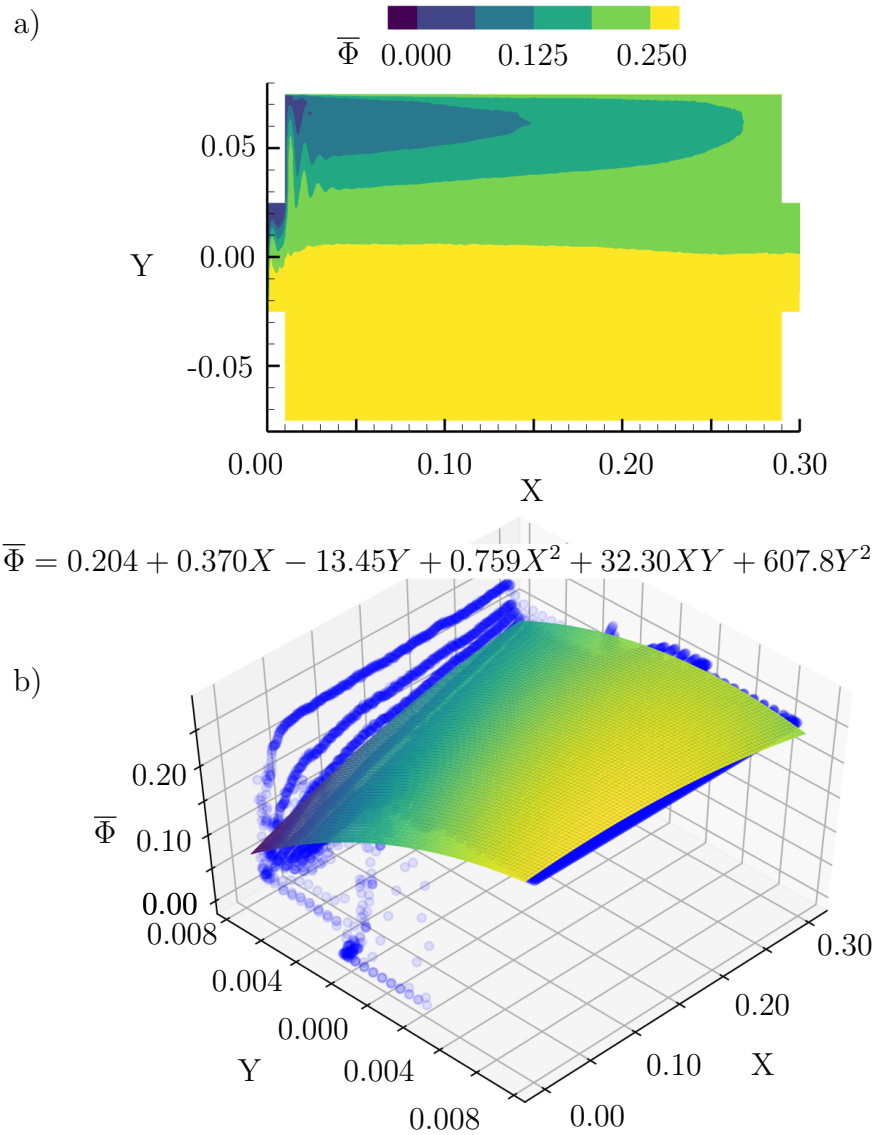
Figure 4.9: Initial distribution fitting. a) Time-averaged mass fraction Φ distribution. b) Least-square fitting surface of the time-averaged mass fraction distribution, the fitting polynomial equation will be used to define the initial condition for the next dissolution time step simulation.

shown in Figure 4.10, with $2w = 0.015$ m and $l = 0.3$ m. The domain is assumed to be filled with brine. As shown in Figure 4.10, fresh water enters the cavity through the inlet. Fluid flow is assumed to be well-developed such that the inlet velocity has a parabolic profile. The parabolic profile assumption can help reduce the sharp change of fluid flow velocity near the inlet corner and improve the model stability. The brine is discharged from the outlet. Dissolution occurs at the interface (dissolution front) between brine and solid mineral. The velocity of the brine is assumed to be zero since the dissolution rate of the interface is much lower than the brine flow velocity. The bottom boundary is the stationary wall where the solid mineral is absent.

Dissolution front
$\mathbf{V} = \mathbf{0}$ m/s
$\phi = 0.264$

Fresh water inlet
$U_{max} = 0.01$ m/s $\quad w$ $\quad U_{max}$
$\phi = 0$

Brine outlet
$p = 0.1$ MPa
$\nabla\Phi = \mathbf{0}$

l

Bottom wall
$\mathbf{V} = \mathbf{0}$ m/s
$\nabla \cdot (-\rho D_{\mathrm{s}} \nabla\Phi) = 0$ kg/s
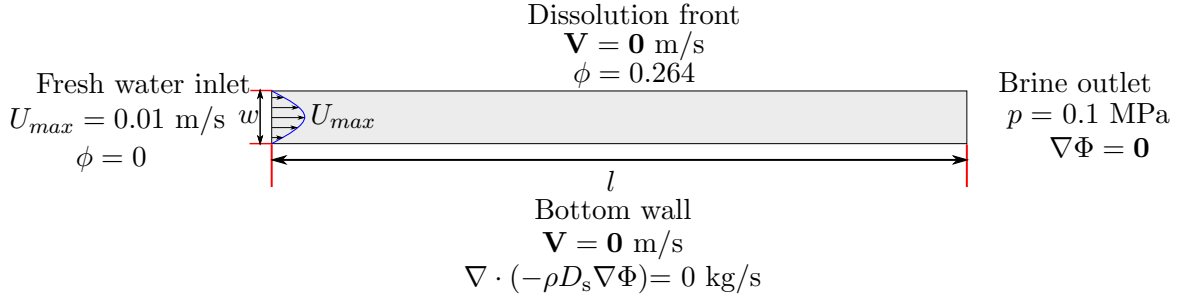
Figure 4.10: Initial cavity geometry for convergence study.

The parameters used for the convergence study are listed in Table 4.1.

Table 4.1: Material properties for convergence study

Parameter	Variable	Value	Unit
Dynamic viscosity	μ	10^{-3}	Pa/s
Density of solid mineral	ρ_{s}	2170	kg/m^3
Density of water	ρ_{w}	1000	kg/m^3
Diffusion coefficient in brine	D_{s}	10^{-9}	m^2/s
Diffusion coefficient near dissolution front	D_{f}	10^{-9}	m^2/s

The results obtained from a model with element size $s_0 = 2 \times 10^{-8}$ m^2 and time step size $\tau = 500$ s are employed as the reference for convergence analysis.

To verify the convergence trend, a normalized L$_2$ norm is used,

$$R_{\Delta\overline{H}l2} = \left(\frac{\int\limits_{\Gamma_d} \left(\Delta\overline{H}_{\mathrm{rs}} - \Delta\overline{H} \right)^2 d\Gamma}{\int\limits_{\Gamma_d} \Delta\overline{H}_{\mathrm{rs}}^2 d\Gamma} \right)^{1/2} \tag{4.13}$$

where $\Delta\overline{H}_{\mathrm{rs}}$ denotes the displacement of the dissolution front in the reference model [m] and $\Delta\overline{H}$ is the dissolution front displacement of other models [m].

The L2 norm changes with mesh and times step size are shown in Figure 4.11. The analysis results show that when the mesh size and dissolution simulation time step get close to the reference model, the dissolution front approaches the reference model, and the error becomes small. Hence, it can be concluded that the model is self-consistent.

4.4.2 Validations: lab experiment and simulation

The lab experiment device and the specimen used for the model validation are described in this section, and the corresponding dissolution simulations are introduced.
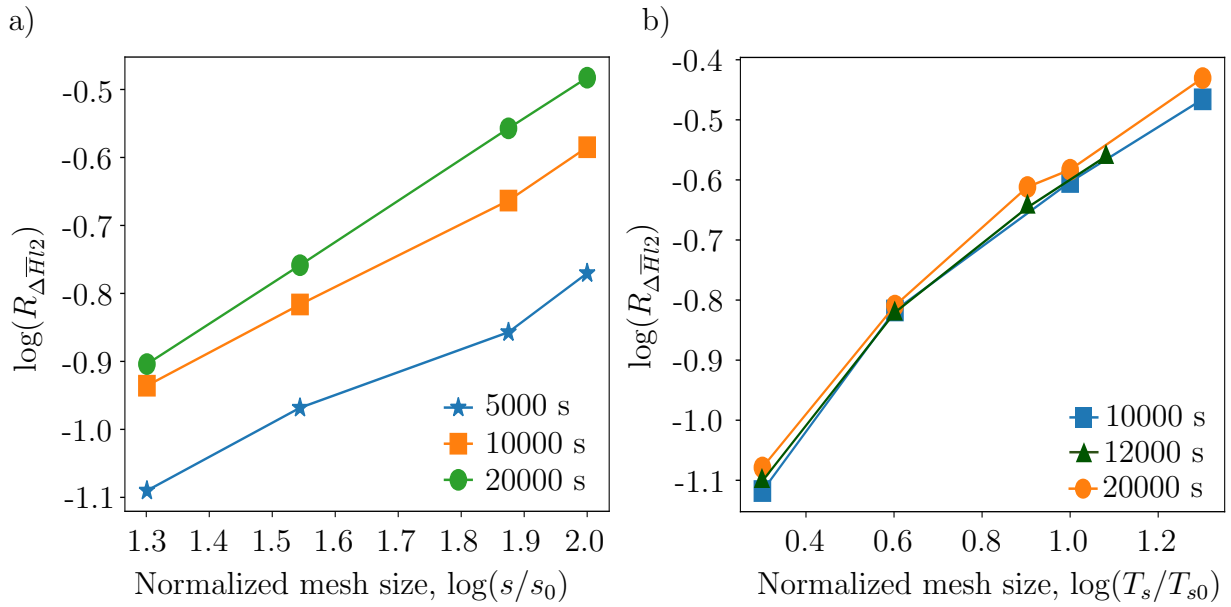
Figure 4.11: The L2 difference norm for mesh (a) and temporal refinement (b).
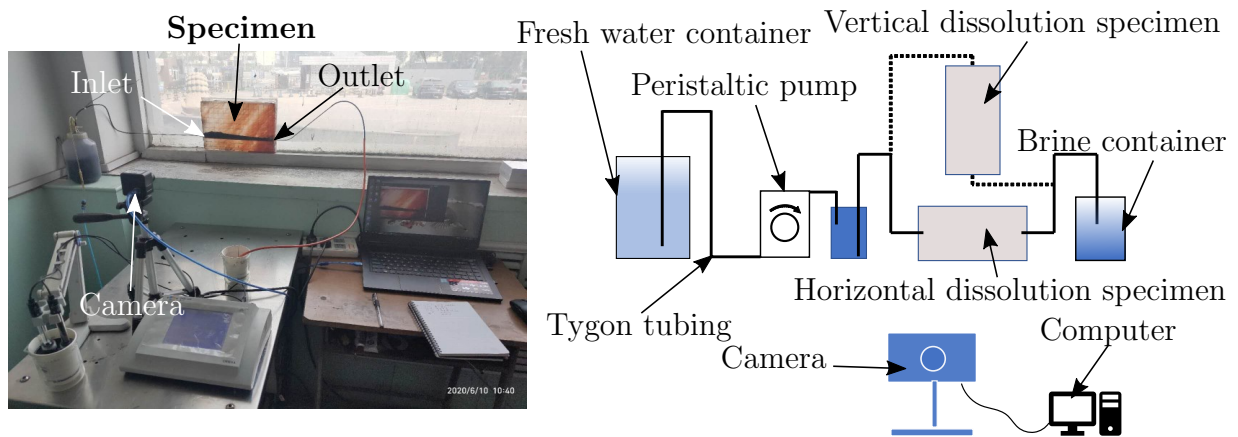
Figure 4.12: Picture and sketch of the lab device.

Lab experiment and specimen

The experiment lab device is shown in Figure 4.12. It is used to investigate the dissolution of salt rock samples through channels in different orientations. In the experiment, each salt rock plate (over 99% soluble content), with dimensions 0.30 m × 0.20 m × 0.03 m, was machined with a 5×10^{-3} m diameter hole in the middle. The hole went through the specimen and acted as the initial brine transportation channel. The length of the hole was 0.3 m. Metal tubes with a diameter of 5×10^{-3} m were inserted into the hole from both ends of the initial channel. The surface and boundaries of the salt rock plate were sealed with glue and glass to prevent brine leaking during experiments. The samples were fixed in the horizontal or vertical direction (based on the pre-drilled hole orientations) to conduct different dissolution experiments. For the vertical dissolution, the fresh water was slowly pumped with a set velocity of 0.001 m/s into the hole for the first two hours and then switched to 0.01 m/s to conduct the remaining dissolution experiment. The fresh water injection velocity for the horizontal dissolution scenario was kept at 0.01 m/s through the whole dissolution process. A constant fluid pressure was kept at the other end of the hole. A camera was placed in front of the specimen to monitor the change of the dissolved cavity.

Simulation model geometry and perimeters

The 2D initial geometries for the vertical and horizontal dissolution simulation are illustrated in Figure 4.13. The width of the geometry is 5×10^{-3} m, with the dissolution front set as 0.3 m. The values are the same as the diameter and length of the dissolution channel in the lab experiments. Under the vertical dissolution scenario, the magnitude of the inlet fresh water velocity, U_{max}, was 0.001 m/s for the first two hours and 0.01 m/s for the rest of the dissolution period. U_{max} was set to 0.01 m/s for the entire period of the horizontal

85
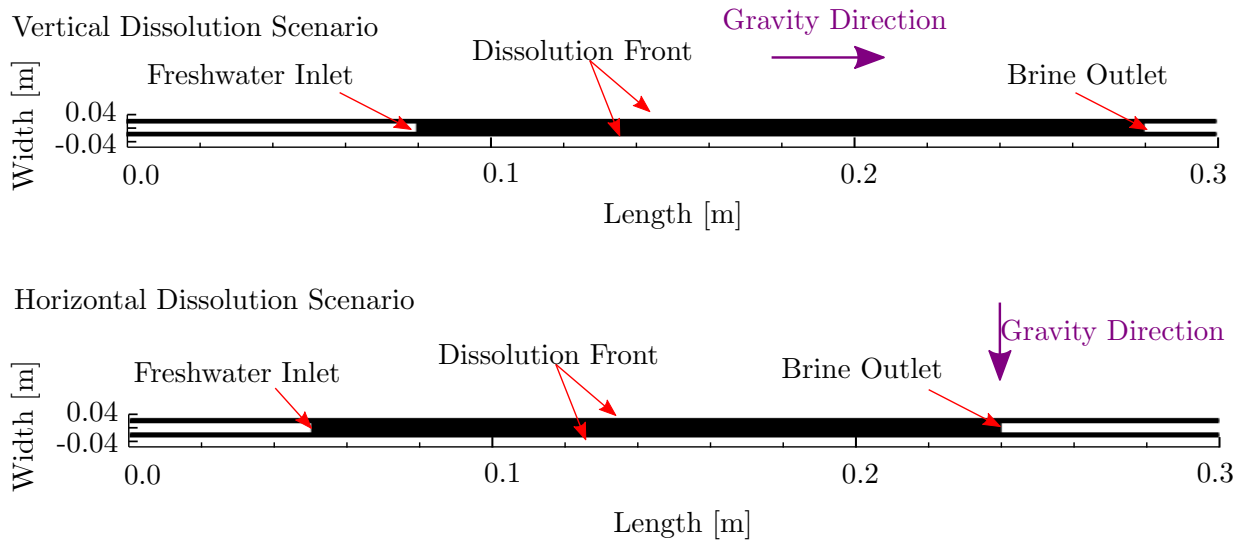
Figure 4.13: Initial cavern geometry for vertical and horizontal dissolution.

dissolution simulation. The diffusion coefficient near the dissolution front is selected to obtain the best agreement with the experimental results. The parameters in the model are given in Table 4.2.

Unstructured meshes with quadrilateral cells were employed, and the average mesh size was set to be approximately 5×10^{-8} m^2. The number of the mesh cells in the initial geometry was 3.3×10^4 and increased with the expansion of the dissolved cavity. The Peclet number is calculated as $Pe = h_m U_{max}/D_s$, in which h_m is the characteristic length. The Peclet number reached 1.2×10^6 and was much larger than the previous studies on dissolution simulation[64, 71, 72]. The last equation of (4.10) was used to obtain the averaging period t^{ss}. When the inlet velocity was 0.001m/s and 0.01m/s, t^{ss} was 300 s and 30 s, respectively.

Table 4.2: Material Properties for comparison simulation

Parameter	Variable	Value	Unit
Inlet velocity	U_{max}	0.001 or 0.01	m/s
Dynamic viscosity	μ	10^{-3}	Pa/s
Density of salt rock	ρ_s	2165	kg/m^3
Density of water	ρ_w	1000	kg/m^3
Diffusion coefficient in brine	D_s	10^{-9}	m^2/s
Diffusion coefficient near dissolution front	D_f	$(1.25 - 3.0) \times 10^{-9}$	m^2/s

Lab and simulation results comparison

Figure 4.14 shows the dissolved cavity shapes under vertical dissolution after 1 h, 3 h, and 5 h. The shapes of the simulated cavities show good agreement with the experimental results, indicating that the proposed model can reflect the dissolution process. Under the vertical dissolution scenario, the volume of the dissolved cavity grows due to the injection of fresh water. The boundaries of the dissolved cavities expand outwards and upwards with time. During the dissolution process, the dissolved cavity formed the well-known "morning glory" shape. The upward movement of the dissolution experiment is affected by thin air film that exists on the top of the cavity, limiting vertical growth and leading to a very flat aspect. The proposed model is adjusted to simulate the air effect by modifying the dissolution diffusion coefficient on the top dissolution boundary, using trial and error to obtain similar behavior. In the proposed model in this work, the D_f is set to be 1.25^{-9} m^2/s at the vertical-cavity top dissolution front when considering the air film effects, and the value is 2.5^{-9} m^2/s on the rest of the front. The expansion of the cavity is not perfectly symmetric, and the reasons for this phenomenon will be explained in Section 4.4.3.

The evolution of dissolution fronts has a significant difference in the horizontal dissolution
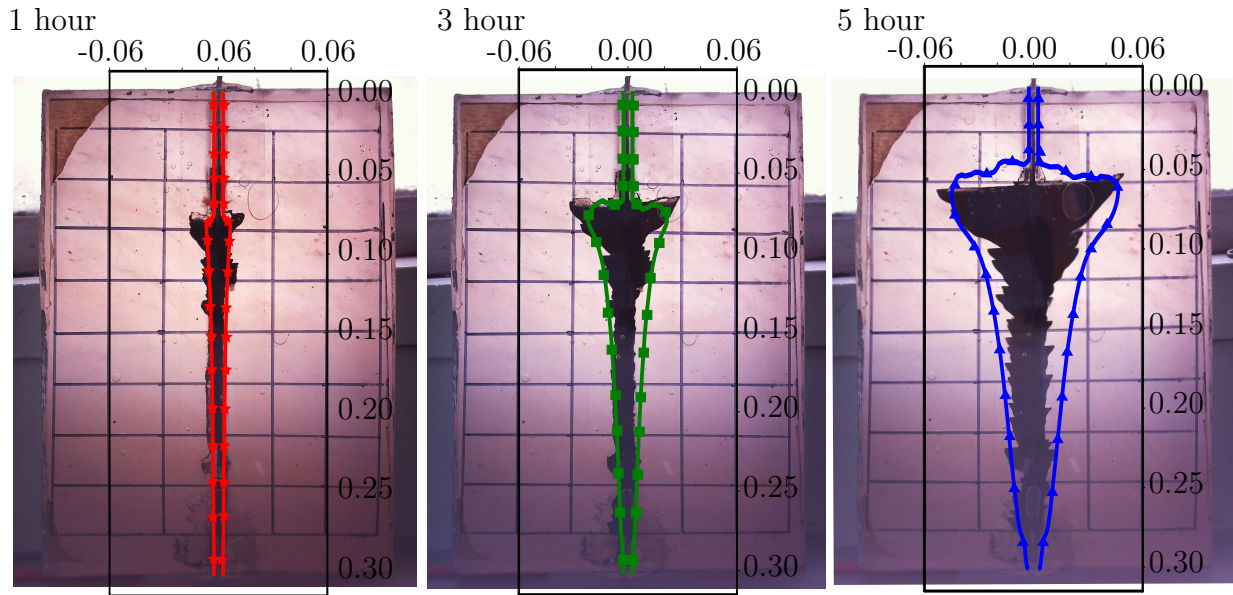
Figure 4.14: Comparison between simulation and lab results after 1h, 3h, and 5h dissolution under vertical dissolution.

scenario compared to the vertical scenario, as shown in Figure 4.15. The D_f is set to be 3.0^{-9} m^2/s on both upper and lower dissolution fronts. After a long dissolution time, the lower dissolution front does not show apparent changes, but the shape of the upper front changes significantly. The proposed numerical model captures the difference between the upper and lower dissolution surfaces and gives a high degree of agreement with the shape of the cavity.

Although the proposed model results give a good agreement with the experimental results, some small irregular shapes in the lab experiment are not shown in the simulation, especially for the vertical dissolution. At this time, we are unable to fully explain the discrepancy between the dissolution front shape of simulation and experiment results. There are some possible reasons listed here:
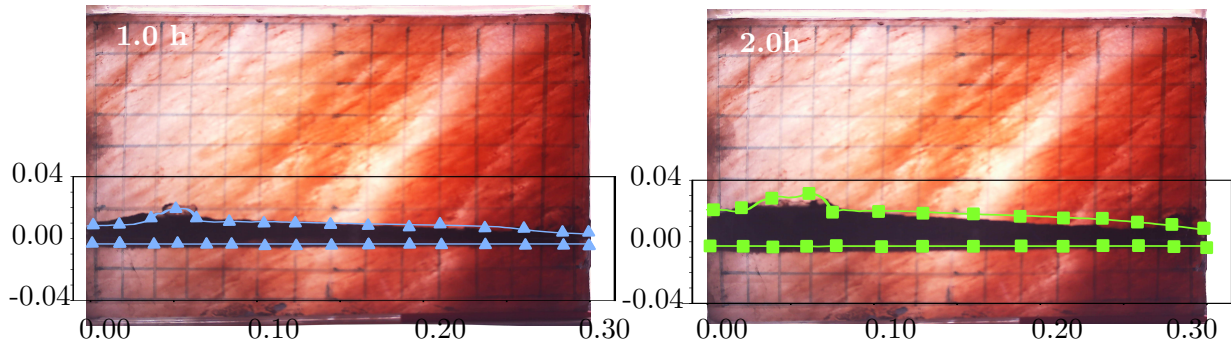
Figure 4.15: Comparison between simulation and lab results after 1h, and 2h dissolution under horizontal dissolution.

1. The dissolution properties are heterogeneous in some areas of the specimen because of crystalline orientations or imperfections, as shown in Figures 4.14 and 4.15, but it is not modeled in the simulation.

2. The development of eddies in the cavity can influence the dissolution pattern. In our model, the brine flow is assumed to be 2D, and we tried to make the experiment "two-dimensional", but eddy generation at this scale is still a three-dimensional phenomenon. This will leads simulations to be slightly different from the lab experiments.

3. It is possible that some damage happened to the specimens during the sample preparation. Micro-fractures or cracks developed in the solid mineral can significantly impact the dissolution pattern and change the dissolution direction[73]. The impact of any small damage along crystal boundaries on the dissolution is ignored in our proposed model.

4. A local re-crystallization process may happen in the cavity where the crystallization rate of salt rock is higher than the dissolution rate; then, salt precipitation could form the zigzag shape. In our model, only the dissolution process is considered; any crystallization process that might occur is not captured.

89
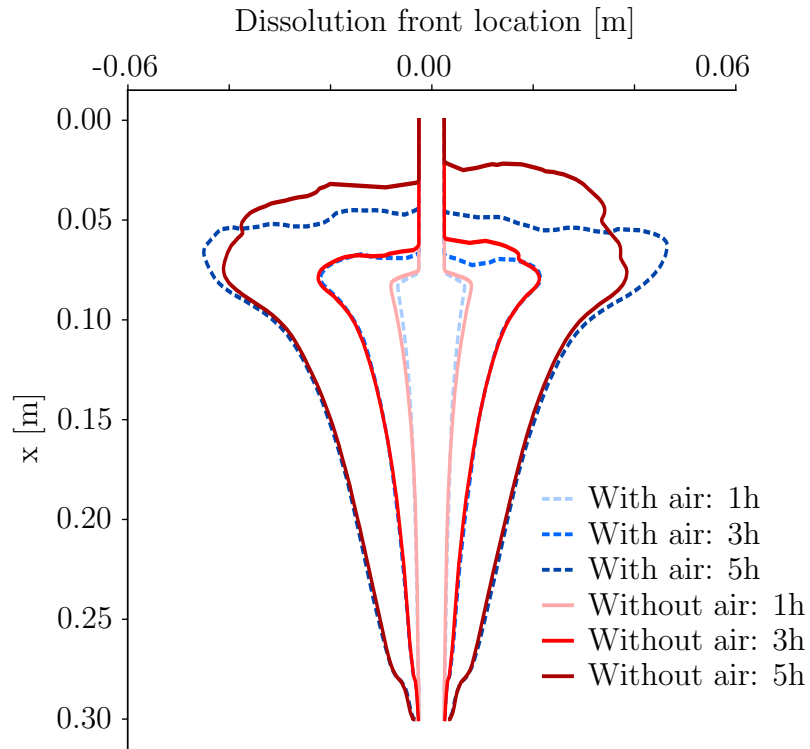
Figure 4.16: Dissolution front comparison with and without air in the cavity top

4.4.3 Mechanics of dissolution

The proposed model presents excellent accuracy and reliability in simulating the coupled dissolution process in a 2D situation. In this section, the simulation results will be further discussed, and the mechanism behind the coupled dissolution process will be studied.

Vertical dissolution

The dissolution front evolution of the vertical cavity is shown in Figure 4.16. The two dissolution scenarios in which air exists and does not exist at the top are presented. It shows that the cavity expands with time, and the dissolution front displacement decreases

90

from top to bottom in both scenarios. The dissolution front near the inlet undergoes large displacement. The air restricts the vertical movement of the upper dissolution front but results in a significant outward dissolution (the "morning glory" effect).

We note that roof shape is always an issue in real cavity design for storage use, and a wide flat roof is never the goal[22]; instead, a progressively narrowing roof section is best to avoid undesirable roof instability. The simulation results indicate that while methods, such as the air pad, are useful to control the longitudinal growth of the cavity, the lateral development of the cavity requires more attention.

The vertical dissolution simulation models the evolution of the cavity under changing freshwater inlet velocities. In the first two hours, the inlet velocity is 0.001 m/s, and after that, the velocity increases to 0.01 m/s. The dissolved mineral distribution and brine flow patterns under these two inlet fresh water injection velocities without air are shown in Figures 4.17 and 4.18. During the early stage, the inlet velocity is low, and the injected freshwater moves upwards along the borehole wall due to its low density. After contacting the salt rock, the brine concentration rises rapidly, and then the denser brine moves downwards due to gravity (i.e., buoyancy). Vortexes develop and further promote the circulation of the solution. However, because the freshwater injection rate is small, the solution becomes saturated shortly after it enters the cavity and contacts the salt rock wall. It will no longer affect the salt rock dissolution of other areas. Therefore, as shown in Figure 4.17, the low-concentration solution with a complex flow pattern is trapped in the upper zone of the cavity. The distribution of the brine concentration undergoes obvious changes during the dissolution process. After injecting fresh water for 5 hours (Figure 4.18), the low concentration brine occupies the majority area of the cavity. Still, the trend that dissolved mineral
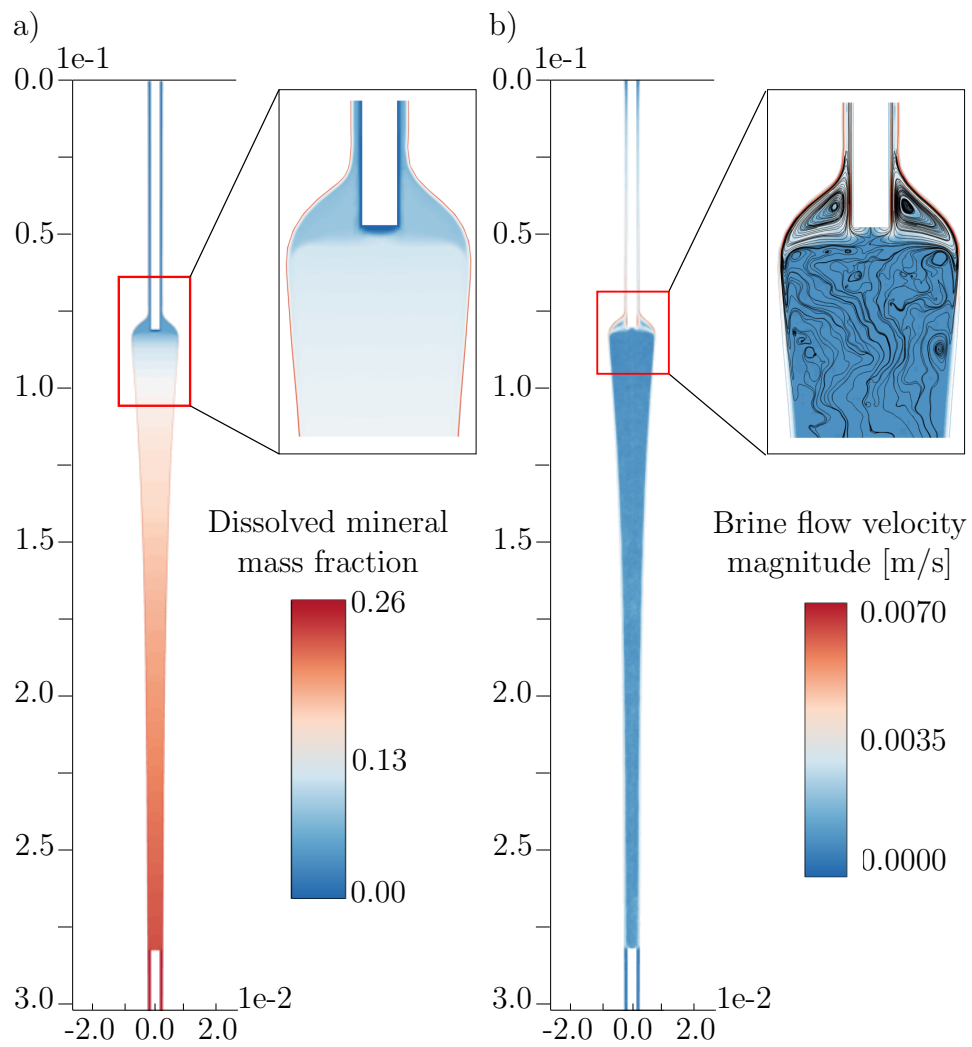
Figure 4.17: Mass fraction and velocity distribution for vertical dissolution at 1 h
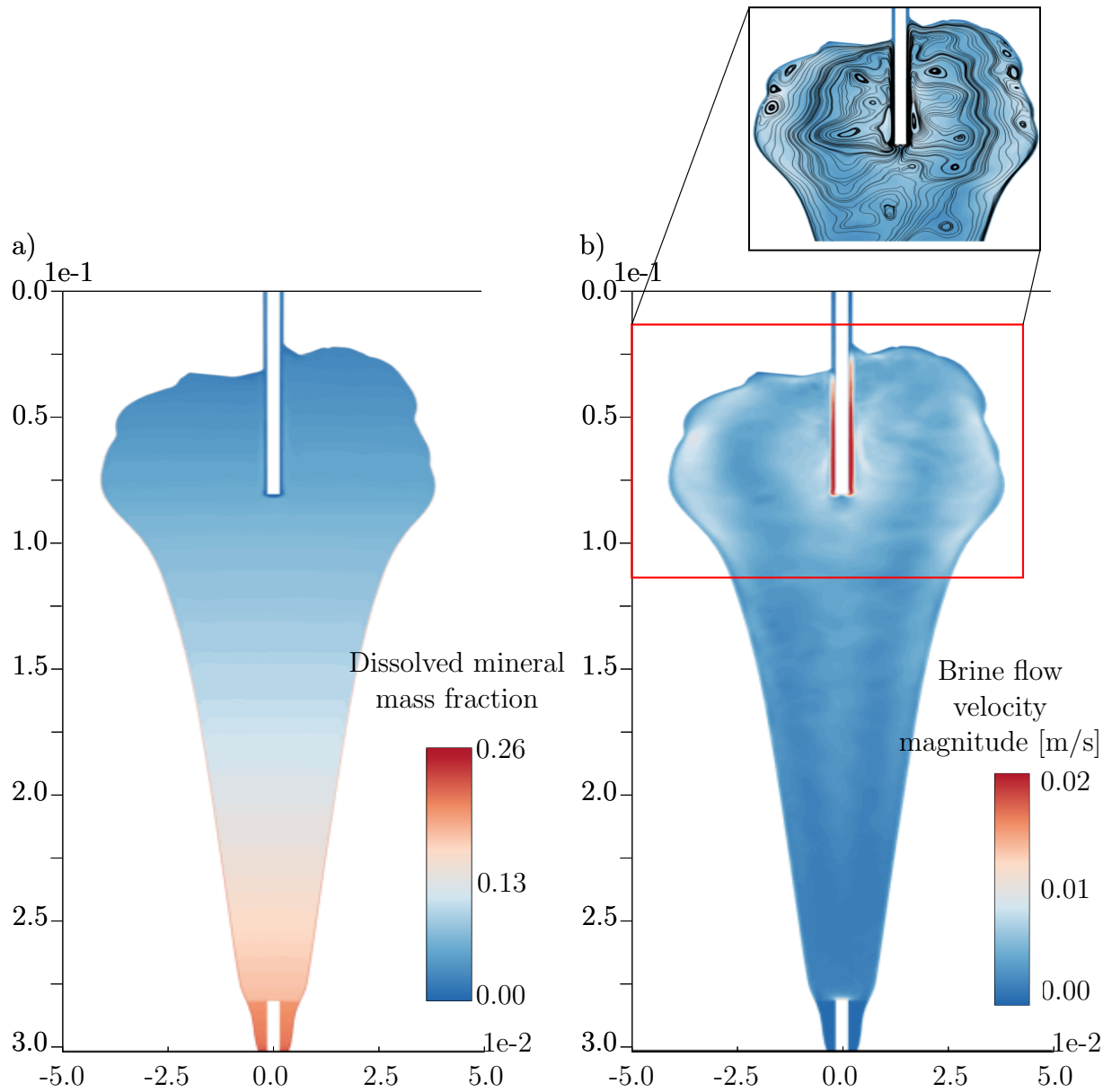
Figure 4.18: Mass fraction and velocity distribution for vertical dissolution at 5 h

mass fraction increases from inlet to outlet remains unchanged, and the mass fraction of the brine approaches saturation near the outlet. Gravity has an impact on the flow of the injected fresh water even as the mass fraction of the brine in the cavity drops, and the inlet velocity increases from 0.001 m/s to 0.01 m/s.

The enlargement of the cavity and the increased fresh water injection velocity promote more complex brine flow patterns in the cavity. Large eddies develop in the cavity, with some small vortexes growing near the dissolution front, which affects the dissolution pattern near the boundaries. The generation of different scales of eddies is rarely noted in other studies related to mineral dissolution. In addition, the results show that the distribution of brine concentration experiences significant changes during the dissolution process, and the distribution of the brine concentration can not be simplified as a linear function as in previous studies[74].

To further investigate the coupling effects of the brine flow and dissolution pattern and why the dissolution is not perfectly symmetric, a snapshot of the mass fraction and velocity distribution and dissolution rate distribution for vertical dissolution at 2.5 h is shown in Figure 4.19. The mineral mass fraction of the brine on the top is small (Figure 4.19(a)), indicating that the dissolved mineral mass fraction gradient is large near the fronts, promoting more rapid dissolution of the mineral. The dissolution rate at the cavity top is higher than other areas and decreases from inlet to outlet (Figure 4.19(c)). However, the dissolution rates at the same height level on either side of the 2D model do not equal each other, especially in the region between 0.06 m and 0.10 m. The dissolution rate of the RHS front is slightly higher than on the LHS. That is why the changes of the RHS and LHS front are similar but not symmetric with the central cavity line. The difference in
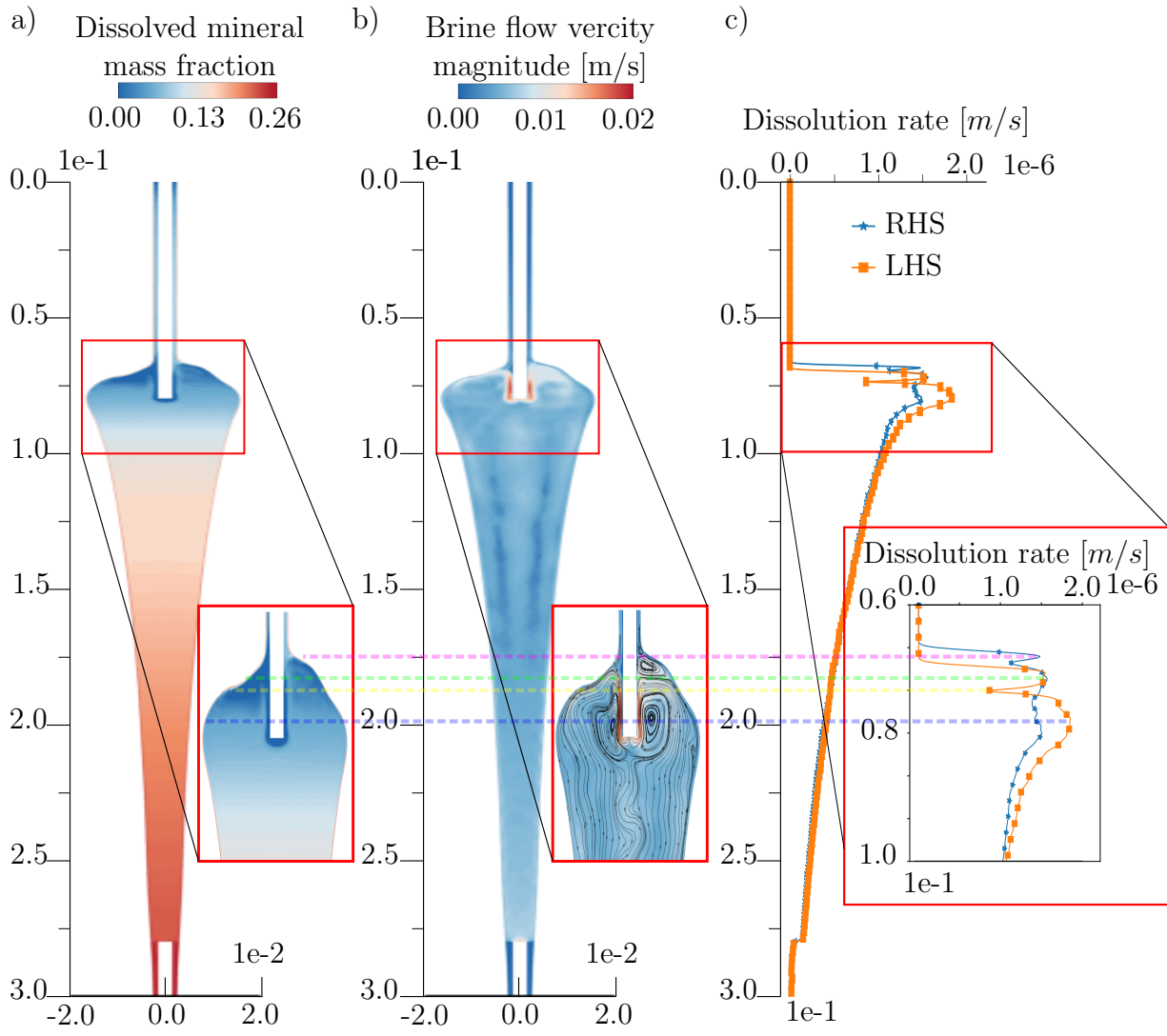
Figure 4.19: Mass fraction and velocity distribution and dissolution rate distribution for vertical dissolution at 2.5 h

the brine flow pattern and eddy development at the two sides of the inlet, as shown in Figure 4.19(b), contributes to the uneven distribution of brine concentration, which then affects the dissolution pattern. The brine flow velocity near the RHS front is larger than the LHS, resulting in a greater drop in mineral mass fraction near the dissolution front because of brine advection and eddies effects. It leads to a rise in the mass fraction gradient at the LHS front, which is not noticeable along the dissolution front shown in Figure 4.19; but can be recognized from the general mass fraction distribution trend. While a highly symmetric shape is often sought, deviations from symmetry are to be expected. Due to the presence of turbulence and eddies and the path-dependent irreversible nature of dissolution, a symmetric solution is not achieved, as small numerical deviations lead to non-symmetric solutions.

When the low-density brine rises and touches the top boundary and dissolves the solid mineral, the denser brine transports downward due to gravity, promoting the vortex generation. The vortexes near the dissolution front contribute to the convection of the brine. More dissolved mineral is taken away, so the dissolution rate increases, as shown in the area highlighted with purple and green dash lines in Figure 4.19. When the dissolution front is flat, the brine flow along the front, which similar to the horizontal dissolution, and the brine mass fraction will increase near the downstream front. This results in a decrease in the dissolution rate, as indicated by the yellow dash line. The unsaturated brine then moves downward along the cavity boundary. At the lower part of the front (such as the area marked with the blue dash line), the brine velocity direction is consistent with gravity force direction. The dissolved salt rock can be quickly taken away, which promotes dissolution. That is why the largest dissolution rate is not located on the top of the cavity. The uneven brine flow pattern and gravity effect significantly impact the dissolution pattern,

96

but these effects have been rarely highlighted in previous work.

In addition, the geometry of the cavity affects the flow pattern. The low-density brine moves upward along the tubing and is forced to change the direction when it reaches the top boundary. Then the brine flows along the cavity boundary, and eddies develop. Once deviations from the symmetry cavity exist, the vortex development on both sides of the cavity will change, leading to variations in distribution rates along the front, which is also shown in Chapter 3.

The complex coupling phenomena between the brine flow (with buoyancy effects), eddy development, and dissolution front evolution are seldom addressed in previous models but can be captured by the model presented herein.

Horizontal dissolution

Figure 4.20 shows the dissolution distance and rate evolution of the upper and lower dissolution fronts of the horizontal cavity. The cavity widens as fresh water is injected. Dissolution along the bottom front is negligible, while dissolution at the upper surface varies considerably along the brine flow path. The dissolution mainly happens near the inlet, and the widening effect drops along the brine flow path. Even though the dissolution rate has been smoothed in our model, irregular shapes and edges are still generated. The upper dissolution front propagates upwards with time, and the dissolution also extends to the area behind the inlet pipe. Figure 4.20(b) illustrates the dissolution rate distribution. The value of simulation results falls in the range of the mineral dissolution rate obtained from the lab experiments[68], indicating that the proposed model may be able to reliably

97
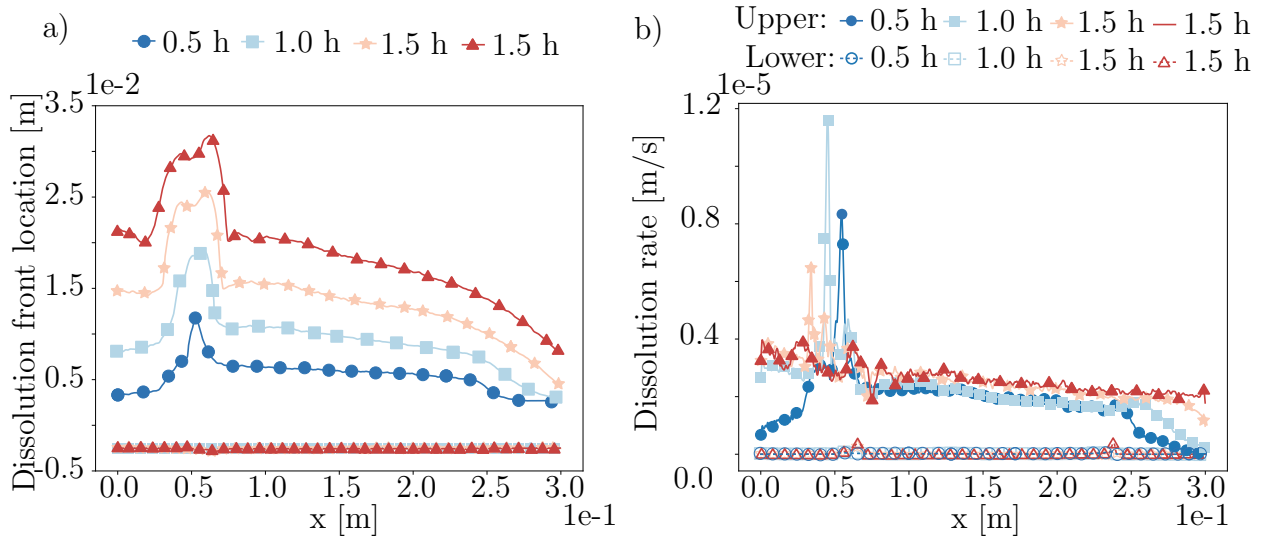
Figure 4.20: Dissolution distance (a) and dissolution rate (b) at different time under horizontal dissolution

emulates real dissolution phenomena. The dissolution rate of the upper front near the inlet is large at the early stage of dissolution and decreases with time. The rate along the rest of the upper front increases slightly during the dissolution process. However, the trend that the dissolution rate decreases along the flow path remains unchanged. The large difference between the dissolution rate along the upper surface highlights the challenge of controlling the dissolution of a horizontal cavity and that the location of the inlet is a significant factor.

The dissolution rate, the dissolved mineral mass fraction, and velocity distribution along the fronts after 2.5 h dissolution are illustrated in Figure 4.21. Figure 4.21(a) shows that at the top area of the cavity (the upper left corner near the inlet), the mass fraction of dissolved mineral is low, and the gradient of the mass fraction between the brine in the cavity and dissolution front is higher than other areas. It explains why the large dissolution rate and dissolution distance are located at the upper left corner, as shown in Figures 4.21(c)

a) Dissolved mineral mass fraction 0.00 0.13 0.26

b) Brine flow vercity magnitude [m/s] 0.00 0.02 0.04

c) Dissolution velocity [m/s] Upper Lower
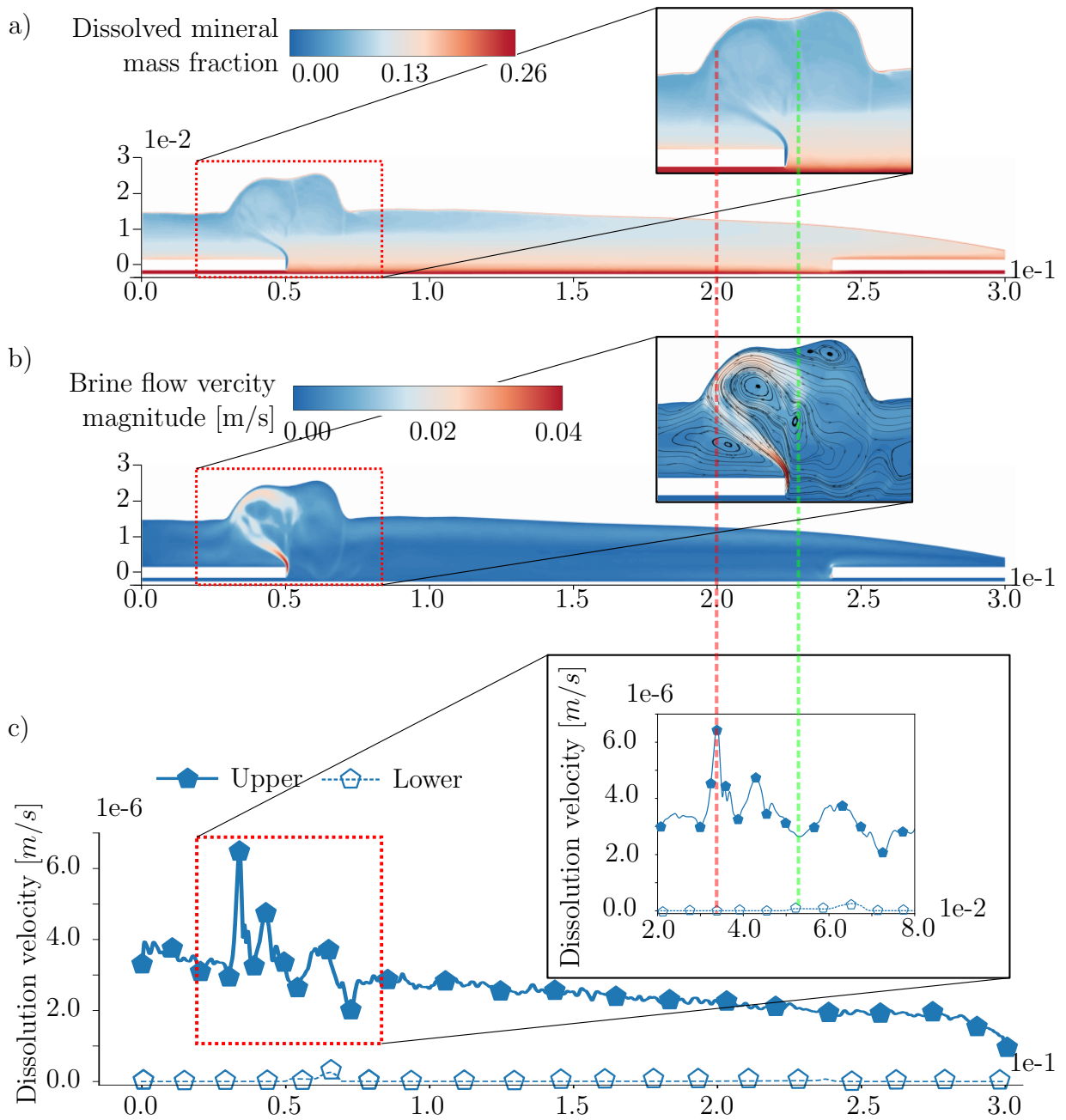
Figure 4.21: Dissolved mineral fraction(a), brine flow velocity(b), and dissolution rate (c) distribution for horizontal dissolution at 2.5 h

and [4.20](#).

Under the horizontal dissolution scenario, gravity is perpendicular to the inlet velocity direction. The fresh water injected from the inlet flows to the top region of the cavity because of buoyancy. When the injected freshwater gets in touch with the solid salt, the brine density increases and circulates downwards due to gravity, and a vortex is created. The fluid flow pattern is affected by the development of the vortex, and that is why the streamlines show that the fresh water does not flow directly to the top but goes back to the left and then flows upwards. The brine flow velocity is accelerated in the cavity near the inlet because of the combined effect of buoyancy and vortex formation. The brine velocity acceleration during the dissolution process is also reported in experimental work[65], indicating that the proposed model emulates brine flow patterns in the cavity.

Significant oscillations of the dissolution rate are observed near the inlet section near 0.5 m (Figure 4.21(c)) and result from the complex flow pattern in this region. The eddies (Figure 4.21(b)) near the inlet region results in brine advection near the front. The flow takes dissolved minerals from the dissolution front more rapidly, leading to a larger dissolution rate, as marked with the red dash line. At the location marked with a green dash line, there are two opposite rotating vortexes. The two vortexes cause accumulation of dissolved minerals near the front, causing a decrease in dissolution rate. Similar behaviour is reported in Chapter 3.

In the region below the inlet and outlet, fresh water can not flow into the saturated area because of the buoyancy force (Figure 4.21(b)), so the brine concentration does not noticeably change (Figure 4.21(a)). This leads to negligible dissolution at the lower front (Figure

The buoyancy effect has an impact on the brine flow, causing the generation of the complex eddies that affect the dissolution pattern in the horizontal scenario. The model proposed in this work reproduces the primary characteristics of the laboratory experiments and provides insights into the mechanics of flow and dissolution in this system which were difficult to elucidate from the experiments alone.

Chapter 5

Simulation of large-scale turbulence-driven cavern development by dissolution mining

5.1 Introduction

In this chapter, the SCI-FIE model discussed in Chapters 3 and 4 is extended to integrate the $k - \omega - SST$ turbulence model to enable the simulation of industrial-scale dissolution mining. The complex flow phenomena, which appear in both the direct and reverse dissolution methods used to develop vertical caverns, are studied and compared. The impact of the use of air/oil blankets, different injection velocity, and the influence of a single horizontal insoluble interlayer on cavern shape complexity is also investigated. This work advances the understanding of the interaction between turbulent brine flow and mineral dissolution and identifies several novel mechanisms affecting large cavity development.

5.2 The Improved Strategically Coupled Inertial Flow and Interface Evolution (SCI-FIE) model

The SCI-FIE model enables the simulation of problems and time scales up to that of benchtop experiments; however, at present the methodology is too computationally expensive for industrial-scale applications (as discussed in Chapters 3 and 4). This stems from the use of Direct Numerical Simulation (DNS) to solve the Navier-Stokes equations. In DNS simulations, all the flow motions are resolved, giving detailed information about velocity, density, and pressure, and capturing kinetic energy dissipation and dynamic eddy evolution at different scales. However, this resolution comes at the cost of a need for a large number of cells and grid points, and extensive computational resources. Additionally, the extensive flow information provided by DNS is often significantly more than engineers need [75].

In this Section, the extension of the SCI-FIE model to full-scale systems is achieved by replacing DNS with the solution of the Reynolds-Averaged Navier-Stokes (RANS) equations. The RANS equations are derived as the time-averaged behaviour of the turbulence, contributing to a reduction in computational time and resources. The application length and time scale of RANS are much larger than the scale of DNS [76], which is desirable for the large space and time scale dissolution simulation process studied in this work. Additional equations are introduced to close the model to calculate the turbulence effect in the RANS model. The $k - \epsilon$ model and $k - \omega$ model are two popular models used to help calculate the turbulent effects. The standard $k - \omega$ model tends to yield a more accurate prediction of the boundary layer near the wall, but is sensitive to the boundary condition of the inlet and the initial condition of the free flow region [77]. In contrast, the standard $k - \epsilon$ model more accurately predicts the free flow, but needs special treatment (a wall function) to simulate the flow near the wall [78]. To overcome the shortcomings of these two models,

the $k - \omega - SST$ model was developed to combine them. It applies the $k - \omega$ model at the boundary layer region and uses the $k - \epsilon$ model to simulate the fluid flow outside the boundary layer [79]. An effective large-scale dissolution model requires robust turbulent brine flow simulation in a large domain over long simulation times and precise brine flow analysis near the domain boundaries to accurately model dissolution front evolution; thus herein, the $k - \omega - SST$ model is used to simulate the brine flow in the cavity.

5.2.1   Governing equations

The governing equations used to simulate the dissolution process are those of the RAND model and are implemented in ANSYS FLUENT^{TM}, which is called from the SCI-FIE code. The model involves turbulent brine flow, dissolved mineral transport, and the slow movement of the cavern boundaries. The equations include mass and momentum conservation of brine and mass conservation of the dissolved mineral in the cavity and along the dissolution boundaries.

A cavity under construction is filled with brine of non-constant density/concentration and a blanket fluid (gas or oil). Brine is the only fluid explicitly simulated, as the effect of the blanket fluid is incorporated through the definition of the fluid domain and boundary conditions. The brine is assumed to be a Newtonian fluid with a constant temperature. Brine mass conservation in the cavity is governed by [75],

$$\frac{\partial \rho}{\partial t} + \frac{\partial}{\partial x_i}(\rho u_i) = 0 \tag{5.1}$$

in which ρ is the brine density; t is time; and u_i is brine velocity. The Einstein summation convention is used in this equation and those to follow.

The brine flow in the cavity is unsteady and irregular (turbulent). Quantities, such as mass and momentum, can fluctuate in time and space. In the RANS model, the time-averaged flow properties are solved, and the instantaneous fluctuations are ignored. The relevant conservation of momentum equations are:

$$\frac{\partial}{\partial t}(\rho u_i) + \frac{\partial}{\partial x_j}(\rho u_i u_j) = -\frac{\partial p}{\partial x_i} + \frac{\partial}{\partial x_j}\left(\sigma_{ij} - \rho \overline{u_i' u_j'}\right) + \rho f_i \tag{5.2}$$

in which p is the fluid pressure; σ_{ij} is the shear stress and can be calculated as $\sigma_{ij} = \left[\mu\left(\frac{\partial u_i}{\partial x_j} + \frac{\partial u_j}{\partial x_i} - \frac{2}{3}\delta_{ij}\frac{\partial u_k}{\partial x_k}\right)\right]$; μ is the dynamic viscosity; δ_{ij} is Kronecker delta; $-\rho \overline{u_i' u_j'}$ is the turbulence kinetic energy production term; and f_i denotes the gravity acceleration.

The turbulence kinetic energy production term is modelled with the Boussinesq hypothesis, and the Reynolds stress tensor is presumed proportional to the mean deformation rate,

$$-\rho \overline{u_i' u_j'} = \mu_t\left(\frac{\partial u_i}{\partial x_j} + \frac{\partial u_j}{\partial x_i}\right) - \frac{2}{3}\left(\rho k + \mu_t \frac{\partial u_k}{\partial x_k}\right)\delta_{ij} \tag{5.3}$$

in which k is the turbulent kinetic energy; and μ_t is the turbulent viscosity; they both are needed to close the turbulence model.

In the $k - \omega - SST$ model, the turbulent eddy viscosity is calculated as,

$$\mu_t = \frac{a_1 \rho k}{max\left(a_1 \omega, SF_2\right)} \tag{5.4}$$

in which ω is specific dissipation rate; α_1 is constant value, and S is an invariant measure of the strain rate, calculated as $S = \sqrt{\frac{1}{2}\left(\frac{\partial u_i}{\partial x_j} - \frac{\partial u_j}{\partial x_i}\right)\left(\frac{\partial u_i}{\partial x_j} - \frac{\partial u_j}{\partial x_i}\right)}$, F_2 is one of the blending functions.

The turbulent kinetic energy and specific dissipation rate are governed by,

$$\frac{\partial}{\partial t}(\rho k) + \frac{\partial}{\partial x_i}(\rho u_i k) = p_k - \beta^* \rho k \omega + \frac{\partial}{\partial x_i}\left[(\mu + \theta_k \mu_t)\frac{\partial k}{\partial x_i}\right] \tag{5.5}$$

$$\frac{\partial}{\partial t}(\rho \omega) + \frac{\partial}{\partial x_i}(\rho u_i \omega) = \alpha \rho S^2 - \beta \rho \omega^2 + \frac{\partial}{\partial x_i}\left[(\mu + \theta_\omega \mu_t)\frac{\partial \omega}{\partial x_i}\right]$$
$$+ 2(1 - F_1)\rho \theta_{\omega 2}\frac{1}{\omega}\frac{\partial k}{\partial x_i}\frac{\partial \omega}{\partial x_i} \tag{5.6}$$

The model coefficients in equations (5.5) and (5.6) are calculated by: $\theta_k = F_1 \theta_{k1} + F_2 \theta_{k2}$; $\theta_\omega = F_1 \theta_{\omega 1} + F_2 \theta_{\omega 2}$; $\alpha = F_1 \alpha_1 + F_2 \alpha_2$; $\beta = F_1 \beta_1 + F_2 \beta_2$, where F_1 and F_2 are blending functions defined as:

$$F_1 = \tanh\left\{\left\{\min\left[\max\left(\frac{\sqrt{k}}{\beta^* \omega y}, \frac{500\nu}{y^2 \omega}\right)\right], \frac{4\rho \theta_{\omega 2} k}{CD_{k\omega} y^2}\right\}^4\right\} \tag{5.7}$$

$$F_2 = \tanh\left\{\min\left[\max\left(\frac{\sqrt{k}}{\beta^* \omega y}, \frac{500\mu}{y^2 \omega \rho}\right)\right]^2\right\} \tag{5.8}$$

in which $CD_{k\omega} = \max\left(2\rho \theta_{\omega 2}\frac{1}{\omega}\frac{\partial k}{\partial x_i}\frac{\partial \omega}{\partial x_i}, 10^{-10}\right)$; and y is the distance to the nearest wall.

Research shows that the choices of coefficients in (5.5) and (5.6) in the suggested range

do not translate into a significant difference in the turbulent flow prediction [80], so the suggested constants values listed in Menter *et al.* [81] are used in this paper: $\beta^* = 0.09$, $\alpha_1 = 5/9$, $\alpha_2 = 0.44$, $\theta_{k1} = 0.85$, $\theta_{k2} = 1.0$, $\theta_{\omega 1} = 0.5$, $\theta_{\omega 2} = 0.865$, $\beta_1 = 3/40$, $\beta_2 = 0.0828$.

The transport of dissolved minerals in the cavity involves both convection and diffusion. Turbulence triggers more convection and the dissolved mineral transport rate is higher. An additional diffusion term related to the turbulent eddy viscosity (μ_t) and the turbulent Schmidt number (Sc_t) is added to the governing equation to reflect the turbulence effect on dissolved mineral transport. The transfer of the dissolved minerals in the turbulent brine is governed by,

$$\frac{\partial}{\partial t}(\rho \Phi) + \frac{\partial}{\partial x_i}(u_i \rho \Phi) = -\frac{\partial}{\partial x_i}\left(\left(-\rho D_s + \frac{\mu_t}{Sc_t}\right)\frac{\partial \Phi}{\partial x_i}\right) \tag{5.9}$$

in which Φ is the mass fraction of the soluble mineral in the brine; D_s is the mass diffusion coefficient of the mineral in brine; Sc_t is set to be 0.7 in this work.

The density of brine changes because minerals are dissolved from the solid mineral surface. The brine density is assumed to depend only on the mass fraction of the dissolved minerals (as discussed in Chapter 3), expressed as,

$$\rho = \frac{\rho_w \rho_s}{\rho_s - \Phi(\rho_s - \rho_w)} \tag{5.10}$$

in which ρ_w represents the density of water; and ρ_s denotes the density of the pure solid mineral rock.

5.2.2 Dissolution front

Dissolution occurs at the interface between the brine and solid mineral; it is assumed to happen on a zero-thickness interface, called the dissolution front. The gradient of the brine concentration at the dissolution front drives the process. As observed in simulations, laboratory work, and field studies, the time scales of dissolution and brine flow are significantly different, and the dissolution rate is much less than the brine flow velocity[62, 64, 63, 69], which allows these processes to be modeled in a loosely coupled fashion (as discussed in Chapters 3 and 4).

Following Chapter 3, the time-averaged (quasi-steady) dissolution rate (front velocity) is

$$v_{\mathrm{d}} = \frac{\overline{\rho}}{(\rho_{\mathrm{s}} + \overline{\Phi}\rho_{\mathrm{w}} - \overline{\Phi}\rho_{\mathrm{s}})} \left(-D_{\mathrm{f}} \frac{\partial \overline{\Phi}}{\partial n} \right). \tag{5.11}$$

in which $\overline{\Phi}$ is the time-averaged (quasi-steady) mass fraction of the soluble mineral (discussed below); $\overline{\rho}$ is the time-averaged brine density and calculated by replacing Φ by $\overline{\Phi}$ in (5.10); and D_{f} is the diffusion coefficient of the dissolved mineral close to the dissolution front.

The SCI-FIE model uses two time steps, a macro time step: τ, which is used to update the dissolution front; and a micro time step: Δt, which is used by the CFD simulator ($\tau \gg \Delta t$). In strongly coupled approaches, such as implemented in COMSOL (Chapter 2), $\Delta t = \tau$; however, this makes many analyses intractable. The SCI-FIE model takes advantage of the time-scale differences in the dissolution processes to accelerate computations without undue loss in accuracy.

The location of the dissolution front is updated at the end of each macro step using the front velocity (5.11), such that the increment in the normal displacement of the front is $\Delta d = v_d \tau$. The time-averaged mass faction, $\overline{\Phi}$, is computed as follows: a CFD simulation with micro time step Δt is conducted using the Reynolds-averaged Navier–Stokes equations. The initial conditions for the CFD simulation are obtained by projecting the fluid flow solution from the previous macro time step and domain onto the new mesh of the domain defined by the new dissolution front. The CFD simulation is conducted over a pseudo time period $t^* \ll \tau$, chosen to be long enough so that the system evolves from its initial conditions (guess) to a quasi-steady state. Conceptually, it is useful to assume that t^* can be divide into two distinct periods: $t^* = t^t + t^{qs}$, t^t a transient period, and t^{qs} a quasi-steady period. The fluid behaviour at any point in the domain during the quasi-steady period is not constant but fluctuates in a consistent and repetitive manner. To obtain the time-averaged mass fraction $\overline{\Phi}$, the CFD solution is sampled over a suitable period, $t^s \le t^*$, specifically.

$$\overline{\Phi} = \frac{1}{t^s} \int_{t^*-t^s}^{t^*} \phi \, dt \tag{5.12}$$

The purpose of the CFD brine flow simulation is to determine the time-averaged brine concentration for a given fluid domain. So, the time in the CFD simulation is a pseudo-time and is separate from the time used to advance the dissolution front at the macro scale. By analogy, the pseudo-time of the CFD simulation can be compared to iterations of Newton's method, in which each iteration (pseudo time step) moves one from an initial guess (initial condition) towards a converged solution (steady time-averaged value of concentration).

Discussion of CFD simulation time t^* and sample period t^s

The CFD simulation time t^* and sample period t^s are key inputs to the SCI-FIE model, the choice of which will affect both the computational cost and the accuracy. Ideally, t^* and t^s should be selected such that $t^t = t^* - t^s$, sampling begins after the transient phase, and t^s is just large enough to yield accurate measures of time-averaged concentrations. However, the selection of t^* and t^s is challenging as the length of the transient phase is not known *a priori* and varies during the evolution of the cavity.

To illustrate the role of these inputs, consider a simulation of reverse dissolution starting from an initially perfectly cylindrical cavern; fresh water is injected at a velocity of 1 m/s from a central pipe; the inlet is at a depth of 5 m and the outlet is at a depth of 10 m.

Figure 5.1 illustrates results for two CFD brine flow simulations for two different fluid domains, the initial domain and the domain after 10^5 s of injection. Two concentric tubes are inserted into the cavity form the center of the cavern top to serve as the fresh water injection well and brine discharge well. The fresh water is injected through the outer tube, which has a radius of 0.2 m and reaches 5 m depth. The brine with the dissolved mineral is discharged through the inner tube, whose radius is 0.1 m and is 10 m deep. The dissolved mineral mass fraction gradient normal to the interface at four monitoring points is plotted versus time; the values are normalized by the largest $d\phi/dn$ among the four monitoring points.

It can be observed that at each monitoring point, the concentration gradient initially experiences large fluctuations initially, but eventually reaches a quasi-steady state with small
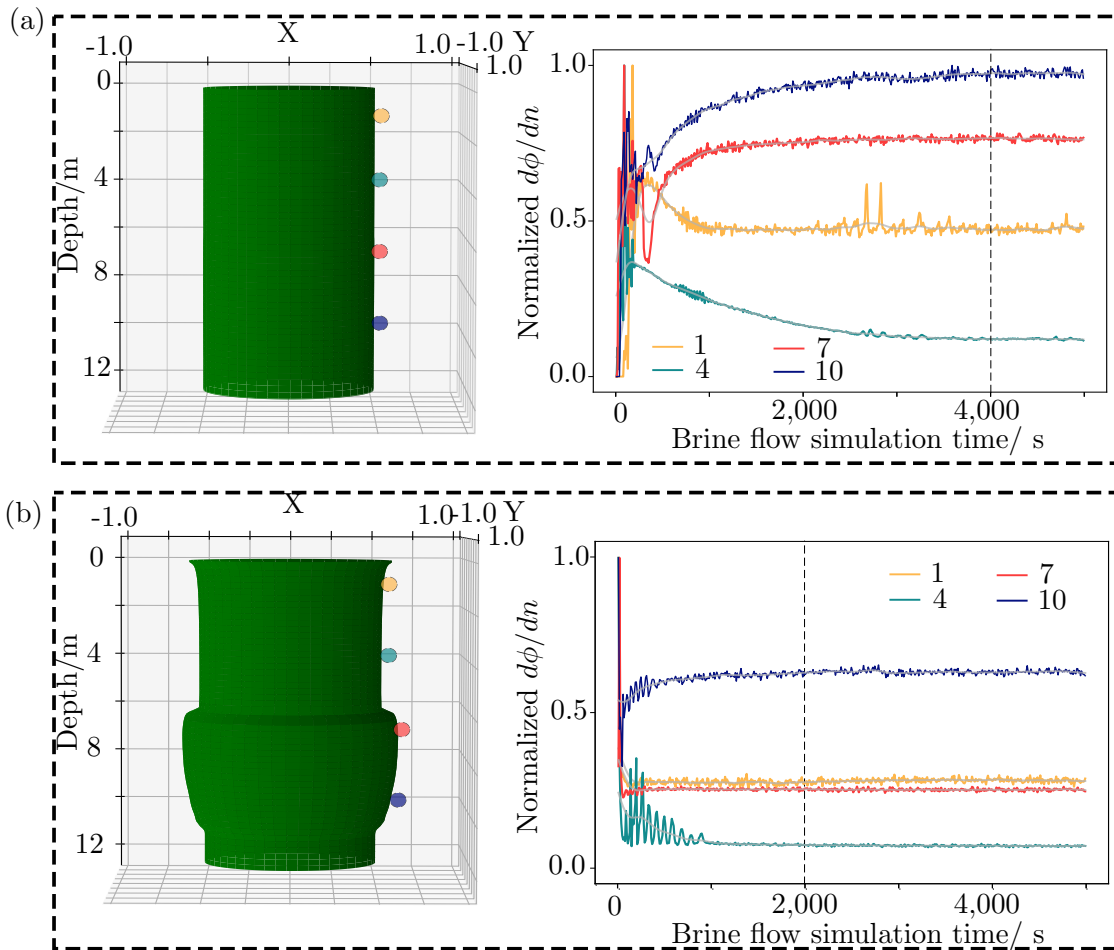
110

Figure 5.1: Change of $d\phi/dn$ at different locations with simulation time at 0 s (a) and 10^5 s (b).

oscillations. The time needed to reach the quasi-steady state (t^t) also varies with time, from about 4000s for the domain in Figure 5.1a) to about 2000s for the domain in Figure 5.1b). The source of the difference stems from the initial conditions used. In the first stage, the initial conditions assume that the fluid is at rest, while for the later stages, the initial condition is obtained by projection of the CFD solution from the previous stage. In the second case, the initial conditions are a better guess of the time-averaged quantities. See discussion in Section 5.2.3 and Chapter 4.

The end of the transient period (start of the quasi-static period) is difficult to define, a useful indicator is when the fluctuation of the mass fraction gradient at all locations along the front is less than 0.5 % of the maximum oscillation of the whole simulation time (5000 s).

To explore how the choice of t^* and t^s impacts the analysis, Figure 5.2 illustrates the mass fraction gradient over pseudo-time and the various ways the time-averaged mass fraction gradient that could be computed from the time history curves. The two time histories shown in Figure 5.2(b) and (c), correspond to a monitoring point at a depth of 5m, for the domains illustrated in Figure 5.1(a) and (b).

It can be observed in the right side plots, that if t^* is chosen to be shorter than the length of the transient period (about 4000 s Figure 5.2(b) or about 2000 s Figure 5.2(c)) then the computation of the time-averaged mass fraction will be unstable no matter the choice of the length of sampling period, t^s. When t^* is chosen to be longer than the length of the transient period (about 4500 s Figure 5.2(b) or about 2500 s Figure 5.2(c)) then the computation of the time-averaged mass fraction will yield a stable value, relatively independent of choice of the length of sampling period, t^s.
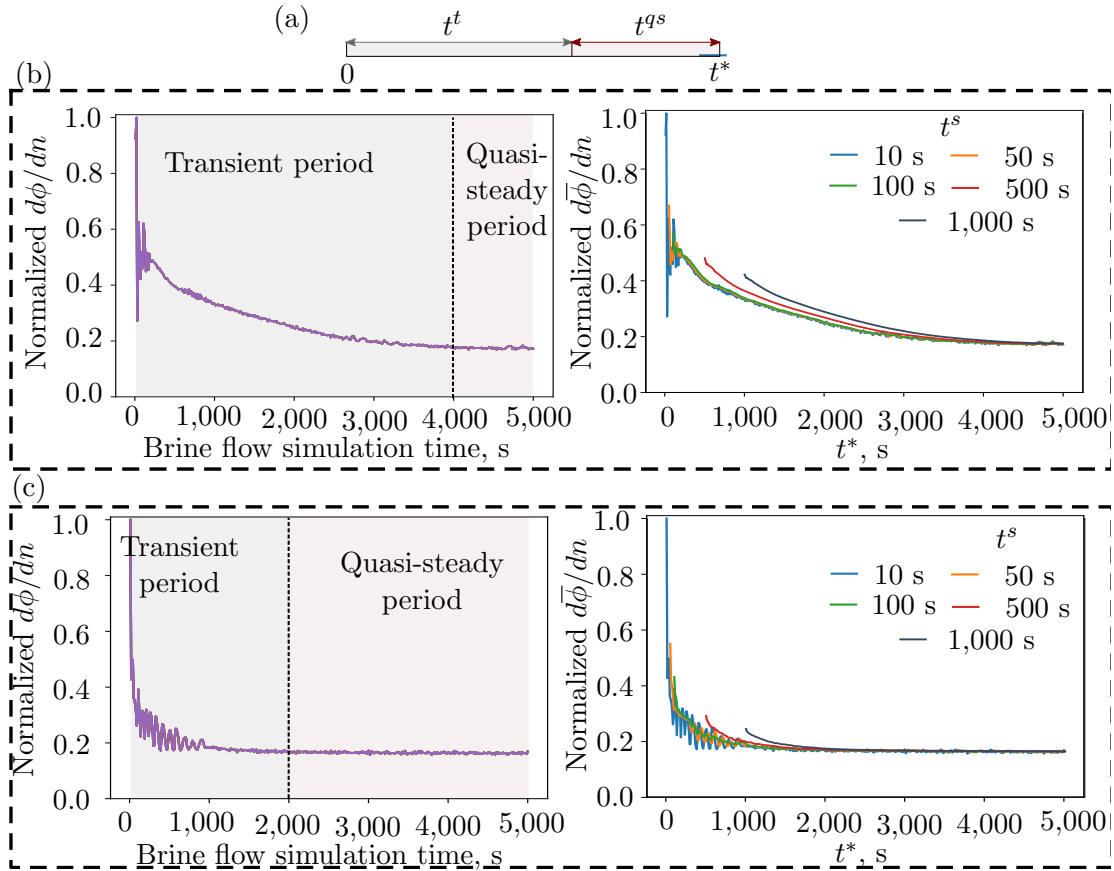
Figure 5.2: Sketch of t^* components(a), change of $d\phi/dn$ with simulation time, and effect of t^s length on the time-averaged mass fraction gradient normal to the interface at 0 s (b) and 10^5 s(c) at 5 m depth.

The optimum choice of t^s depends on the nature of the fluid system, domain boundary topology, etc. and the desired level of accuracy. When t^s is selected too small (10 - 50 s in this example), there will be large fluctuation in the time-averaged values even when $t^* > t^t$. When t^s is selected exceedingly large, the time-averaged values are smooth and consistent; however, the computational cost of the CFD simulations is unnecessarily severe ($t^s = 1000$s in this example) because t^* should be large. Thus, the ideal choice of t^s is a compromise; 100- 500 s is a good choice for t^s in this example.

Ideally, t^* should be as small as possible, as the total computational cost of the SCI-FIE model is proportional to t^*, which is proportional to the number of CFD time steps needed for each macro-step. Some expediency can be achieved by using different t^* (and t^s) at different macro time steps. In the examples presented below, we have found that $t^* = 4,500$ s and $t^s = 500$ s for the first macro step, and $t^* = 2,100$ s and $t^s = 100$ s for each subsequent macro step leads to efficient and accurate simulations.

The selection of t^* and t^s in other applications would rely on the experience of the analysis developer.

5.2.3   Implementation of the simulation algorithm

An efficient algorithm is developed to solve (5.1)-(5.11) numerically. The algorithm consists of four modules that are iteratively coupled: 1) Preprocessing for geometry and mesh generation; 2) Turbulent brine flow and dissolved mineral transport simulation; 3) Dissolution

114

front evolution calculation; 4) User-defined function (UDF) calculation and generation for the initial condition for the fluid dynamics simulation. The iteration and relation between the four modules are the same as in Chapter 4.

Several improvements are applied in Modules 1, 2, and 3 to improve the accuracy, reliability, and robustness of the model, which can thereby simulate the dissolution under turbulent flow conditions.

In Module 1, the commercial software ANSYS ICEM^{TM} is used to build the geometry of the brine-filled cavity and generate the mesh for simulation. An unstructured mesh that combines quadrilateral and triangular cells is used to conform to different cavity shapes: quadrilateral cells are located near the cavity boundary; the other area is discretized using triangular cells. Mesh element size is maintained relatively constant with each geometry update, and the number of cells increases with cavity enlargement. The commercial software FLUENT^{TM}, based on the Finite Volume Method (FVM), is used to calculate the $k - \omega - SST$ turbulent flow model in Module 2. The time-history data of the brine flow pressure, velocity, and dissolved mineral throughout calculation period t^* are written in text files and saved. Although the time-history data is saved throughout the turbulence simulation time t^*, only the data in t^s is used to calculate the averaged dissolution rate in Module 3. So, this approach is different from Module III that we presented in Chapter 4. The data is averaged over the sample period t^s to get the stable and reliable dissolution prediction based on the turbulent brine behaviour in a quasi-steady state.

5.3 Case studies

This section describes simulation results for different case studies. In this section, the case studies refer to the simulation cases for various dissolution mining scenarios. The first case investigates cavity evolution and brine flow patterns under reverse dissolution; the second case considers the influence of different dissolution methods on the cavern expansion, and the third case investigates the impact of a blanket on cavity evolution.

The initial cavity geometry for all cases is a cylinder with a diameter of 1 m and height of 12 m, as shown in the left of Figure 5.3. Two concentric tubes are inserted into the cavern from the top center to conduct fresh water injection and brine discharge. The outer tubing has a radius of 0.2 m and extends to a depth of 5 m. The inner tubing diameter is 0.1 m, and the tube bottom is 10 m deep. The top and bottom boundaries of the cavity are assumed to be insoluble rock formations. The cavern is surrounded by homogeneous solid dissoluble minerals. On the dissolution front, the mass fraction of dissolved minerals is set to be the saturated value of 0.264. To simplify the simulation and reduce solving time, a two-dimensional axisymmetric model is used.

5.3.1 Cavity evolution

In this section, the case of reverse dissolution with 0.5 m/s of fresh water velocity at the inlet is studied. In this work, reverse dissolution is defined as when the fresh water injection is higher in the cavern than the brine discharge location. So, the fresh water is injected through the outer tube, the brine is withdrawn through the inner tube. The Reynolds number reaches 5×10^6, and turbulent brine flow develops in the cavity. The dissolution

116

simulation time step τ is 10^5 s (≈ 1.16 day), and the total dissolution time is 5×10^6 s ($\approx$ 58 days).
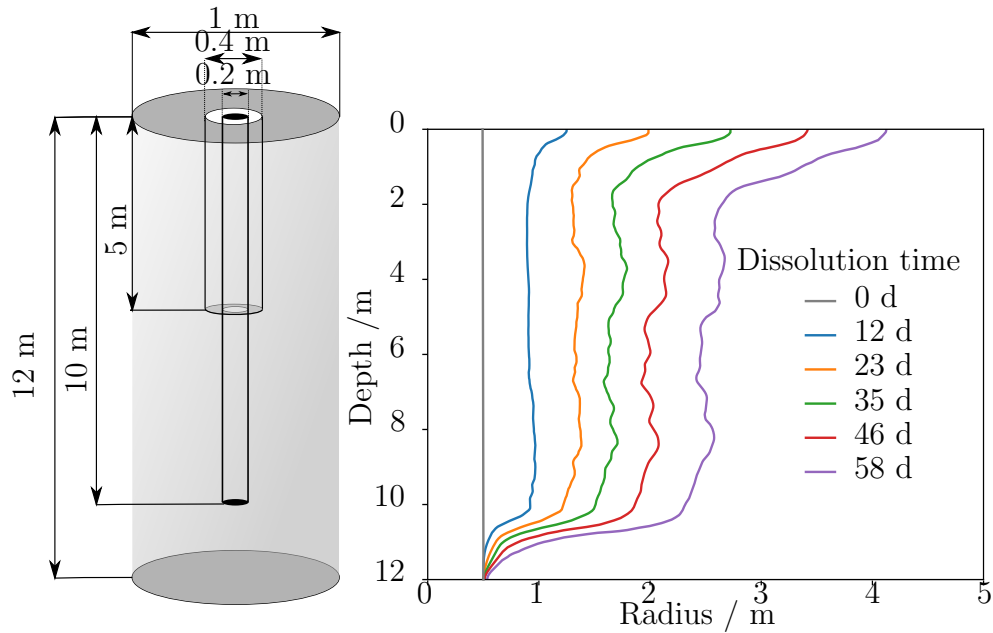
Figure 5.3: Dissolution front evolution with time.

The cavity boundary growth is shown in Figure 5.3. The dissolution rate of the front under the outlet location is low, but the boundary above the outlet undergoes significant change. The dissolution boundary is not smooth; we observe several irregular overhanging blocks, and the irregularity becomes more severe with time. The cavity top undergoes the most dissolution, resulting in the "morning glory" shape, and the roof span increases continually, shown in Figure 5.4. The irregular shape cavity develops despite the assumption of a fully homogeneous mineral; heterogeneity is therefore not the only reason for cavity wall irregularities in practice [17].
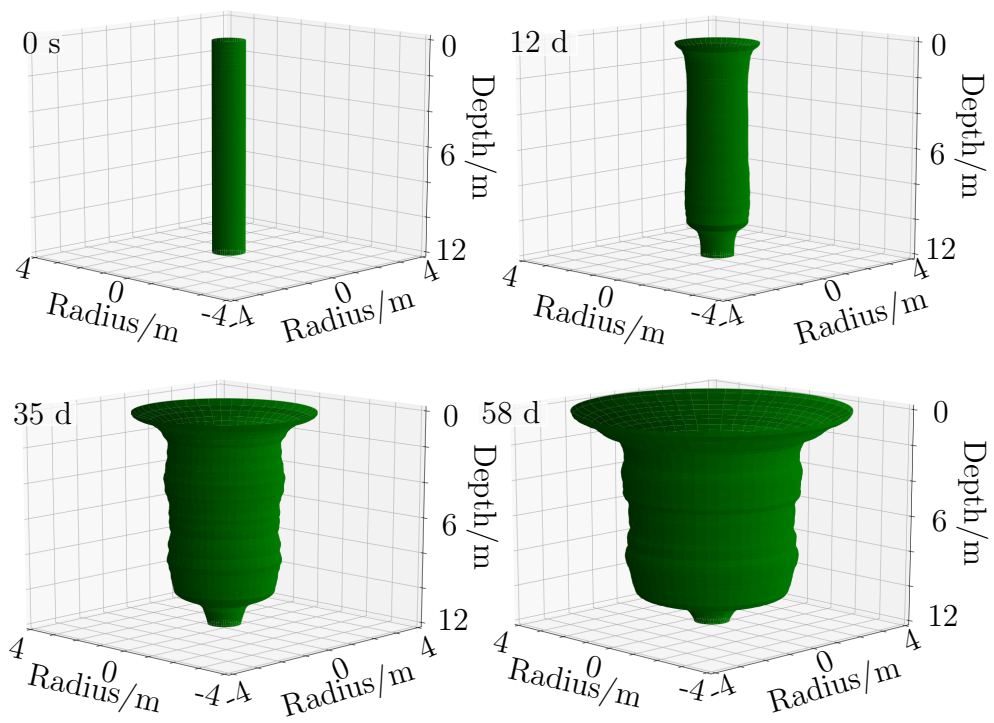
Figure 5.4: Cavity evolution.

The brine flow pattern in the cavity influences the dissolution process. To investigate how the turbulent brine flow affects the dissolution pattern, a snapshot of the dissolved mineral mass fraction distribution, the turbulent brine flow pattern, and the dissolution rate distribution at 29 d are illustrated in Figure 5.5. The fresh water injected into the cavity from the inlet is transported downward to the depth of 7 m, leading to the mineral mass fraction of the brine decrease near the inlet zone. Then, the fresh water does not flow to the deeper location but flows to the upper zone of the cavern because of buoyancy. The less concentrated brine keeps flowing upwards until it reaches the cavity top and changes direction to flow horizontally. The less concentration brine reaches the upper dissolution boundary, reducing the brine concentration near the dissolution front. The drop in dissolved mineral concentration at the cavern top increases the mineral mass fraction gradient near the dissolution front, and results in a high dissolution rate, as shown in Figure 5.5(c). This leads to the large dissolution growth at the cavity top, resulting in the " morning glory" shape. The dissolution of solid minerals increases the density of the brine, then the brine is transported downward along the dissolution front, as shown in Figure 5.5(b). When the brine reaches the bottom zone of the cavity (below the outlet), the brine is not denser enough to flow downwards further, and it changes flow direction towards the outlet, where the brine is discharged.

Dissolved mineral transport is governed by advection and diffusion, so the distribution of the dissolved mineral fraction is affected by turbulent flow, and it varies at different locations. The combination of the forced convection and buoyancy effect disturbs the overall flow pattern in the cavern, forming eddies and changes of brine flow direction. The vortexes result in an uneven distribution of the solution concentration in the upper part of the cavity, so the relation between the brine concentration distribution and depth is ambiguous.

119
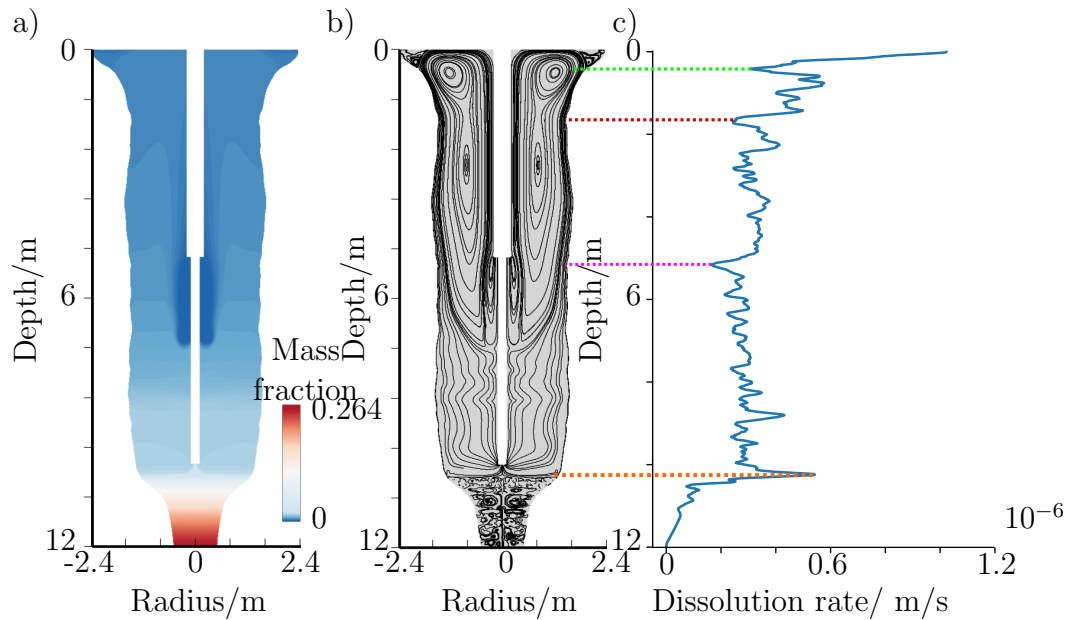
Figure 5.5: Averaged mass fraction and velocity distribution and dissolution rate distribution at 29 d.

Furthermore, the variations in brine flow pattern in the cavity affect the transportation of dissolved mineral near the dissolution fronts, resulting in fluctuations of the mass fraction gradient. The gradient fluctuations lead to dissolution rate oscillations, as illustrated in Figure 5.5(c). The relation between the dissolution rate and the depth is thus indeterminate. The simplification that brine concentration distribution and dissolution rate are linearly related to depth [82] is therefore not suitable for accurate cavity dissolution simulation.

There are several abnormal dissolution rate values along the dissolution front (Figure 5.5, dash lines). The green and red dash lines mark counter-rotating eddy mid points where the mineral mass accumulates. The two rotating eddies transport dissolved mineral toward a common point, increasing the local brine concentration and lowering the local dissolution

rate. The counter-rotating eddies' influence is one of the abnormalities source and has not been previously studied in large-scale cavity evolution. At the location marked with a purple dash line, the brine flow direction changes because the overhanging section hampers brine flow underneath the overhang, reducing convection, and elevating brine concentration because of a lack of a fresher water or low-concentration brine supply. The cavity shape strongly influences the brine flow pattern, which in turn affects the magnitude and distribution of dissolution rates along the cavity walls. The bidirectional coupling of dissolution and cavity shape change appears a novel, yet logical observation.

Another interesting feature appears in the lower part of the cavity (orange dash line). There is an interface between the lower and higher concentrations of brine, and at the interface, the brine flow changes the direction because it is not dense enough to flow downward, so it turns to flow horizontally. The brine flow takes more dissolved mineral from the dissolution front, causing a rapid increase in the dissolution rate above the interface. The brine underneath becomes mostly stagnant, largely isolated from the rest of the cavern flow system.

5.3.2 Cavity evolution under direct and reverse dissolution

Dissolution methods (reverse vs direct) influence cavern development. Direct dissolution is defined as when the fresh water injection location is lower than the brine discharge location. The outer tubing serves as the injection well under the reverse dissolution and serves as the discharge location in the direct dissolution mode. To get the same inlet fresh water flux and injection volume, the inlet velocity is set to be 0.5 m/s for reverse dissolution and 1.5 m/s for direct dissolution.
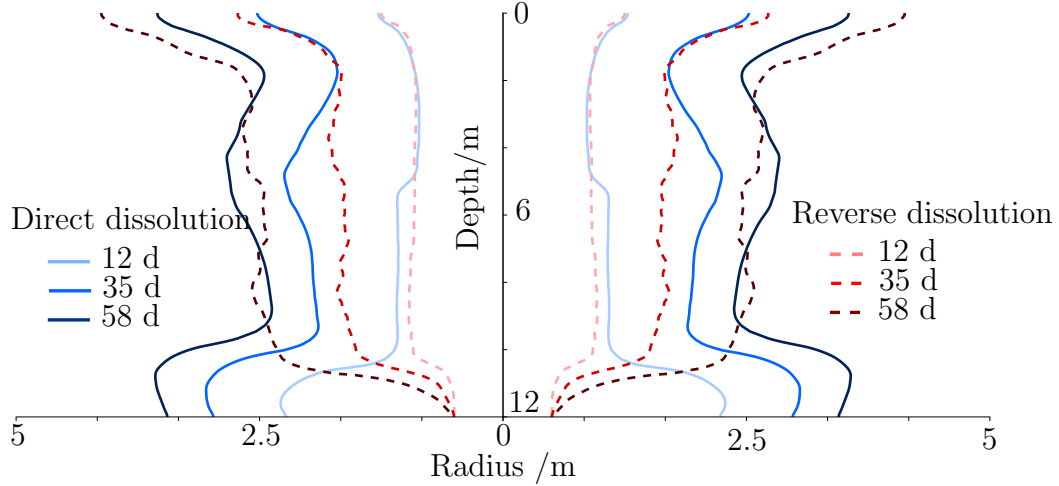
Figure 5.6: cavity outline difference between reverse and direct dissolution.

Cavity boundary evolution under direct and reverse dissolution modes are illustrated in Figure 5.6. The brine flow circulation direction strongly influences cavern shape because of differences in brine flow patterns. Under direct dissolution, the bottom of the cavity undergoes significantly more dissolution and forms a cavity shaped like a wide bottom decanter. The bottom of the "decanter" keeps expanding outwards and upwards, quite different from the reverse dissolution mode where the bottom of the cavity become stagnant and ceases to expand. The "morning glory" top also appears in direct dissolution, but its expansion rate is not as high as in reverse dissolution, so the roof span is substantially smaller after 58 d. Also, direct dissolution creates a large overhang at the middle part of the cavity, a potential concern.

Besides cavity shapes differences, the circulation mode affects average dissolution rate at the boundary and the cavity volume change is also affected (Figure 5.7). The average dissolution rate under direct dissolution is high at the beginning (around 8×10^{-7} m/s)

122
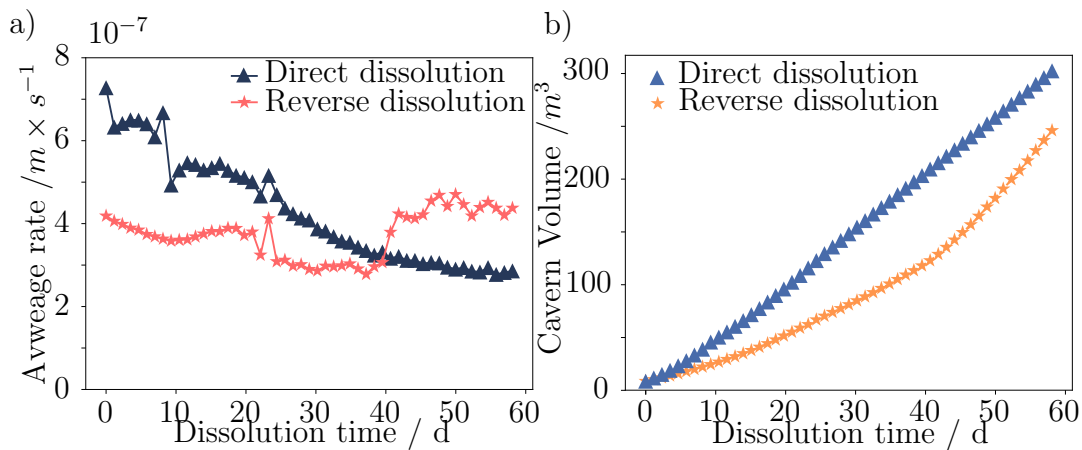
Figure 5.7: Change of average dissolution rate (a) and cavern volume (b) with time under direct and reverse dissolution.

and keeps decreasing to less than half its initial value after 46 d, and then stays stable. However, the average dissolution rate in reverse dissolution does not undergo significant change. The dissolution rate remains around 4×10^{-7} m/s before 40 d, and then slightly increases to approximately 5×10^{-7} m/s, because of the turbulent flow pattern changes in the cavern. The dissolution rate change is less significant than the direct dissolution scenario. Average dissolution rate differences can result in different cavity volume evolution trends (Figure 5.7(b)). Direct dissolution has apparent advantages in creating a large cavern during the early stage of construction, but the continuously direct dissolution leads to a drop of the dissolution rate, and a slowing of the cavity growth rate over time. The cavern growth rate under reverse dissolution is more consistent and increases sightly after injecting fresh water for 40 d.

The dissolved mineral mass fraction, brine velocity distribution and flow pattern in the cavity after 6 d and 52 d are shown in Figure 5.8. The scale of the dissolved mineral fraction (as shown in the figure legend) is changed to illustrate fraction distribution better.

Figure 5.8: Mass fraction (1) and flow pattern (2) after 6 d (a) and 52 d (b).

At the early stage of direct dissolution (6 d), the average dissolved mineral mass fraction in the cavity is low, with the highest value of 0.03. The combination of forced and natural brine convection leads to the generation of eddies, and strong convection results in the rapid decrease of the overall dissolved mass fraction in the cavity. This explains why the mass fraction of dissolved mineral is low and the average dissolution rat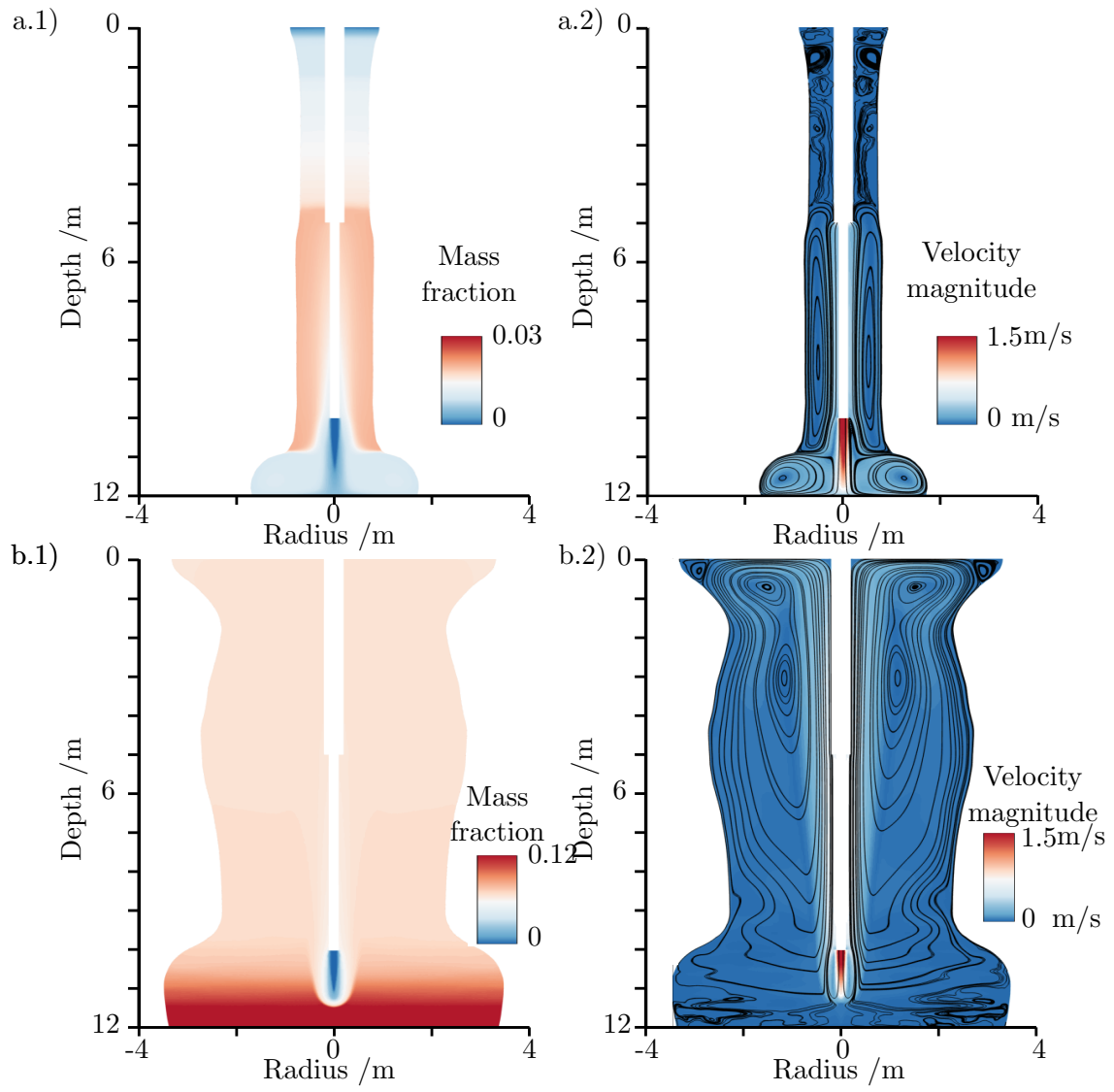e on the boundary is high in the early dissolution stage (Figure 5.7(a)). There is still significant variation in the mineral concentration in the cavity although the average dissolved mineral concentration is low. The mass fraction of mineral mass in the top and the bottom zones is less than the middle. The fresh water is injected at a relatively high velocity from the lower tubing and contacts the cavity bottom. The flow then changes direction toward the dissolution front, resulting in decreased dissolved mineral concentration and a larger dissolution displacement at the bottom, explaining the "decanter" shape that is formed. The brine flow in the "decanter" bottom area is complex. Vortexes are generated because of the dissolution front topology changes (Figure 5.8 (a.2)). The dissolved minerals at the bottom is carried upward by the eddies. Gravity (density buoyancy) promotes downward flow of brine as its density increases, resulting in the drop of mineral concentration near the top boundary, prompting a large roof span at the cavity top. Upward flow from the bottom and downward flow from the top contribute to the development of eddies at depths between 5 m and 11 m. The eddies trap the higher concentration brine and reduce the dissolution rate of the cavity boundaries in that area. At a depth of about 11 m, there are two eddies rotating in opposite directions, leading to an increase in brine concentration where they come together, and resulting in less dissolution at that location.

The cavity keeps expanding during the dissolution process, the average mass fraction in the cavity becomes higher than the value in the early stages (Figure 5.8 (b.1)). The denser

brine settles to the bottom of the cavity, reducing the mass fraction gradient near the front and decreasing the dissolution rate. The injected fresh water can no longer penetrate to the bottom because of buoyancy. The fresh water mixes with the brine, reducing its density, and the lighter brine is transported upwards along the tube, similar phenomena are also reported in other works [83]. Some of the lighter brine is discharged directly from the outlet because the outlet is located above the injection location. The directly discharged lighter brine does not flow to the dissolution front and does not directly get involved in the dissolution process (Figure 5.8 (b.2)). The "waste" portion of low concentration brine is the reason that causes increases in the dissolved mineral mass fraction in the cavity, and it is why the average dissolution rate drops with time, as illustrated in Figure 5.7 (a). An overhang has been created at a depth of 2 m because of the action of two eddies rotating in opposite directions, similar to the phenomena that appear in the reverse dissolution (Section 5.3.1).

The direct dissolution method can cause more bottom cavity dissolution than the reverse method, but the buoyancy effect is still significant, so the large span roof can not be avoided by simply changing the dissolution method from reverse to direct. An optimal cavern shape is still hard to achieve because of the large overhangs generated in the middle part of the cavity. It can be concluded that the combined effect of turbulence and gravity on the brine flow can contribute to the irregular shape of the cavity, regardless of the brine circulation direction.

5.3.3 Cavity evolution under different blanket locations

The application of a blanket at the cavern top is widely used to control upwards disso-lution and help achieve a better shape with a lesser roof span. This section investigates the influence of blanket location on the dissolution pattern. The fresh water is injected from the outer tube to conduct reverse dissolution, and the injection velocity is 0.5 m/s. During the simulation, the brine-filled cavity top boundary, where the blanket is applied, is assumed to be a no-slip and no-dissolution boundary. This makes the model suitable for the simulation with large viscosity blanket fluid, such as oil. The total dissolution time simulated is 5×10^6 s ($\approx$ 58 d). The dissolution process is divided into five stages for blanket application to study the cavern development under different blanket locations, and each stage lasts for 10^6 s (about 11.6 d). In the first stage, there is no blanket; the blanket is applied at a depth of 2 m in the second stage ($12d - 23d$) then, the blanket is lowered to 3 m and 4 m at the beginning of stages 3 and 4, respectively. In the last stage ($46d -$ 58d), the blanket is raised to 1 m depth.

Cavity evolution during the simulation is shown in Figure 5.9. To illustrate the cavity shape differences, the cavity outline evolution of both scenarios (blanket/no blanket) is plotted. The results show that the cavity will have a jagged boundary at the top when the blanket moves downwards, which is also reported in lab-scale experiments [84]. The application of the blanket creates an "artificial roof" in the cavity; the brine flow then can not reach the mineral above the "artificial roof", and a flat boundary is formed (Figure 5.9). Several flats are generated as the blanket moves downwards, hence a jagged shape is developed. When the blanket rises back to 1 m, the jagged boundary below the blan-ket is gradually smoothed in the last dissolution stage. Adjusting the blanket location will
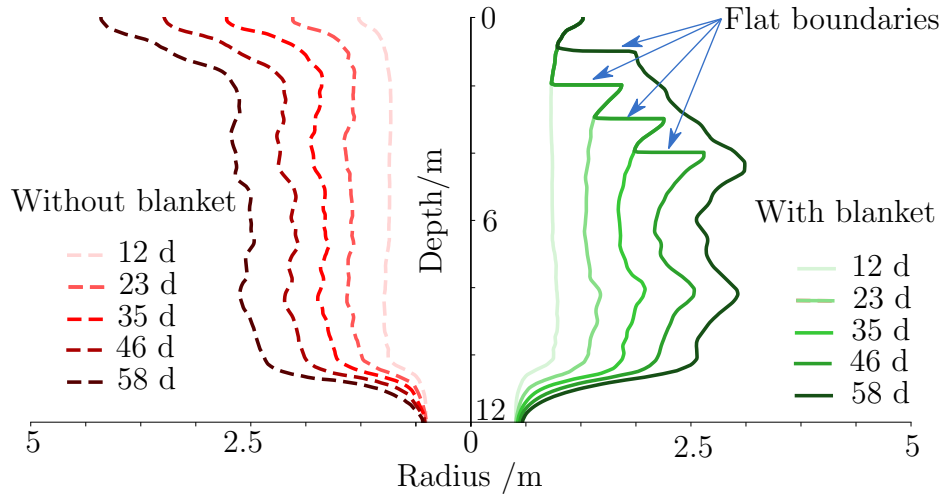
Figure 5.9: Cavity boundary evolution with time.

smooth the jagged boundary below the blanket, but a new flat boundary (jagged boundary) is generated at the new blanket location. The results show that the blanket application can prevent large cavern roof span generation (morning glory effect) and promote a more barrel-shaped cavern. However, a complex shape cavern is still developed with a blanket application strategy. In addition to the jagged boundary, the use of the blanket fluid leads to more outwards expansion of the cavity and results in more uneven dissolution of the boundary. After dissolution for 46 d, the average radius of the cavity under the blanket is larger than the one without a blanket at the location between 2-8 m depth. The large overhanging block generated near the depth of 6 m after 46 d dissolution is part of the more irregular shape cavity. The irregularity of the cavity at the central part can not be eliminated and become even greater when the blanket location changes. The overhang growth may be an issue for cavern use, so more attention to the large irregular overhangs generated at the center of the cavern is required when the blanket fluid is used to conduct cavern shape control.
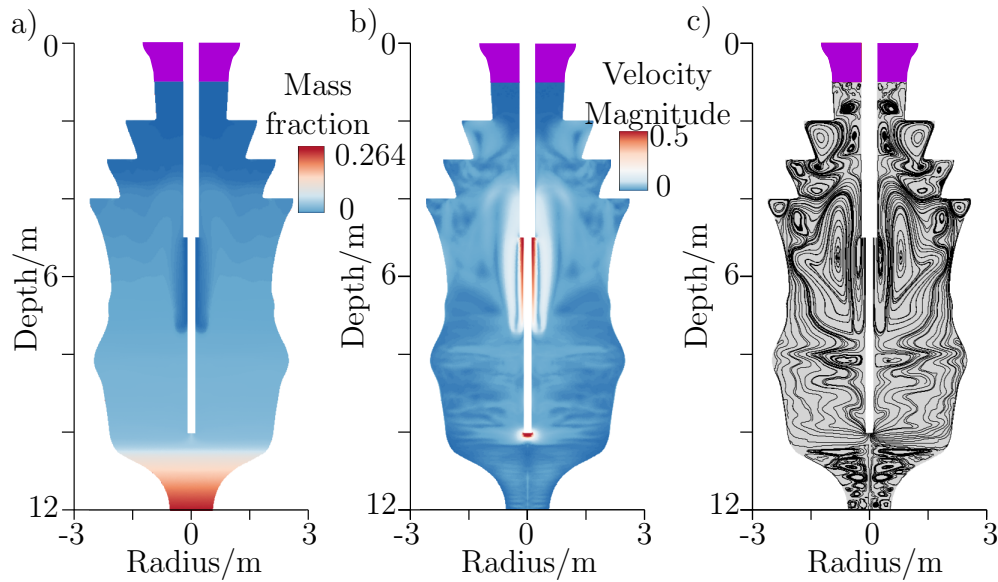
Figure 5.10: Dissolved mineral mass fraction (a), brine flow velocity (b), stream line of brine flow (c) on 46 d (at the beginning of stages 4).

Figure 5.10 illustrates the dissolved mineral mass fraction and brine flow pattern at 46 d. The blanket fluid occupies the zone above 1 m and is marked with purple. The lighter brine is trapped at the top of the cavity because of the buoyancy effect and increases the dissolution rate of the upper cavity (below the blanket). The change of blanket fluid location results in multiple overhangs and leads to more complex brine flow patterns (Figure 5.10 (b)) than the scenario without a blanket.

By comparing Figure 5.10 (b) and Figure 5.10 (c), it can be seen that many vortexes with high flow velocity develop in the upper portion of the cavity. The jagged shape boundaries help generate the eddies, causing changes in the brine flow direction. The eddies contribute to more intense advection near the cavity boundary, leading to local changes in brine velocity (as shown in Figure 5.10 (b)). The flow near the jagged boundaries transports away more dissolved mineral and promotes an increase in concentration gradient,

resulting in a increasing dissolution rate and smooths the jagged shapes, increasing the regularity of the cavity. However, while small irregularities are eliminated, a large overhang is generated; eddies develop in the central cavity part and keep growing, leading to an increase in brine concentration near the boundary near the depth of 6 m. The increase in brine concentration decreases the dissolution rate, contributing to the large overhang development.

The complex dissolution pattern indicates that there is competition between the two mechanisms of dissolution during large cavity dissolution. The first one is that eddies and brine flow, which bypass small and deep irregularities in the cavity wall, can act to smooth the small irregularities. The second mechanism is that the surface deviations lead to the generation of eddies that promote variable local dissolution rates and increase cavity surface irregularity, reinforcing and increases surface complexity. These competing processes have apparently not been noted in previous studies.

The application of the blanket will also affect the construction efficiency of the cavern. Figure 5.11 shows that the application of a blanket fluid slows down the construction of the cavity. The injection of blanket fluid into the cavity reduces the contact surface of the brine and the solid mineral, resulting in a decrease in the mineral dissolution rate. The construction efficiency of the cavern is a significant consideration for an investment into salt cavern utilization for storage, so, the negative impact of the blanket application on construction efficiency should be considered when planning salt cavern development for storage.
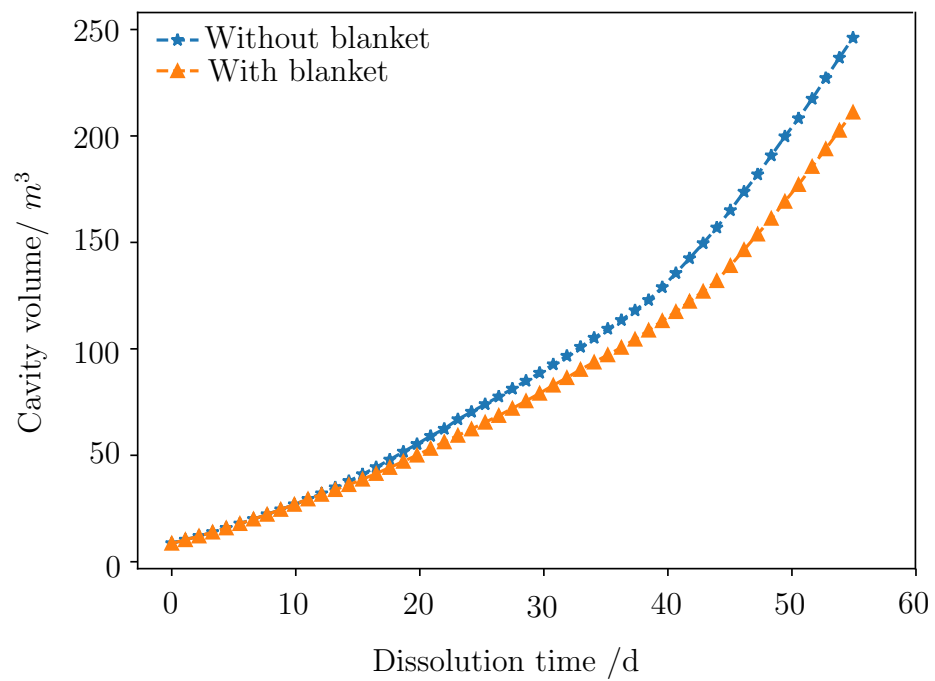
Figure 5.11: cavity volume change with time.

Chapter 6

Conclusion

6.1 Concluding remarks

Mineral dissolution involves brine flow, dissolved mineral transport, and slow movement of the dissolved cavity boundaries. Shape control is important in underground caverns developed by dissolution mining if they are to be used for storage (CAES, natural gas, hydrocarbon fluids...), and the key factors affecting the mineral dissolution procedure need to be quantified. The three main objectives in this thesis support the simulation of the mechanisms which result in the ultimate cavern shapes. Strategically Coupled Inertial Flow and Interface Evolution (SCI-FIE) models have been developed and are proposed to solve the complex nonlinear system of equations that governs the mineral dissolution and fluid flux process.

The first objective is to develop a tractable numerical simulation model involving free brine flow and physically-driven boundary evolution. A novel numerical algorithm for solving

the nonlinear problem of mineral dissolution with a moving boundary is proposed. The nonlinear equations of brine continuity, conservation of momentum (Navier-Stokes), and advection-diffusion are solved using the finite volume method. A generalized nonlinear dissolution rate equation is solved rather than a linear or empirical one to get more physically correct predictions of the cavity shape evolution. The dissolution rate is coupled with brine transport and solved under a quasi-steady-state condition to obtain the movement of the dissolution boundary. A novel dissolution rate smoothing algorithm is introduced to improve the robustness of the model and ensure the accuracy of the dissolution shape prediction.

The numerical method employed is verified by evaluating the self-consistency of the model. Both spatial and temporal convergence is demonstrated in the results.

The proposed model can capture complex flow patterns arising because of the coupled effect of nonlinear brine flow equations and physically-derived dissolution rate. The evolution of the flow velocity, mass fraction of dissolved minerals, and cavity shape are studied in numerical simulations. A mechanism captured in this work but rarely reported in previous models is the generation of a vortex near the cavity inlet that promotes mineral dissolution and traps some dissolved minerals within the cavity. The cavity widens most in the areas corresponding to strong vortex flow. A single vortex generated in a system will grow in size over time, advancing the area of higher dissolved mineral mass towards the outlet. Flow with a higher Peclet number leads to faster vortex growth and migration, and therefore more dissolution near the outlet.

The second objective of this research program is to develop a numerical model for nonlinear

mineral dissolution processes with inclusion of buoyancy effects arising from differences in brine density (i.e., salt concentration). A novel simulation model used to investigate non-linear mineral dissolution processes, including gravity effects, is developed, verified, and semi-quantitatively validated against bench-top experiments. The time-averaged brine properties are used to calculate the dissolution front movement. The new liquid/solid boundary evolution algorithm enables the model to predict the change of different brine-solid surfaces (interfaces) at any location and in different orientations. The model fully couples the dissolution pattern with the brine flow in the cavity.

Verification of the numerical aspects of the model demonstrates that both spatial and temporal convergence is achieved. Validation is conducted, and the simulation results show good agreement with both vertical and horizontal two-dimensional laboratory dissolution experiments.

The model can simulate dissolution cavity evolution under vertical and horizontal dissolution methods. Gravity is shown, both in experiments and simulations, to play a vital role in bench-top-sized systems. For the vertical scenario, the buoyancy effects promote the dissolution of the top front and contribute to the development of eddies. Perfectly symmetric caverns/configurations are hard to achieve even in homogeneous salt formations because the eddies affect the brine flow and dissolution, and the dissolution process is non-reversible. So, symmetric caverns should not be expected in practice. For the horizontal scenario, the fresh water from the inlet rises quickly to the top of the cavity. The dissolution rate between the inlet and outlet along the top of the cavern decreases significantly. The front below the inlet will not undergo significant dissolution.

This work advances the understanding of the complicated nature of mineral dissolution and the critical role of buoyancy and eddies in developing both vertical and horizontal salt caverns.

The final objective of the thesis is to develop an integrated numerical model for large-scale cavern evolution under turbulent flow. Brine flow patterns are solved using Reynolds-averaged Navier–Stokes equations. The $k - \omega - SST$ model is applied to obtain detailed turbulent brine flow information in the cavity and near the dissolution front. The physically-driven dissolution front evolution equation is coupled with the turbulent brine flow governing equations and numerically solved.

The turbulence of brine leads to irregular wall shapes, even if the surrounding mineral characteristics are stipulated to be perfectly homogeneous. Generated eddies result in uneven distribution of the dissolved mineral in the cavity, leading to variations of dissolution rate along the cavern boundary and a consequent irregular cavern shape. In turn, the cavern topology also affects the brine flow pattern and influences the dissolution front evolution.

The model can reasonably simulate cavern evolution under different shape control methods used in the industry. The "morning glory" shape arises more strongly with reverse dissolution, whereas the direct dissolution method also generates a "wide bottom decanter" shape and a small "morning glory" roof span. The brine flow pattern in the cavern has a significant impact on the cavern shape evolution. Because gravity (density buoyancy) plays an important role in brine flow and dissolution patterns, the "morning glory" shape arises in both dissolution modes. Overhanging blocks will develop in the middle of the cavity under both direct and reverse dissolution because of the brine convection. Using an oil/gas

blanket at the cavity top helps control overall cavity development, avoids excessive roof span, but contributes to irregular shape caverns with jagged boundaries when the blanket is applied to multiple locations. The blanket application can lead to a large overhang at the center of the cavity, and it also reduces the cavity construction rate. Considerations of surrounding formation heterogeneity and changes in fresh water injection velocity will increase the cavern shape complexity.

The model demonstrates that there is a competition between the mechanics of dissolution: (1) surface deviations lead to eddies which change the local dissolution rate and increase surface complexity; and (2) when irregularities become too severe, flow bypasses the deviations, and accelerates dissolution, thereby decreasing the surface complexity and smoothing the shape edges.

This work advances the understanding of the complicated nature of mineral dissolution processes. The results show the critical roles of gravity and turbulent brine flow in developing a large-scale cavity. The simulation methodology presented shows promise for providing reliable predictions for industrial scale solution cavern construction.

Simulation of cavern/cavity evolution is challenging because of the complex coupled physics involved. There is no dissolution prediction model currently available that rigorously incorporates all the mechanisms that lead to cavern shape change under dissolution mining. A numerical model that can simulate the forced and natural convection of brine, mineral dissolution and transportation, and cavern boundary evolution will be a valuable tool for better understanding the dissolution mechanism and help industries make operational decisions. Although the SCI-FIE models presented in this thesis still have limitations in their

136

application to study all the mechanisms behind the complex dissolution problem, especially in the in-suit dissolution scenario, they address the important relationships between the brine pattern and cavern boundary evolution. The SCI-FIE models open a new pathway to support the creation of advanced dissolution models by addressing the numerical challenges posed by the highly nonlinear coupled mechanisms involved in dissolution mining. Lastly, the simulation methodology presented shows great promise for applications to reactive leachate mining of other ore bodies,ice melting, karst-forming processes, and other physically similar process.

6.2 Significant contributions

Contributions that advance the knowledge of mineral dissolution and cavern shape control have been achieved during the process of accomplishing the objectives of this research. The contributions are highlighted and disseminated in peer-reviewed journals and conference papers and can be summarized below.

The paper, which highlights the first object of developing a tractable numerical simulation model involving free brine flow and physically-driven boundary evolution, is:

- L. Li, E. Rivas, R. Gracie, M. B. Dusseault, Methodology for the nonlinear coupled multiphysics simulation of mineral dissolution, International Journal for Numerical and Analytical Methods in Geomechanics 45 (15) (2021) 2193–2213.

The key contributions of the work are:

- The dissolution front evolution is determined using a loosely coupled algorithm, taking advantage of the scale difference between brine flow rate and dissolution rate.

- The incompressible Navier-Stokes equations and physically-derived dissolution rate equations were coupled and solved to give more information about the relation between brine flow and cavity shape evolution.

- The algorithm is suitable for simulating large domains and long-term dissolution processes and can capture the effect of vortices on dissolution patterns and cavity geometry evolution.

The second objective of the thesis is to develop a numerical model for non-linear mineral dissolution processes with buoyancy effects. The work is published in:

- L. Li, R. Gracie, M. B. Dusseault, N. Xiao, W. Liang, Modeling and verification of non-linear mineral dissolution processes with buoyancy effects, International Journal of Rock Mechanics and Mining Sciences, 2022 (Under Review)

The key contributions of the work are:

- The gravity (density) effect is included in the model, confirming the important role density differences play in the dissolution process.

- The model calculates the quasi-steady dissolution rate based on the time-averaged brine properties, enabling the simulation of longer dissolution processes in larger caverns.

- The model is verified, qualitatively validated, and has proven capable of simulating cavity boundary evolution in different orientations and locations on the scale of a meter.

The third object of the thesis is to develop an integrated numerical model for large-scale cavern evolution under turbulent flow condtions. The work is published in:

- L. Li, R. Gracie, M. B. Dusseault. Strategically Coupled Inertial Flow and Interface Evolution Model for Cavern Development by Dissolution, Applied Energy (Under Review)

Additional results are published in:

- L. Li, R. Gracie, M. B. Dusseault. Salt Cavern Dissolution Mining: Lessons Learned from Simulations. in: 56th U.S. Rock Mechanics/Geomechanics Symposium, U.S. Rock Mechanics/Geomechanics Symposium, American Rock Mechanics Association, 2022.

The key contributions of the works are:

- Nonlinear equations of turbulent brine flow continuity, conservation of momentum, and advection-diffusion are solved iteratively in the model. Detailed turbulent flow information in the cavity and near the dissolution fronts is obtained.

- The model shows excellent reliability for simulating cavern evolution under various shape control methods on an industrial scale and can even give an excellent prediction of cavern evolution in the case of an insoluble interlayer present in the solution mining sequence.

- The interesting competitive mechanics that arise in a large-scale dissolution process have been identified for the first time, and investigated for several relevant cases.

6.3 Directions for future study

Throughout the investigation for this thesis, many ideas for improving and extending this research have arisen but have not been covered because of time constraints. Possible directions for future work to continue to enhance mineral dissolution and cavity shape control as well as engineering predictions are summarized below:

Validation of large-scale dissolution: The validation of the dissolution process is challenging because cavity evolution is a path-dependent process. Although qualitative validation with lab-scale experiments has shown that the methods developed are potentially quite powerful, large-scale cavern evolution modeling with turbulent brine flow is not yet validated through careful field measurements. Validation of large-scale cavern evolution is recommended; this, can be done based on availability of detailed industrial monitoring data for cavern shapes during the dissolution mining process (along with other relevant data related to the dissolution process such as rate, velocity, input/outlet locations...).

Crystallization: Two opposite effects occur at the solid-liquid interface, where solid minerals are in contact with the brine. They are the dissolution of solid minerals and the re-crystallization of minerals from the brine. These actions happen together, but the dissolution and crystallization rates are different before the equilibrium state is achieved. A local re-crystallization process may happen in the cavity where the crystallization rate of minerals is higher than the dissolution rate. Indeed, this may also be impacted by temperature differences arising because of the vertical cavern height and the geothermal gradient when the large-scale cavern (over a hundred meters in height) is developed. This work has not included the temperature or the temperature gradient impact on the dissolu-

140

tion/crystallization process. Thus, in these models, the local non-equilibrium dissolution equations are used to simulate the dissolution, and the re-crystallization is ignored. Including the two opposite effects is potentially an interesting and useful direction.

Complex geological conditions: Although the cavern evolution with one horizontal insoluble interlayer has been investigated, the actual geological conditions can be far more complex. For example, there may be different salts with various solubilities (as in the case of solution mining of potash). There may be a significant number of interbeds in the vertical sequence that is being dissolved. A numerical model that can consider temperature effects, heterogeneous mineral properties, and multi-interlayers with different orientations is of interest as it enables a more rigorous study of cavern evolution prediction in practice. The main challenge for introducing these into the coupled model is the additional computational difficulties of obtaining a converged solution due to the nonlinearity of the moving boundary problem. If this challenge can be overcome, the model can be used to perform sensitivity analyses of the factors that affect in-situ dissolution to enhance the understanding of the principal factors driving the efficiency of the shape control.

Application: The numerical models proposed in this thesis can be used to simulate other scenarios of interest in the domain of the boundary evolution process. The model can simulate in-situ chemical leach mining by adding the chemical reactions into the model. The development of the karst feature in carbonates or gypsum is another topic to which the model can be applied. Predicting the development of caves or sinkholes helps the engineering assessment of the landscape. Additionally, the model can be used to simulate ice melting, which must also consider the thermodynamics of phase changes and heat transfer in the system. However, adding more physics also means making the model

141

more nonlinear, and the convergence and reliability of the model can be potential concerns.

Extension to three dimensions: The two-dimensional mineral dissolution and cavity evolution model is useful for investigating the qualitative trends of dissolution behaviour. However, the simplifications necessary for two-dimensional simulations limit the scope of the applications, as they significantly impact the accuracy of the prediction. Although an axisymmetric model is used to study large-scale dissolution simulation in the last objective, it still has differences from the actual cavern dissolution process, and only a limited (axisymmetric) amount of heterogeneity can be investigated. In reality, brine flow and vortex development is three-dimensional, the salt structures as well (particularly in domal salts), and the evolution of the cavity is affected by the three-dimensionality of the fluid flow. The three-dimensional cavity shape changes and brine flow evolution can not be captured in a two-dimensional model. An extension of the model to a three-dimension form will produce more realistic and accurate results. It will also be far more computationally intensive, so the continued pursuit of robust simplifications and more efficient solution approaches constitute important future work.

References

[1] Z. Zhao, W. Zhu, W. Shan, Y. Wan, Research on mechanism of solution mining for building underground gas storage in salt cavern, Petroleum Exploration and Development 30 (5) (2003) 107–109.

[2] D. E. Garrett, Solution Mining, Springer Netherlands, Dordrecht, 1996, pp. 304–324.

[3] X. Dai, R. Su, J. Ma, G. Zhang, L. Tang, Mining technology research on Glauber's salt horizontally connected well pairs, China Well and Rock Salt 4 (4) (2012) 9.

[4] M. Hardy, M. Ramey, C. Yates, K. Nielsen, Solution mining of nahcolite at the American Soda Project, Piceance Creek, Colorado, SME Annual Mtg., Feb (2003) 24–26.

[5] G. Sears, F. Jessen, Controlled solution mining in massive salt, Society of Petroleum Engineers Journal 6 (02) (1966) 115–125.

[6] J. Istvan, L. Evans, J. Weber, C. Devine, Rock mechanics for gas storage in bedded salt caverns, International Journal of Rock Mechanics and Mining Sciences 34 (3-4) (1997) 142–e1.

[7] A. Ozarslan, Large-scale hydrogen energy storage in salt caverns, International Journal of Hydrogen Energy 37 (19) (2012) 14265–14277.

[8] M. Langer, Principles of geomechanical safety assessment for radioactive waste disposal in salt structures, Engineering Geology 52 (3-4) (1999) 257–269.

[9] K. Allen, CAES: the underground portion, IEEE Transactions on Power Apparatus and Systems PAS-104 (4) (1985) 809–812.

[10] L. Wei, C. Jie, J. Deyi, S. Xilin, L. Yinping, J. Daemen, Y. Chunhe, Tightness and suitability evaluation of abandoned salt caverns served as hydrocarbon energies storage under adverse geological conditions (AGC), Applied Energy 178 (2016) 703–720.

[11] M. Raju, S. K. Khaitan, Modeling and simulation of compressed air storage in caverns: a case study of the Huntorf plant, Applied Energy 89 (1) (2012) 474–481.

[12] L. Li, W. Liang, H. Lian, J. Yang, M. B. Dusseault, Compressed air energy storage: characteristics, basic principles, and geological considerations, Advances in Geo-Energy Research 2 (2) (2018) 135–147.

[13] K. van Thienen-Visser, D. Hendriks, A. Marsman, M. Nepveu, R. Groenenberg, T. Wildenborg, H. van Duijne, M. den Hartogh, T. Pinkse, Bow-tie risk assessment combining causes and effects applied to gas oil storage in an abandoned salt cavern, Engineering Geology 168 (2014) 149–166.

[14] J. Li, X. Shi, C. Yang, Y. Li, T. Wang, H. Ma, H. Shi, J. Li, J. Liu, Repair of irregularly shaped salt cavern gas storage by re-leaching under gas blanket, Journal of Natural Gas Science and Engineering 45 (2017) 848–859.

[15] T. Xue, C. Yang, X. Shi, M. Hongling, Y. Li, X. Ge, X. Liu, The formation mechanism of irregular salt caverns during solution mining for natural gas storage, Energy Sources, Part A: Recovery, Utilization, and Environmental Effects 0 (0) (2020) 1–17.

[16] J. Chen, D. Lu, W. Liu, J. Fan, D. Jiang, L. Yi, Y. Kang, Stability study and optimization design of small-spacing two-well (sstw) salt caverns for natural gas storages, Journal of Energy Storage 27 (2020) 101131.

[17] J. Li, L. Wang, C. Liu, D. Zhou, Y. Wang, J. He, Y. Xue, Factors affecting cavities distortion of jintan salt caverngas storage, Oil and Gas Storage and Transportation 33 (3) (2014) 269–273.

[18] W. Liu, Z. Zhang, J. Fan, D. Jiang, J. J. Daemen, Research on the stability and treatments of natural gas storage caverns with different shapes in bedded salt rocks, IEEE Access 8 (2020) 18995–19007.

[19] J. Wan, T. Peng, M. J. Jurado, R. Shen, G. Yuan, F. Ban, The influence of the water injection method on two-well-horizontal salt cavern construction, Journal of Petroleum Science and Engineering 184 (2020) 106560.

[20] T. Wang, X. Yan, H. Yang, X. Yang, T. Jiang, S. Zhao, A new shape design method of salt cavern used as underground gas storage, Applied Energy 104 (2013) 50–61.

[21] T. Wang, H. Ma, X. Shi, C. Yang, N. Zhang, J. Li, S. Ding, J. Daemen, Salt cavern gas storage in an ultra-deep formation in Hubei, china, International Journal of Rock Mechanics and Mining Sciences 102 (2018) 57–70.

[22] K. Cyran, M. Kowalski, Shape modelling and volume optimisation of salt caverns for energy storage, Applied Sciences 11 (1) (2021) 423.

[23] T. Wang, C. Yang, H. Wang, S. Ding, J. Daemen, Debrining prediction of a salt cavern used for compressed air energy storage, Energy 147 (2018) 464–476.

145

[24] C. Yang, T. Wang, H. Ma, Y. Li, X. Shi, J. Daemen, Feasibility analysis of using horizontal caverns for underground gas storage: a case study of Yunying salt district, Journal of Natural Gas Science and Engineering 36 (2016) 252–266.

[25] D. Qi, S. Li, Y. Wang, Characteristics of cavity differential dissolution of Jintan salt cave gas reservoir, Journal of Southwest Petroleum University (Science & Technology Edition) 41 (2) (2012) 75–83.

[26] D. Jiang, L. Yi, J. Chen, S. Ren, H.-F. Qiu, Y.-P. Li, Laboratory similarity test relevant to salt cavern construction in interlayer-containing moulded saliferous aggregates specimen, Current Science (00113891) 111 (1) (2016) 157–167.

[27] Q. Wanyan, Y. Xiao, N. Tang, Numerical simulation and experimental study on dissolving characteristics of layered salt rocks, Chinese Journal of Chemical Engineering 27 (5) (2019) 1030–1036.

[28] A. Russo, Horizontal natural gas storage caverns and methods for producing same, US Patent 5,431,482 (Jul. 11 1995).

[29] D. Shock, Use of hydraulic fracturing to make a horizontal storage cavity in salt, 2nd Northern Ohio Geol. Soc. Symp. on Salt (United States), Continental Oil Co, United States, 1966, p. 406.

[30] R. Thoms, R. Gehle, A brief history of salt cavern use, The 8th World Salt Symposium. [S. l.], Elsevier, Netherlands, 2000, pp. 207–214.

[31] J. Wan, T. Peng, R. Shen, M. J. Jurado, Numerical model and program development of TWH salt cavern construction for UGS, Journal of Petroleum Science and Engineering 179 (2019) 930–940.

[32] H. Kazemi, F. Jessen, Mechanism of Flow and Controlled Dissolution of Salt in Solution Mining, Society of Petroleum Engineers Journal 4 (04) (1964) 317–328.

[33] R. C. Kerr, C. D. McConnochie, Dissolution of a vertical solid surface by turbulent compositional convection, Journal of Fluid Mechanics 765 (2015) 211–228.

[34] S. Molins, C. Soulaine, N. I. Prasianakis, A. Abbasi, P. Poncet, A. J. Ladd, V. Starchenko, S. Roman, D. Trebotich, H. A. Tchelepi, Simulation of mineral dissolution at the pore scale with evolving fluid-solid interfaces: review of approaches and benchmark problem set, Computational Geosciences (2020) 1–34.

[35] A. Zidane, E. Zechner, P. Huggenberger, A. Younes, Simulation of rock salt dissolution and its impact on land subsidence, Hydrology and earth system sciences 18 (6) (2014) 2177–2189.

[36] S. Gärttner, P. Frolkovič, P. Knabner, N. Ray, Efficiency and Accuracy of Micro-Macro Models for Mineral Dissolution, Water Resources Research 56 (8) (2020) e2020WR027585.

[37] J. Nolen, O. von Hantlemann, S. Meister, W. Kleinitz, J. Heiblinger, Numerical simulation of the solution mining process, SPE European Spring Meeting, Society of Petroleum Engineers, Netherlands, 1974.

[38] C. I. Steefel, A. C. Lasaga, Evolution of dissolution patterns: Permeability change due to coupled flow and reaction, in: Chemical Modeling of Aqueous Systems II, ACS Publications, 1990, Ch. 16, pp. 212–225.

[39] J. Chen, C. Liu, Numerical simulation of the evolution of aquifer porosity and species concentrations during reactive transport, Computers & Geosciences 28 (4) (2002) 485–499.

[40] Q. Kang, D. Zhang, S. Chen, Simulation of dissolution and precipitation in porous media, Journal of Geophysical Research: Solid Earth 108 (B10) (2003) 1–10.

[41] H. Luo, M. Quintard, G. Debenest, F. Laouafa, Properties of a diffuse interface model based on a porous medium theory for solid–liquid dissolution problems, Computational Geosciences 16 (4) (2012) 913–932.

[42] J. Guo, F. Laouafa, M. Quintard, A theoretical and numerical framework for modeling gypsum cavity dissolution, International Journal for Numerical and Analytical Methods in Geomechanics 40 (12) (2016) 1662–1689.

[43] H. Luo, F. Laouafa, J. Guo, M. Quintard, Numerical modeling of three-phase dissolution of underground cavities using a diffuse interface model, International Journal for Numerical and Analytical Methods in Geomechanics 38 (15) (2014) 1600–1616.

[44] H. Luo, F. Laouafa, G. Debenest, M. Quintard, Large scale cavity dissolution: From the physical problem to its numerical solution, European Journal of Mechanics-B/Fluids 52 (2015) 131–146.

[45] F. Laouafa, J. Guo, M. Quintard, Modeling of salt and gypsum dissolution: applications, evaluation of geomechanical hazards, European Journal of Environmental and Civil Engineering (2019) 1–22.

[46] M. B. Cardenas, D. T. Slottke, R. A. Ketcham, J. M. Sharp Jr, Effects of inertia and directionality on flow and transport in a rough asymmetric fracture, Journal of Geophysical Research: Solid Earth 114 (B6) (2009).

[47] J. Yang, H. Li, C. Yang, Y. Li, T. Wang, X. Shi, Y. Han, Physical simulation of flow field and construction process of horizontal salt cavern for natural gas storage, Journal of Natural Gas Science and Engineering 82 (2020) 103527.

[48] R. Durie, F. Jessen, The influence of surface features in the salt dissolution process, Society of Petroleum Engineers Journal 4 (03) (1964) 275–281.

[49] J. Li, Y. Tang, X. Shi, W. Xu, C. Yang, Modeling the construction of energy storage salt caverns in bedded salt, Applied Energy 255 (2019) 113866.

[50] J. Li, W. Xu, J. Zheng, W. Liu, X. Shi, C. Yang, Modeling the mining of energy storage salt caverns using a structural dynamic mesh, Energy 193 (2020) 116730.

[51] J. Li, X. Shi, S. Zhang, Construction modeling and parameter optimization of multi-step horizontal energy storage salt caverns, Energy 203 (2020) 117840.

[52] B. Sedaee, M. Mohammadi, L. Esfahanizadeh, Y. Fathi, Comprehensive modeling and developing a software for salt cavern underground gas storage, Journal of Energy Storage 25 (2019) 100876.

[53] X. Liu, X. Yang, Z. Zhong, N. Liang, J. Wang, M. Huang, Research on dynamic dissolving model and experiment for rock salt under different flow conditions, Advances in Materials Science and Engineering 2015 (2015).

[54] X. Yang, X. Liu, Numerical simulation of rock salt dissolution in dynamic water, Environmental Earth Sciences 76 (12) (2017) 1–10.

[55] D. Reda, A. Russo, Experimental studies of salt cavity leaching via fresh-water injection, Tech. rep., Sandia National Labs., Albuquerque, NM (USA) (1984).

[56] T. Stocker, Introduction to climate modelling, Springer Science & Business Media, Switzerland, 2011.

[57] J. Wan, T. Peng, G. Yuan, F. Ban, M. J. Jurado, Y. Xia, Influence of tubing/oil-blanket lifting on construction and geometries of two-well-horizontal salt caverns, Tunnelling and Underground Space Technology (2020) 103688.

[58] L. H. Engvall, T. J. O'Hern, D. L. Lord, Experimental characterization of temperature dependence of salt dissolution rate, Tech. Rep. No. SAND2013-2398C, Sandia National Lab.(SNL-NM), Albuquerque, NM (United States) (2013).

[59] S. A. Socolofsky, G. H. Jirka, Special topics in mixing and transport processes in the environment, Engineering–Lectures. 5th Edition. Texas A&M University (2005) 1–93.

[60] R. W. Durie, F. Jessen, Mechanism of the dissolution of salt in the formation of underground salt cavities, Society of Petroleum Engineers Journal 4 (02) (1964) 183–190.

[61] D. C. Reda, A. J. Russo, Experimental studies of salt-cavity leaching by freshwater injection, SPE Production Engineering 1 (01) (2013) 82–86.

[62] F. Bayram, I. Bektasoglu, Determination of actual dissolution rates from some rock properties in construction of deep salt cavern for natural gas storage, International Journal of Rock Mechanics and Mining Sciences 126 (2020) 104183.

[63] S. Kim, J. Santamarina, Geometry-coupled reactive fluid transport at the fracture scale: application to co_2 geologic storage, Geofluids 16 (2) (2016) 329–341.

[64] L. Li, R. Gracie, M. B. Dusseault, Numerical simulation of salt rock dissolution, in: 54th U.S. Rock Mechanics/Geomechanics Symposium, U.S. Rock Mechanics/Geomechanics Symposium, American Rock Mechanics Association, Physical event cancelled, 2020.

[65] J. Yang, H. Li, C. Yang, Y. Li, T. Wang, X. Shi, Y. Han, Physical simulation of flow field and construction process of horizontal salt cavern for natural gas storage, Journal of Natural Gas Science and Engineering 82 (2020) 103527.

[66] F. Gibou, R. Fedkiw, S. Osher, A review of level-set methods and some recent applications, Journal of Computational Physics 353 (2018) 82–109.

[67] J. Kim, Phase-field models for multi-component fluid flows, Communications in Computational Physics 12 (3) (2012) 613–661.

[68] F. Bayram, I. Bektasoglu, Determination of actual dissolution rates from some rock properties in construction of deep salt cavern for natural gas storage, International Journal of Rock Mechanics and Mining Sciences 126 (2020) 104183.

[69] D. C. Reda, A. J. Russo, Experimental studies of salt-cavity leaching by freshwater injection, SPE Production Engineering 1 (01) (1986) 82–86.

[70] P. C. Lichtner, The quasi-stationary state approximation to coupled mass transport and fluid-rock interaction in a porous medium, Geochimica et Cosmochimica Acta 52 (1) (1988) 143–165.

[71] X. Li, H. Huang, P. Meakin, Level set simulation of coupled advection-diffusion and pore structure evolution due to mineral precipitation in porous media, Water Resources Research 44 (12) (2008) W12407.

[72] C. Oltéan, F. Golfier, M. A. Buès, Numerical and experimental investigation of buoyancy-driven dissolution in vertical fracture, Journal of Geophysical Research: Solid Earth 118 (5) (2013) 2038–2048.

[73] N. Weisbrod, C. Alon-Mordish, E. Konen, Y. Yechieli, Dynamic dissolution of halite rock during flow of diluted saline solutions, Geophysical Research Letters 39 (9) (2012) L09404.

[74] X. Chen, Y. Li, X. Ge, X. Shi, T. Xue, Simulating the transport of brine in the strata of bedded salt cavern storage with a fluid–solid coupling model, Engineering Geology 271 (2020) 105595.

[75] D. C. Wilcox, et al., Turbulence modeling for CFD, Vol. 2, DCW industries La Canada, CA, 1998.

[76] S. Heinz, A review of hybrid rans-les methods for turbulent flows: Concepts and applications, Progress in Aerospace Sciences 114 (2020) 100597.

[77] F. R. Menter, Review of the shear-stress transport turbulence model experience from an industrial perspective, International journal of computational fluid dynamics 23 (4) (2009) 305–316.

[78] H.-G. Sung, S.-J. Kim, H.-W. Yeom, J.-Y. Heo, On the assessment of compressibility effects of two-equation turbulence models for supersonic transition flow with flow separation, International Journal of Aeronautical and Space Sciences 14 (4) (2013) 387–397.

[79] F. R. Menter, Two-equation eddy-viscosity turbulence models for engineering applications, AIAA journal 32 (8) (1994) 1598–1605.

[80] C. Fu, C. Bounds, M. Uddin, C. Selent, Fine tuning the sst k- ω turbulence model closure coefficients for improved nascar cup racecar aerodynamic predictions, SAE International Journal of Advances and Current Practices in Mobility 1 (2019-01-0641) (2019) 1226–1232.

[81] F. R. Menter, M. Kuntz, R. Langtry, Ten years of industrial experience with the sst turbulence model, Turbulence, heat and mass transfer 4 (1) (2003) 625–632.

[82] X. Chen, Y. Li, X. Ge, X. Shi, T. Xue, Simulating the transport of brine in the strata of bedded salt cavern storage with a fluid–solid coupling model, Engineering Geology 271 (2020) 105595.

[83] W. Liu, Z. Zhang, J. Chen, J. Fan, D. Jiang, D. Jjk, Y. Li, Physical simulation of construction and control of two butted-well horizontal cavern energy storage using large molded rock salt specimens, Energy 185 (2019) 682–694.

[84] D. Jiang, H. Qiu, L. Yi, S. Ren, J. Chen, C. Yang, Similar experimental study of cavity building using large-size molded salt rock, Chinese Journal of Rock Mechanics and Engineering 31 (9) (2012) 1746–1755.

Appendices

Appendix A

Additional case studies of large-scale turbulence-driven cavern development simulation

In this section, two more cases studies are investigated to demonstrate the ability of the SCI-FIE models. The first case studies brine flow and cavity evolution under different fresh water injection velocities. The second one focuses on the influence of an insoluble interface on the cavern shape evolution. The initial cavity geometry is same as demonstrated in Chapter 5. In the first case study, the surrounding mineral formation is assumed to be pure and homogeneous. In the second case study, an insoluble interlayer is included in the model, and the specification of the dissolution front boundary condition is discussed in Section A.2. Reverse dissolution are studies in this section. The fresh water is injected through the outer tube, which has a radius of 0.2 m and reaches 5 m depth. The brine with the dissolved mineral is discharged through the inner tube, whose radius is 0.1 m and

is 10 m deep.

A.1 Cavity evolution under different injection velocities

The influence of the fresh water injection velocity on the cavern development in a pure and homogeneous dissoluble mineral formation is investigated in this section. To investigate the injection velocity effect, the fresh water injection velocity is set to be 0.5 m/s and 1.0 m/s. The injection velocity is constant during dissolution simulation, whereas in actual cavern construction, a changing injection velocity is commonly used to help achieve regularly shaped caverns. The Reynolds number can reach 2.5×10^5 and 5×10^5, which means the turbulent brine flow will appear in the cavity. Reverse dissolution is studied in this Section.

The cavity shape evolution under the two injection velocities is shown in Figure A.1. The caverns expand because of the continuous injection of fresh water. A "morning glory" shape cavern develops under the two injection velocities, and the large top keeps expanding with time. For both scenarios, the bottom of the caverns does not undergo apparent expansion, indicating that there is not much dissolution in the area. When the injection velocity is 0.5 m/s, some small oscillations appear in the dissolution front, causing the generation of the small overhanging parts, even though the soluble mineral around the cavity is assumed to be pure and homogeneous. This indicates that heterogeneity of the salt formation is not the only reason leading to overhang generation. When the injecting velocity increases to 1 m/s, the development of the large overhanging becomes substantial. As shown in Figure A.1, there is a large overhang generated at a depth of 6 m when the injection velocity is
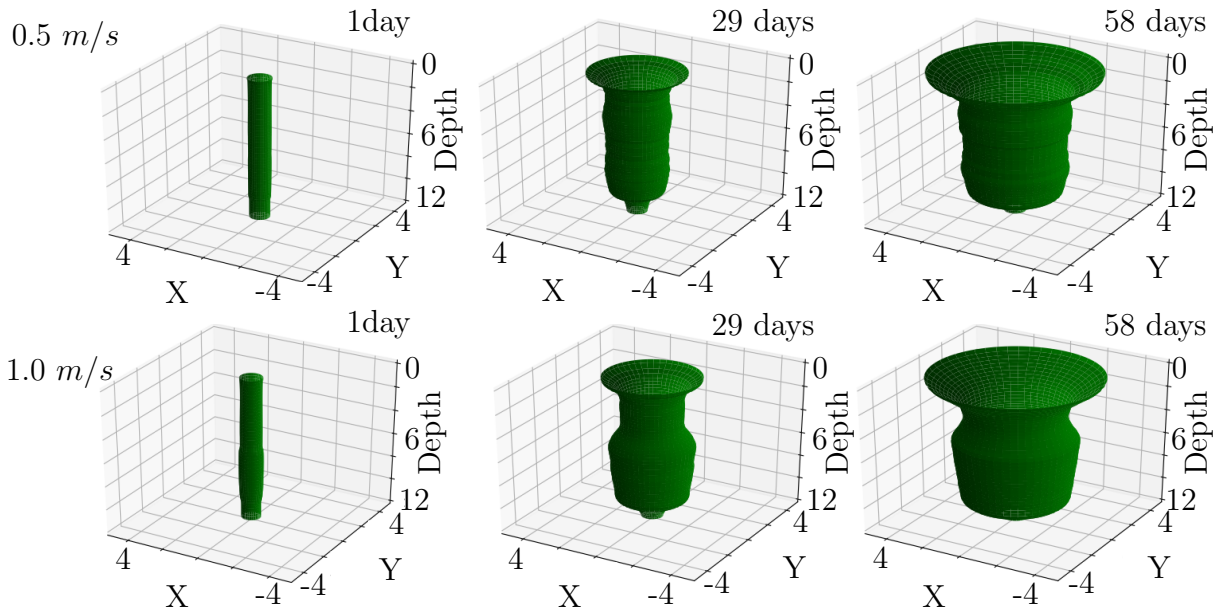
Figure A.1: 3D cavity evolution under different injecting velocity.

large.

To investigate how the brine flow has an impact on the dissolution pattern, a "snapshot" of the averaged brine flow pattern in the initial cavity under different fresh water injection velocities is taken and shown in Figure A.2. It is noticed that the cavity shape evolution under different injection velocities is different, so the snapshots of brine flow in the initial cavities are taken to conduct a comparison. The overall distribution of the dissolved mineral is similar under the two injection velocities. The less-dense brine occupies the majority of the cavity. Below the outlet location, there is a clear interface between the less concentrated brine and saturated brine; fresh water injection does not disturb the distribution. This shows that the buoyancy effect is crucial; it promotes lighter brine transport to the top of the cavern, and the denser brine settles down below the outlet. This results in a significant dissolution rate in the upper part of the cavity boundary and only a slight
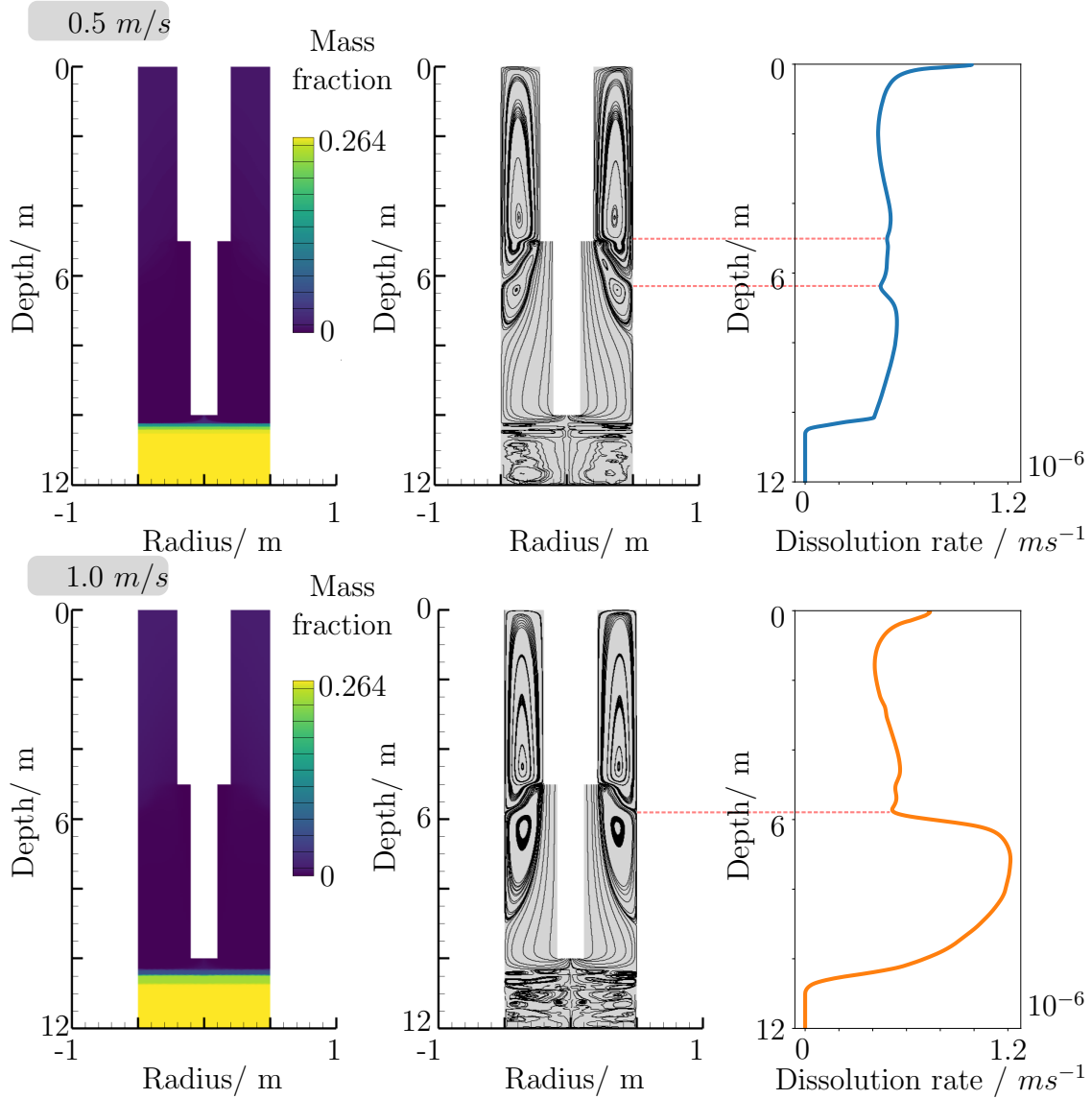
Figure A.2: Mass fraction, brine flow pattern, and dissolution rate distribution in the initial cavity under different injection velocity.

dissolution below the outlet.

The increase of the injection velocity results in a difference of the brine flow pattern above the outlet location. As shown in the middle pictures in Figure A.2, the injection of fresh water leads to vortex generation in the cavity. The size of the vortices grows with an increase of the inlet fresh water velocity. When the injection velocity is 0.5 m/s, a large vortex develops between 0- 6 m due to the combined effect of the convection and buoyancy. The fresh water was taken to the top of the cavity, resulting in a significant dissolution rate, leading to the "morning glory" shape of the cavern, which evidences a large roof span. Another small eddy develops between 6-7m depth. The two counter-rotating vortexes accumulate the dissolved mineral concentration at the tip, decreasing the dissolution rate (as marked with red dash lines). This explains why the small overhangs are generated, as shown in Figure A.1.

When the injection velocity increased to 1.0 m/s, the convection of the brine in the cavity became more important. The buoyancy still has a significant impact on the upwards brine flow, so the dissolution rate of the top boundary is large. But the strong convection results in some additional fresh water flow, being involved in the dissolution between 6- 11 m. The top dissolution rate in this scenario is not as high as in the 0.5 m/s case due to lack of fresh water supply. The strong convection near the inlet results in rapid brine flow near the dissolution front and leads to a larger dissolution rate. The large overhang is then generated because of the uneven dissolution rate distribution caused by the vortices. The effect of the counter-rotating vortices on the dissolution rate is also shown in this scenario.

The results indicate that buoyancy has a significant influence on the dissolution pattern.

In addition, the turbulence of the brine in the cavity can result in variable displacement of the cavity boundary over time. The generation of the vortex is another reason for the generation of overhangs.
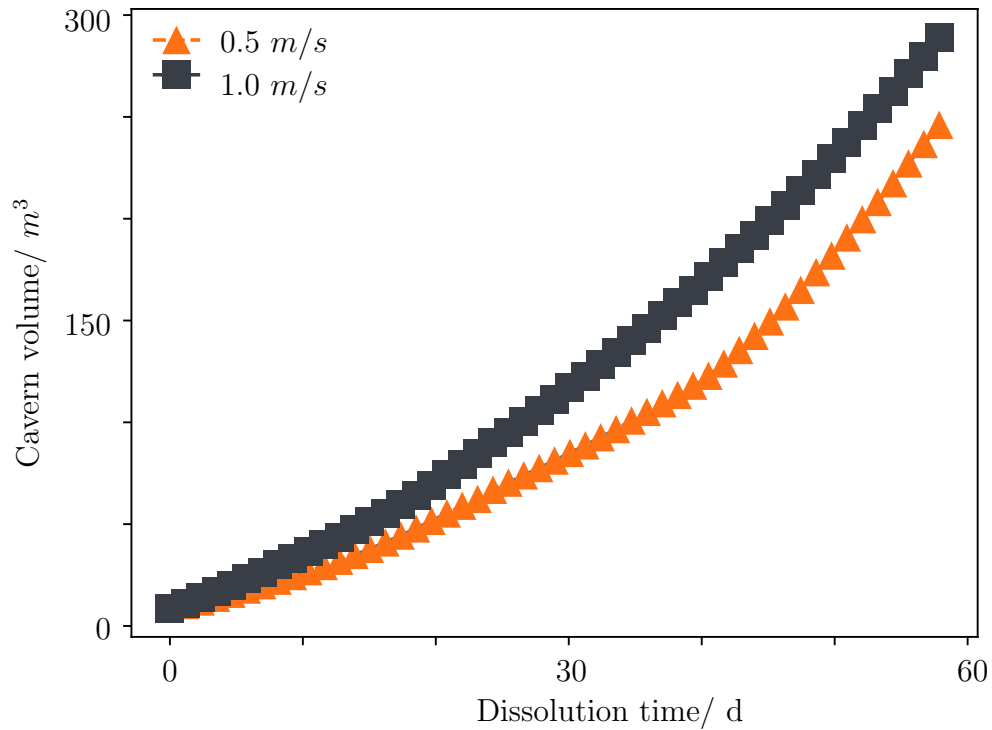

Figure A.3: Cavern volume change under different inlet velocity.

Construction efficiency is important for the development of the cavern. The cavity volume changes with time under the two different velocities are shown in Figure A.3. The cavern volume increases with time because of the continuous injection of fresh water, but the relation between the volume and construction time is not linear. Once increasing the inlet velocity, the growth rate of the cavern volume can be increased. But after the same cavern construction time, the cavity volume is not doubled when the injection velocity increases from 0.5 to 1.0 m/s. This shows that increase in inlet velocity can accelerate dissolution

of cavern, but the acceleration magnitude is inherently limited. In addition, the high inlet velocity can result in the substantially uneven dissolution of the cavern, which may be harmful to the stability of the cavity.

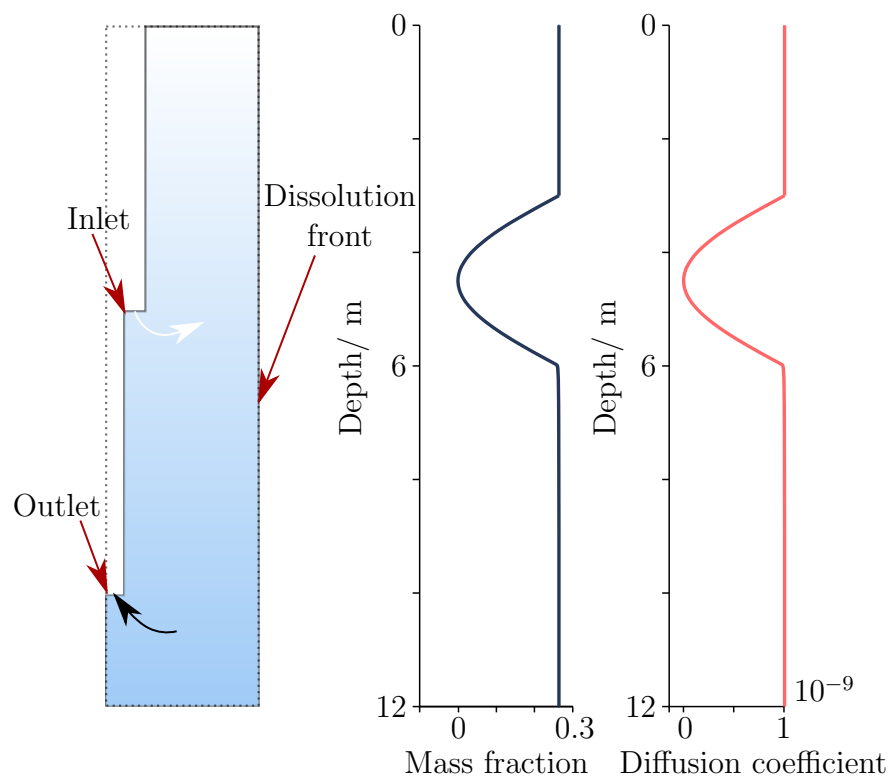## A.2   Cavity evolution with an insoluble interlayer

Figure A.4: Geometry and boundary condition of the dissolution front of the model with insoluble interlayer.

The influence of an insoluble interlayer on dissolution is investigated in this section. Special treatment of the boundary condition and dissolution rate calculation is applied to include an insoluble interlayer in the model. As shown in Figure A.4, the mass fraction of the

dissolved mineral on the dissolution front and the diffusion coefficient near the dissolution front are modified. The insoluble interlayer is assumed to be located between 3 to 6 m, the center of the interlayer is at a depth of 4.5 m. A sinusoidal profile is used to express the change of the dissolved mineral mass fraction and diffusion coefficient near the dissolution front change in the interlayer area. During the dissolution simulation, if the mass fraction in the brine near the dissolution front is greater than the value of the mass fraction on the front, then dissolution does not happen at this location. The inlet fresh water velocity is set to be 0.5 m/s in this case study.
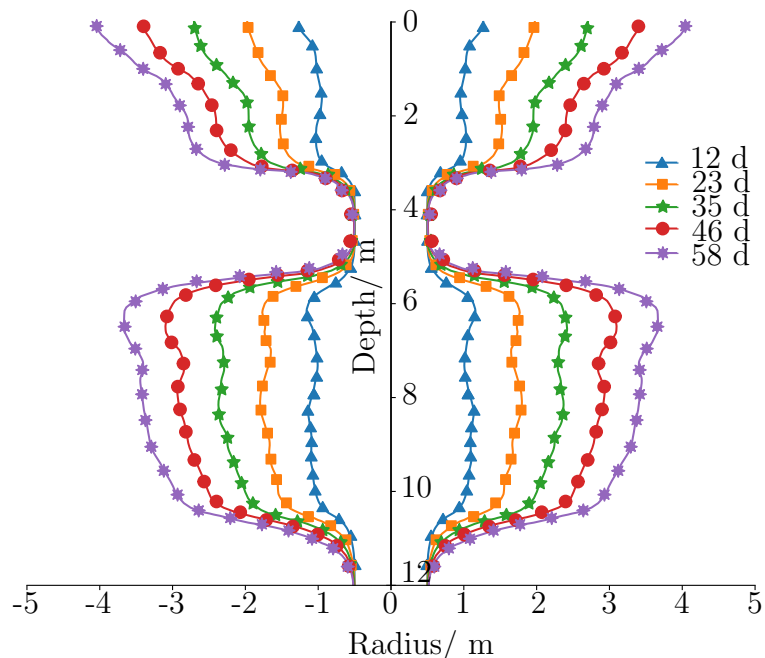

Figure A.5: The boundary evolution of the cavern constructed in the mineral formation with insoluble interlayer.

The evolution of the cavity boundary is illustrated in Figure A.5. This shows that the insoluble interlayer significantly affects the dissolution front displacement. Unlike the previous discussion of the case without the insoluble interlayer, the displacement of the dissolution boundary of the cavity does not show a continuous decreasing trend with depth. The

162

interlayer has divided the cavern into two parts. Above the interlayer, a large roof span is generated, the dissolution displacement is lower with the increase in depth, which is similar to the "morning glory" phenomenon commonly observed. The dissolution displacement experiences a sharp increase when the depth is greater than the interlayer location. At the 6 m depth location, the dissolution displacement reached approximately 4 m, which is close to the morning glory roof span. Then the dissolution displacement decreases with depth, but some small overhangs also develop. The dissolution is not significant on the boundary below the outlet. Similar dissolution cavern shapes are reported in the lab-scale experiment which studied the influence of the insoluble interlayer on the cavity shape evolution [26].
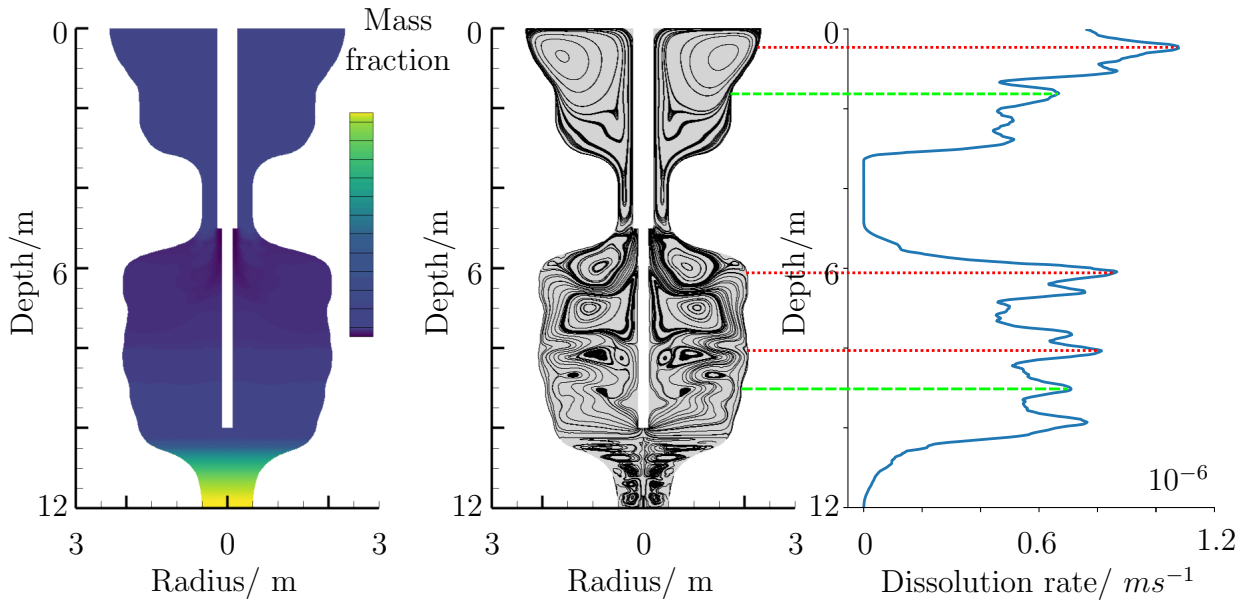

Figure A.6: Mass fraction, brine flow pattern, and dissolution rate distribution after 29 d dissolution in the cavity with insoluble interpayer.

The snapshot of the dissolved mass fraction, brine flow pattern, and dissolution rate distribution in the cavern after 29 d dissolution (shown in Figure A.6) explains why the dissolution shape evolution changes (see above). The mass fraction distribution shows

that gravity plays an important role even when the indissoluble interlayer exists. The upper part of the cavern is filled with light brine, and the denser brine settles down below the outlet. But, the distribution of the mass fraction distribution is slightly different from the case in which there are no interlayers. The mass fraction of the dissolved mineral right below the interlayer is slightly less than the value at the cavern top. The interlayer blocks the pathway of the majority of the fresh water going upward and results in sightly denser brine near the cavity top. The convection below the interlayer is strong and contributes to the complex flow pattern in the cavern. Several large vortices are generated and promote the dissolution below the interlayer. The counter-rotating eddies effect on the dissolution rate is also noticed in this case (as marked with red dash lines). In addition, it shows that the topology of the cavity also influences the dissolution. As marked with green dash lines in the figure, the location with small irregular shapes changes the brine flow direction near the dissolution front. This leads to the accumulation of dissolved mineral and decreases the dissolution rate. This bidirectional coupling of dissolution and cavity shape change has apparently not been addressed before.